AFRL-IF-RS-TR-2002-177
Final Technical Report
August 2002

ELECTROKINETIC MICROACTUATOR ARRAYS FOR CONTROL OF VEHICLES

University of Michigan

APPROVED FOR PUBLIC RELEASE; DISTRIBUTION UNLIMITED.

AIR FORCE RESEARCH LABORATORY
INFORMATION DIRECTORATE
ROME RESEARCH SITE
ROME, NEW YORK

This report has been reviewed by the Air Force Research Laboratory, Information Directorate, Public Affairs Office (IFOIPA) and is releasable to the National Technical Information Service (NTIS). At NTIS it will be releasable to the general public, including foreign nations.

AFRL-IF-RS-TR-2002-177 has been reviewed and is approved for publication

APPROVED: _Clare D. Thiem_
              CLARE D. THIEM
              Project Engineer

FOR THE DIRECTOR: _Michael Talbert_
                      MICHAEL L. TALBERT, Technical Advisor
                      Information Technology Division
                      Information Directorate

REPORT DOCUMENTATION PAGE

Form Approved
OMB No. 074-0188

1. AGENCY USE ONLY (Leave blank)	2. REPORT DATE AUGUST 2002	3. REPORT TYPE AND DATES COVERED May 98 – Oct 01

4. TITLE AND SUBTITLE
ELECTROKINETIC MICROACTUATOR ARRAYS FOR CONTROL OF VEHICLES

6. AUTHOR(S)
Francisco J. Diez-Garcia and Werner J. A. Dahm

5. FUNDING NUMBERS
C   - F30602-98-2-0228
PE - 63739E
PR - E117
TA - 00
WU - 42

7. PERFORMING ORGANIZATION NAME(S) AND ADDRESS(ES)
The University of Michigan
Department of Aerospace Engineering
Ann Arbor Michigan 48109-2140

8. PERFORMING ORGANIZATION REPORT NUMBER

037068-6

9. SPONSORING / MONITORING AGENCY NAME(S) AND ADDRESS(ES)
Defense Advanced Research Projects Agency   AFRL/IFTC
3701 North Fairfax Drive   26 Electronic Parkway
Arlington Virginia 22203-1714   Rome New York 13441-4514

10. SPONSORING / MONITORING AGENCY REPORT NUMBER

AFRL-IF-RS-TR-2002-177

11. SUPPLEMENTARY NOTES

AFRL Project Engineer: Clare D. Thiem/IFTC/(315) 330-4893/ Clare.Thiem@rl.af.mil

12a. DISTRIBUTION / AVAILABILITY STATEMENT
APPROVED FOR PUBLIC RELEASE; DISTRIBUTION UNLIMITED.

12b. DISTRIBUTION CODE

13. ABSTRACT *(Maximum 200 Words)*

Merging sense, actuation and control capability at the microscale is a challenging problem. This particular effort pursued the development of microactuator arrays that function on the electrokinetic principle to permit active contol of streamwise sublayer vortical structures in turbulent boundary layers. Electrokinetic microactuator arrays induce volume displacements in the sublayer by electrokinetic pumping under an impulsively applied electric field. The resulting micro electrokinetic actuator (MEKA) arrays have characteristics that make them potentially suited for practical sublayer control on full-scale aeronautical and hydronautical vehicles. Essentially loss-less frequency response has been demonstrated up to 10 kHz; theoretical bandwidth is in the MHz range. The final MEKA-5 is a full-scale hydronautical array with 25,600 individual electrokinetic microactuators on 350 micrometer spacing in a 7 X 7 centimeter mylar tile with a novel unit-cell architecture. The array has a MEMS-fabricated top layer with leadouts to unit-cell processing. In addition to the electrokinetic microactuators themselves, the MEKA-5 design is based on an array architecture that provides dramatic reductions in both sensor and processing requirements needed to achieve practical sublayer control on real vehicles.

14. SUBJECT TERMS
Microactuator, Arrays, Microelectromechanical Systems, MEMS, Electrokinetic, Turbulent Boundary Layer, Active Sublayer Control, Shear Stress Sensor

15. NUMBER OF PAGES
198

16. PRICE CODE

17. SECURITY CLASSIFICATION OF REPORT	18. SECURITY CLASSIFICATION OF THIS PAGE	19. SECURITY CLASSIFICATION OF ABSTRACT	20. LIMITATION OF ABSTRACT
UNCLASSIFIED	UNCLASSIFIED	UNCLASSIFIED	UL

TABLE OF CONTENTS

LIST OF FIGURES

Chapter 4

Chapter 5

Appendix A

LIST OF TABLES

LIST OF APPENDICES

Acknowledgements

ABSTRACT

Results are summarized from the development of microactuator arrays that function on the electrokinetic principle to permit active control of streamwise sublayer vortical structures in turbulent boundary layers. Electrokinetic microactuator arrays induce volume displacements in the sublayer by electrokinetic pumping under an impulsively applied electric field. Individual microchannels are formed in a substrate and filled with a 1 μm scale doped porous polymer matrix material that provides the required ζ-potential when wetted by the corresponding electrolyte. The resulting micro electrokinetic actuator (MEKA) arrays have characteristics that make them potentially suited for practical sublayer control on full-scale aeronautical and hydronautical vehicles. Several such arrays have been fabricated from a basic three-layer design. Essentially loss-less frequency response has been demonstrated up to 10 kHz; theoretical bandwidth is in the MHz range. The final MEKA-5 is a full-scale hydronautical array with 25,600 individual electrokinetic microactuators on 350 μm spacing in a 7×7 cm mylar tile with a novel unit-cell architecture. The array has a MEMS-fabricated top layer with leadouts to unit-cell processing. In addition to the electrokinetic microactuators themselves, the MEKA-5 design is based on an array architecture that provides dramatic reductions in both the sensor and processing requirements needed to achieve practical sublayer control on real vehicles.

CHAPTER 1

INTRODUCTION

1.1 Practical Applications

Active control for drag reduction on aeronautical and hydronautical vehicles is among the highest-impact applications of microsystems technology for military and commercial purposes, and represents one of the longest-standing objectives in the field of fluid dynamics. A reduction in the drag on an air vehicle of just a few percent translates into enormous system-wide reductions in fuel weight and operations costs, and corresponding increases in vehicle range and payload delivery. Similarly, flow control devices capable of on-demand vortex generation over delta wings, strakes, and other control surfaces in fighter aircraft would permit dramatic increases in maneuverability, and large reductions in radar cross-section through elimination of traditional control surfaces. Such benefits of micro-systems-based flow control extend to naval surface and undersea vehicles as well, including ships, submarines, and torpedoes, as well as to unmanned vehicles used in a variety of applications such as UAV's, UCAV's, and MAV's. Similar technologies could be also applied to supersonic vehicles for aerodynamic noise reduction, and would find use in a wide range of flow control situations involved in propulsion systems, spanning from control of mixing in advanced gas turbine combustors, to active control of surge and stall in compressors.

The prospects of actually achieving such revolutionary advances in flow control are far more realistic than they might at first seem. It is precisely in the realm of vehicle control that the underlying physics of the problem at hand and the inherent characteristics of a microsystems-based approach are ideally matched. The thin boundary layer that exists

directly adjacent to the surface of any practical vehicle is one of the most powerful nonlinear systems found in nature, capable of amplifying the effect of small microactuator-induced perturbations into very large changes in the aerodynamic forces and moments acting on the vehicle. Moreover, the inherent problem of matching the length and time scales between microactuators and the physical system being controlled makes the viscous sublayer of a turbulent boundary layer a natural choice for microsystems-based control. The exceedingly small length scales associated with flow structures that are naturally present in the viscous sublayer of turbulent boundary layers are ideally matched to microscale actuators. However the high performance required for sublayer control places rather stringent limits on the types of actuators that may be suitable for this task.

1.2   Active Sublayer Control

One approach for controlling the vehicle boundary layer is to exploit the structure and dynamics of the streamwise vortices that exist naturally in the viscous sublayer. As will be seen in §2, these sublayer vortices are typically located at distances as small as 10 μm above the vehicle surface, are spaced about 100 μm apart, are roughly 1mm long, and advect past any fixed point on the surface at frequencies up to 10-100 kHz.

Early flow visualization studies performed in the 1960s, and especially those by Kline *et al* (1967), first showed the presence of these streamwise streak structures in the near-wall region inside the turbulent boundary layer, and revealed their role in the production of turbulence within the boundary layer. Those studies originally focused on alternating arrays of low- and high-speed streak-like structures at the upper edge of the viscous sublayer. Experiments by Corino & Brodkey (1969) suggested that the presence of an inrush of high speed fluid towards the wall, termed "sweeping", was involved in the production of turbulence. Subsequent work indicated that most of the turbulence production occurs within the first 100 viscous length scales above the wall due to the dynamics of these streak-like structures (*e.g.,* Kim *et al* 1971). These early discoveries also revealed the potential implications of the streak-like near-wall structures, suggesting that control of turbulence pro-

duction in boundary layers could be achieved by proper manipulation of these coherent structures.

Subsequent experiments (*e.g.,* Blackwelder & Eckelmann 1979) found that alternating pairs of counter-rotating streamwise vortical structures at the upper edge of the viscous sublayer were the probable source of the elongated low- and high-speed streamwise streaks in the near-wall region. These structures were found to be responsible for low-speed fluid being "ejected" from the immediate vicinity of the wall, resulting in the "bursting" process by which relatively large amounts of such low-speed fluid are suddenly ejected from the near-wall region. The term "bursting" was first coined by Kline *et al* (1967) to describe the overall process by which the near-wall streaks break up. Since then, additional details about the origin and dynamics involved in the bursting process and its role in momentum transport within the boundary layer have been revealed by numerous studies. While the key role of the counter-rotating streamwise vortical structures in the bursting process has been firmly established, the precise dynamics involved remain controversial even today, and much research still continues to consider the precise physics of bursting. Further observations of the streamwise sublayer vortices in the near-wall region of turbulent boundary layers and their influence on turbulent transport can be found in Cantwell (1981) and Robinson (1991).

A number of methods have been examined to achieve skin friction reduction by either directly or indirectly controlling the streamwise sublayer structures to interrupt or otherwise alter the bursting process in wall-bounded turbulent flows. These have included both active as well as passive means. Among the earliest passive methods, preceeding the discovery of the sublayer vortical structures themselves, was the use of exceedingly long-chain polymer molecules seeded in very low concentrations (on the order of a few parts per million) in the fluid. The interaction of these long molecules with the sublayer structures has been shown reduce the skin friction as much as 80 percent (*e.g.,* Lumley & Kubo 1985; Hoyt 1990). This phenomenon, first observed by Toms (1949), is used commercially in long oil pumping systems such as the Trans Alaska Pipeline to reduce the wall shear stress and thereby lower the required pumping power. These polymers, however,

can only be used in liquid flows, and their effect is largely degraded after the fluid has been subjected to very high shear rates, as occurs in pumps. More recent work (*e.g.,* Chara *et al* 1993; Miska *et al* 1995; Warholic *et al* 1999; Zakin 2001) has used very low concentrations of surfactant ions which self-assemble into long-chain micelle structures, and in so doing produce a similar effect as long-chain polymer molecules. Unlike polymers, however, after passing through regions of high shear rates these micelles rapidly reassemble to recover their original effectiveness. A related method uses microbubbles, introduced in the near-wall region of turbulent boundary layers, to achieve wall shear stress reduction. While the precise mechanism by which the drag reduction occurs is not yet well understood, experiments have shown that wall shear stress reductions of 80% or more are achievable under laboratory conditions. As in many drag reduction methods, however, a key concern is that the pumping power required to produce such microbubbles on the subsurface hull of practical hydronautical vehicles can more than offset any power benefits from the drag reduction.

Another class of passive drag reduction methods has used fine-scale "riblets" – continuous grooves aligned in the mean streamwise direction – on the surface to alter the structure and dynamics of the near-wall region and thereby achieve wall shear stress reductions. Such riblets are typically located in the viscous sublayer of the boundary layer and have scales of the order of the structures found in that region. Walsh & Weinstein (1979) were among the first to examine this technique, and it has been examined in numerous other studies (*e.g.,* Walsh 1983; Johansen & Smith 1986; Lazos & Wilkinson 1988; Choi 1989, 1993; Pollard 1997). Drag reductions on the order of 8% have been demonstrated in laboratory experiments and in direct numerical simulations, however the precise mechanism by which the wall shear stress reduction occurs remains a subject of some controversy.

A number of other passive control methods have also been used to demonstrate manipulation of vortical structures in the near-wall region of boundary layers. Noteworthy among these, for the present study, are experiments by Gad-el-Hak & Blackwelder (1987, 1989), which showed that slot suction could prevent the bursting process of artificially generated structures in a laminar flow. In principle, this approach could be used in turbulent bound-

ary layers to reduce turbulence production by the bursting of naturally-occurring stream-wise vortical structures.

All of these passive drag reduction methods attempt to reduce the skin friction in turbulent boundary layers by modifying the coherent structures present in the viscous sublayer without actively sensing the pattern of these structures or actively reacting to changes in these coherent structures. A number of other studies have attempted to couple sensors and actuators to provide active control of wall-bounded turbulent flows. Among the earliest of these were Alshamani *et al* (1982), Wilkinson & Balasubramanian (1985), Nosenchuck & Lynch (1985), Nosenchuck *et al* (1987), Breuer *et al* (1989), and Nosenchuck & Brown (1993). Wilkinson (1990) has reviewed a number of these early attempts at active control of the near-wall structures.

The extensive development of micro-electro-mechanical-systems (MEMS) technologies over the past decade has opened a new avenue for such active control approaches for the near-wall region of turbulent boundary layers to achieve drag reduction. MEMS fabrication processes allow comparatively inexpensive production of large, dense arrays of microscale wall shear stress sensors and pressure sensors, typically having length scales of the order of a few hundred μm. Such sensor arrays are, in principle, capable of detecting the wall signature of the instantaneous coherent structure pattern in the near-wall region of turbulent boundary layers. Information of this type could, in principle, be used with large dense arrays of MEMS-fabricated wall actuators and an appropriate control system to manipulate the near-wall coherent structures and their dynamics in order to interfere with the bursting process. Various attempts to develop sensors, actuators, and control systems to accomplish this goal are discussed by Bushnell & McGinley (1989), Fiedler & Fernholz (1990), Wilkinson (1990), Gad-el-Hak (1989, 1994, 1996, 2001), Choi *et al* (1993, 1994), Jacobson & Reynolds (1993, 1998), Moin & Bewley (1994), McMichael (1996), Lumley (1996), Ho & Tai (1996, 1998), Pollard (1997), Lumley & Blossey (1998), and Löfdahl & Gad-el-Hak (1999).

At present, MEMS sensor technologies exist that are capable of detecting these vortical

structures in the viscous sublayer via their wall shear stress signature. Detection of high speed sublayer streaks in turbulent boundary layer has been demonstrated in relatively low-speed wind tunnel tests. A variety of sensors are available today that can accomplish this task, including micro hot-wire anemometers, micro surface stress balances, and micro pressure sensors; these are discussed in detail in §6. Moreover, the control algorithms and associated processing electronics necessary to couple such sensors to an appropriate set of microactuators are also relatively well-developed (*e.g.,* Choi *et al* 1993, 1994; Rebbeck & Choi 2001). The required algorithms and processing capabilities are not very far beyond what has already been demonstrated in a number of less demanding low-speed wind tunnel tests. In fact, reduction of surface shear stress has been successfully demonstrated with remarkably simple control algorithms in several laboratory-scale experiments and numerical simulations (*e.g.*, Breuer *et al* 1989; Moin & Bewley 1994; Jacobsen & Reynolds 1998). The principal remaining technical hurdles required to achieve microsystem-based active sublayer control for drag reduction are in the area of microactuators for manipulation of the near-wall coherent structures.

1.3   Previous Microactuator Approaches

Recent experimental and numerical studies specifically related to the development of microactuators for control of near-wall turbulence have been reviewed by Moin & Bewley (1994), Gad-el-Hak (1996, 2001), McMichael (1996), Ho & Tai (1996, 1998), Pollard (1997), Lumley & Blossey (1998), Löfdahl & Gad-el-Hak (1999) and Bewley (2001), among others. Among the earliest actuation approaches for sublayer control was the use of electromagnetic fields to induce a transversally-oscillating Lorentz force on the near-wall region of turbulent boundary layers. Experiments by Nosenchuck & Brown (1993) showed a reduction in wall shear stresses through use of such actuation on a flat plate turbulent boundary layer. Similar results have been obtained in experiments by Henoch & Stace (1995) and in numerical simulations by Crawford & Karniadakis (1997). Numerical simulations by Lim *et al* (1998) showed that such a transversally-oscillating applied magnetic flux can inhibit the motion of the streamwise vortices and reduce their strength.

Simulation results by Berger *et al* (1999) showed similar wall shear stress reductions by electromagnetic Lorentz force actuation in the near-wall region of turbulent channel flow. However, the power required for such actuation has been shown to be at least an order of magnitude larger than the power saved due to the wall shear stress reduction (Lim *et al* 1998).

Carlson & Lumley (1996*a,b*) examined the effect of a local wall-normal deformation applied at the wall – specifically a gaussian "bump" – on the near-wall streamwise vortices. Their direct numerical simulations showed that an appropriately moving bump could produce a local reduction in the wall shear stress. Related numerical simulations of wall deflection, using a combination of sensors and deformable wall actuators to manipulate the streamwise vortices in wall-bounded turbulent flows, have been performed by Mito & Kasagi (1996) and showed almost no drag reduction. However, similar numerical experiments by Endo *et al* (1999) and Kang & Choi (2000) exhibited wall shear stress reductions of 10% and 13-17%, respectively.

Ho & Tai (1996, 1998) and Tsao *et al* (1994) demonstrated an electromagnetically activated microflap actuator that could be deflected to produce an upward velocity in opposition to the wall-normal velocity produced by the streamwise sublayer vortices. This type of actuator showed a limited frequency response of about 100 Hz, and required a relatively high power consumption that would likely offset any drag reduction benefits. More recent work by Sherman *et al* (1999) has attempted to solve some the problems of this earlier microflap actuator by using electrostatically driven, high aspect ratio, large deflection, in-plane microactuators. That study has shown the capabilities of this type of actuator to induce a Stokes' flow pattern in the vicinity of the actuator, but to date this approach has not yet been applied to demonstrate drag reduction in turbulent boundary layers.

Another set of investigations has examined the use of piezoelectrically-driven resonant cantilever actuators to control streamwise vortices in turbulent boundary layers. This type of actuator, first studied by Jacobson & Reynolds (1993), produces a pair of counter-rotating streamwise vortices moving away from the wall. Experiments by Jacobson & Rey-

nolds (1998) in a laminar boundary layer, using two actuators and six sensors, have shown the ability of this type of actuator to displace synthetically generated disturbances. Related to this, a different type of piezoelectric actuator has been used by Rathnasingham & Breuer (1997) to produce a control jet that discharges from a slit into the boundary layer. Using such an actuator with a linear feed-forward control algorithm and three sensors to detect synthetically-generated near-wall structures in a low Reynolds number turbulent boundary layer, they achieved a maximum of 31% reduction in u_{rms}.

Other attempts to control streamwise vortices include the selective suction actuators of Myose & Blackwelder (1995). However, in their experiment the suction was applied between counter-rotating pairs of Görtler vortices in an otherwise steady laminar flow. Direct numerical simulations of turbulent channel flows using a similar actuation methodology, based on local suction and blowing at the wall, was performed by Choi $et\ al$ (1993, 1994). Their most successful result used a control approach in which suction or blowing at the wall was applied in such a way as to be exactly opposite to the wall-normal component of the velocity at $y^+ \approx 10$, yielding 20-30% reduction in skin friction. That control strategy is now commonly termed "opposition control". More recent numerical experiments by Hammond $et\ al$ (1998) showed that the largest wall shear stress reduction is obtained by the use of such an opposition-control strategy based on the wall-normal velocity at $y^+ \approx 15$ above the wall, with the resulting average drag reduction being about 25%. They suggest that the mechanism for this reduction is the creation of a "virtual wall" halfway between the detection plane ($y^+ \approx 15$) and the actuation plane ($y^+ = 0$) that reduces the sweep and ejection events thereby interferes with the transport of high momentum fluid towards the wall and low momentum fluid away from the wall. Despite the success of this opposition-control approach in such numerical experiments, it would be difficult in practice to measure the wall-normal velocity at that distance above the wall. Closely related to these earlier studies, Rebbeck & Choi (2001) applied opposition-control using wall jets created with piston-type actuators. Their experimental investigation, which used a sensor and an actuator in a wind tunnel turbulent boundary layer, exhibited changes in the intensity of near-wall bursting events when the jet was issued into the boundary layer. They suggest that this mechanism will reduce the skin-friction drag because the wall jet pre-

vents high momentum fluid from reaching the wall.

The studies noted above have shown that active sublayer control of turbulent boundary layers is feasible under laboratory conditions, and have demonstrated several types of actuators suitable for active sublayer control under laboratory conditions. However unlike such laboratory-scale demonstration experiments, the turbulent boundary layers on real aeronautical and hydronautical vehicles are typically at much higher Reynolds numbers, and thus involve much smaller length scales and much shorter time scales than are generally achievable in laboratory-scale boundary layers. Furthermore, actuator arrays on real vehicles will be subjected to a variety of non-ideal environmental and operating conditions that are not encountered under laboratory conditions. Practical microactuators for use on vehicles will thus need to be sufficiently robust and infragile to permit operation under such conditions. Finally, the power required for large, dense arrays of such microactuators to achieve the desired level of drag reduction must be sufficiently small to provide a significant net reduction in the power requirements of the vehicle. All of these factors complicate the practical application of existing microactuator technologies to permit active sublayer control for drag reduction on full-scale vehicles under realistic operating conditions.

1.4 Present Work

To date there has been no microactuator technology demonstrated that can meet all of the requirements noted above for a practical microsystem-based approach to active sublayer control for drag reduction on aeronautical or hydronautical vehicles at full-scale operating conditions. By comparison, the requisite wall shear stress and pressure sensor technologies are relatively mature, and the underlying control theory required to link the sensors and actuators is also relatively well developed. The central technology required to achieve practical vehicle control rests largely in the development of robust, high-performance, highly-survivable, low-power microactuators for integration in large, dense arrays that can meet the realistic operating requirements noted earlier.

The present study (Diez-Garias et al 2000, Dahm & Diez-Garias 2001) is the first to examine the electrokinetic principle as the basis for a new class of microactuator arrays that are potentially suitable for active sublayer control on real aeronautical and hydronautical vehicles under practical conditions. The electrokinetic principle, discovered by Reuss (1809) and now used extensively in a variety of applications, involves the interaction between an electric field and mobile ions in the "double-layer" that forms naturally at the phase interface between a suitable electrolyte and a suitable solid material. Under an applied electric field, the mobile ions accelerate as they extract energy from the electric field, and then collisionally transfer this kinetic energy to the molecules that make up the bulk of the electrolyte. In this manner, an applied electric field can induce bulk motion in the electrolyte. The resulting induced electrokinetic flow is typically too weak for most macroscale applications, since the double-layer is extremely thin. However, the Helmholtz-Smoluchowski scaling laws that govern such electrokinetic flow indicate significant performance advantages in microscale applications. As a result, this electrokinetic flow potentially provides a highly efficient means for moving comparatively small amounts of fluid on comparatively fast time scales in comparatively small geometries. In this study these scaling principles are used together with microfabrication technologies and fundamental considerations of the sublayer structure and dynamics to develop, fabricate, and demonstrate microactuators based on such electrokinetic flow that can meet many of the requirements for active sublayer control in turbulent boundary layers on real vehicles.

The electrokinetic microactuator arrays that are the subject of this study seek to interrupt the bursting process associated with naturally-occurring streamwise sublayer vortices in the turbulent boundary layer under conditions that are typical of real vehicles. The sublayer bursting process sets the local rate of momentum transport from the vehicle to the fluid, and thus determines the drag that acts on the vehicle. As noted earlier, the bursting process can be interrupted by manipulating the streamwise vortices in any of a number of ways. In the present microactuator arrays, each individual actuator serves as a local volume source, applied over a brief time interval, at the wall. The actuator thus impulsively displaces a fixed volume of fluid – either positive or negative, corresponding to local suction or blowing – between the wall and the viscous sublayer to induce lateral displace-

ments in the streamwise sublayer vortices. The volume displacement produced by each actuator occurs via electrokinetic pumping in response to an impulsively-applied electric field. Dense arrays consisting of large numbers of such closely-spaced electrokinetic microactuators have been designed and fabricated in this study at scales suitable for active sublayer control at real-vehicle conditions.

Furthermore, a complete system architecture for such microactuator arrays has also developed as part of this study. This novel system architecture is based on groups of actuators within a local "unit cell" operating together in a "response vector" that depends on the signal from a group of collocated wall shear stress sensors. These local wall shear stress sensors determine the "state vector", characterizing the wall shear stress signature produced by the local streamwise sublayer vortex structures in the unit cell. This unit-cell architecture further permits a greatly simplified control logic approach, also developed as part of this study, that is based on a simple look-up table resident in firmware within each unit cell. This lookup table provides the proper unit-cell response vector for the actuators in response to certain state vectors from the unit-cell sensors that correspond to pairs of streamwise sublayer vortices in configurations that correspond to incipient bursting.

This dissertation is organized as follows. Chapter 2 first reviews the essential aspects of the structure of turbulent boundary layers, and then from these determines the required spacing between individual electrokinetic microactuators, the frequency response required of such microactuators, and the equivalent steady flow rate required of such actuators for active sublayer control on a wide variety of full-scale aeronautical and hydronautical vehicle types. Chapter 3 then presents the system architecture developed in this study based on the unit-cell concept for large, dense arrays of such electrokinetic microactuators with collocated wall shear stress sensors and control logic. Chapter 4 describes essential background material related to various electrokinetic phenomena, and then uses this to obtain results for the theoretical steady and unsteady performance of electrokinetic microactuators. Chapter 5 presents results from microfabrication and testing of several generations of such micro-electro-kinetic-actuator (MEKA) arrays, ranging from simple individual capillary actuators to full-scale hydronautical actuator arrays with 25,600 individual elec-

trokinetic microactuators on a 7×7 cm^2 conformally applicable tile (MEKA-5). This chapter also presents results from wind tunnel experiments demonstrating lateral displacement of synthetically-generated streamwise vortices via volume displacements induced at a wall. Chapter 6 presents design results for wall shear stress sensors suitable for integration in such electrokinetic microactuator arrays, together with a microfabrication process sequence for producing large, dense arrays of such collocated sensors in an electrokinetic microactuator array. Chapter 7 summarizes major findings from this study and presents conclusions as to the applicability of the electrokinetic principle as the basis for a practical class of microactuators suitable for drag reduction via active sublayer control on full-scale aeronautical and hydronautical vehicles. An Appendix provides certain results relevant to the performance of slot-type electrokinetic microactuator arrays.

CHAPTER 2

MICROACTUATOR PERFORMANCE REQUIREMENTS

As noted briefly in §1, the bursting process associated with streamwise vortices at the outer edge of the viscous sublayer sets the rate of momentum transport from the wall to the fluid, and hence the drag that acts on the vehicle. Drag reduction can be accomplished by acting on the streamwise vortices to interrupt or otherwise interfere with this sublayer bursting process. For the present microactuator arrays, the individual actuators serve as point volume sources that impulsively displace a fixed volume of fluid in the near-wall region of the flow. Each actuator thus produces locally positive or negative volume displacements over a brief time interval to displace the streamwise sublayer vortices along the spanwise direction. In order to determine the performance requirements of individual microactuators needed to achieve such lateral displacement of the sublayer vortices, this section first reviews essential elements of the structure and dynamics of the near-wall region of turbulent boundary layers. It then uses this information to derive the actuator spacing, frequency, and flow rate requirements necessary to achieve adequate displacement of individual sublayer vortical structures.

2.1   Structure of Turbulent Boundary Layers

Turbulent boundary layers obey a universal structure and scaling under so-called "equilibrium" conditions, which typically apply over the vast majority of a vehicle surface. This makes it possible to approach the problem of vehicle control with a general set of microactuator arrays, rather than having to resort to a separate approach for each vehicle type. It is necessary to be aware of at least the basics of this general structure and its scaling in order

to understand the approach being taken here, and to understand the performance require-
ments that they dictate for microactuator arrays. This section therefore reviews certain
key aspects of the structure and dynamics of equilibrium turbulent boundary layers.

The central issue concerns the form of the mean velocity profile $u(y)$ with increasing dis-
tance y from the vehicle surface (referred to generically as the "wall", located at $y \equiv 0$).
There are two distinct mechanisms that contribute to momentum transport from the wall to
the fluid and then within the fluid above the wall. The first is classical molecular diffu-
sion, with the momentum diffusivity being the "kinematic viscosity" ν, and the second is
turbulent transport by velocity fluctuations in the flow itself. Directly at the wall, the fluid
cannot move and thus the turbulent transport there must vanish. Consequently, for a small
distance above the wall the turbulent transport must therefore remain essentially negligi-
ble. For this reason, there is a layer of fluid adjacent to the wall within which molecular
transport far exceeds turbulent transport. With increasing distance from the wall, the
momentum flux density due to molecular transport must remain roughly constant, while
that due to turbulent transport increases, and thus turbulent transport eventually becomes
the dominant mechanism. The boundary layer therefore naturally has a two-layer struc-
ture – an "inner layer" directly adjacent to the wall within which molecular transport dom-
inates, and an "outer layer" within which turbulent transport dominates. The crossover
between these two transport mechanisms occurs in the outer part of the inner layer and the
inner part of the outer layer – called the "log layer" for reasons that will become evident
subsequently.

Within the inner layer, owing to the dominance of diffusion the momentum flux density
must be roughly constant at a value called the "wall shear stress" τ_w, literally the value of
the shear stress at the wall. All processes within this layer are assumed to be properly
scaled with this wall shear stress, with the viscosity ν, with the fluid density ρ, and with
the distance y above the wall. It is convenient to equivalently express such near-wall scal-
ings in terms of the characteristic velocity defined from these quantities, namely $u_\tau \equiv$
$(\tau_w/\rho)^{1/2}$, often called the "friction velocity", and the characteristic length $l_\tau \equiv \nu / u_\tau$ termed
the "wall unit" or the "viscous length scale". The appropriately scaled velocity profile is

then $u^+(y^+)$, where $u^+ \equiv u/u_\tau$ and $y^+ \equiv y/l_\tau$. The velocity profile throughout the inner layer, when scaled in this manner, is universal for all equilibrium turbulent boundary layers.

Within the outer layer, however, the velocity profile is not entirely universal, and varies somewhat depending on the local boundary layer thickness δ and the local streamwise pressure gradient dp/dx. The latter is determined via the Bernoulli equation by the local Lagrangian acceleration of the fluid outside the boundary layer as it negotiates around the vehicle shape. Thus irrespective of the particular vehicle, the outer layer structure (under equilibrium conditions) can be cataloged in terms of an appropriately scaled pressure gradient parameter Π. Various ways of expressing this scaling have been proposed, with the most successful being the "law of the wake" (Coles 1956). In the overlap region, namely the inner part of the outer layer and the outer part of the inner layer, the velocity profile must become independent of the pressure gradient, and this turns out to demand that the velocity profile in this overlap region must have a logarithmic form – hence the term "log layer". The remainder of the outer layer is referred to as the "defect layer", because its shape is described in terms of the departure (or defect) it demonstrates in relation to the shape that would result if the logarithmic scaling continued there.

Excluding the logarithmic layer, the inner layer extends to about $y^+ \approx 30$, with the region from $0 < y^+ < 10$ termed the "viscous sublayer", and the remainder called the "buffer layer". Thus, the viscous sublayer is about 10 wall units thick, and the inner layer up to the log layer is about 30 wall units thick. The physical thicknesses that these correspond to depend on the value of l_τ, and hence on the wall shear stress (and thus on the boundary layer thickness δ and pressure gradient parameter Π), the fluid density, and the viscosity. These vary depending on the location on the vehicle, its size, its speed, and the properties of the fluid through which it moves.

Due to the dominance of diffusive transport very close to the wall the vorticity there must be uniform, and hence the velocity must increase linearly with distance from the wall. Within the viscous sublayer (*i.e.,* below $y^+ \approx 10$), the form of $u^+(y^+)$ must thus simply be $u^+ = y^+$. This linear velocity profile remains steady until the resulting uniform vorticity layer

adjacent to the wall reaches a thickness beyond which the no-slip requirement at the wall is no longer able to maintain stability of the layer. This instability is governed by the Reynolds number $Re_y \equiv uy/\nu$. Recognizing that in wall variables $Re_y = u^+y^+$ then gives $Re_y = y^{+2}$ within the sublayer, and since such shear-driven instabilities typically begin at $Re \approx O(10^2)$, this would indicate that this uniform layer of vorticity at the wall will remain stable up to about $y^+ \approx O(10)$. This is in good agreement with the lower edge of the buffer layer.

This two-layer structure of turbulent boundary layers is illustrated in Fig. 2.1. In particular, Fig. 2.1a shows typical boundary layer velocity profiles in outer-layer variables (the local boundary layer thickness δ and the local velocity U at the "edge" of the boundary layer) for pressure gradient parameters Π ranging from mildly adverse to strongly favorable. Figure 2.1b shows the same three velocity profiles in inner-layer variables u^+ and y^+, where the linear and logarithmic scalings noted above can be readily identified in the semi-logarithmic axes.

Above the upper edge of the viscous sublayer at $y^+ \approx 10$, naturally-occurring infinitesimal disturbances cause the otherwise uniform vorticity layer to develop sinusoidal instabilities along the spanwise (cross-stream) direction, denoted z. Amplification and nonlinear growth of this spanwise instability leads to the formation of elongated concentrations of vorticity oriented along the streamwise direction, denoted x. As shown in Fig. 2.2, the resulting streamwise vortical structures at the outer edge of the viscous sublayer have a spacing, in the scaled spanwise coordinate $z^+ \equiv z/l_\tau$, of about $z^+ \approx 100$. The length of these "sublayer vortices" is typically about $x^+ \approx 1000$, but varies from about $400 - 1500$. In other words, the sublayer vortices are about 1000 wall units (l_τ) long, and are spaced about 100 wall units apart. Since the vortices are located roughly 10 wall units above the wall, they will advect at a speed $u^+ \approx 10$, and thus move over any fixed point on the wall with a frequency of about $f^+ \approx 10^{-2}$.

Figure 2.2 is an illustration of the pattern of these streamwise sublayer vortical structures in the near-wall region of turbulent boundary layers. In particular, Fig. 2.2a shows a typi-

cal example of the instantaneous structure of these vortices, such as has been documented in numerous direct numerical simulations of turbulent boundary layers. Note that the structures are not spaced at precisely equal intervals, nor do they have precisely equal lengths, however it is common to idealize this pattern as shown in Fig. 2.2*b* with the characteristic dimensions as noted above.

2.2   Bursting of Sublayer Vortices

It is these streamwise vortices at the outer edge of the viscous sublayer that are the key to momentum transport from the inner layer to the outer layer and thus from the wall to the inner layer, and hence determine the drag that acts on the vehicle. The detailed dynamics of the near-wall structures are complex and remain the subject of considerable controversy, however, the essential mechanism can be understood within the context of a simple inviscid description. Under the influence of their mutual Biot-Savart induced motion as well as that of their images on the opposite side of the wall, these streamwise vortices must naturally group into pairs having alternating sense of circulation. Each streamwise vortex pair remains nominally steady until the combined induced motion of the two elongated vortices abruptly lifts them away from the near-wall region and into the outer layer, in a process termed "bursting". In doing so, low momentum fluid in the wall-fixed coordinate frame (high momentum fluid in an absolute frame) is transported from the inner layer to the outer layer, at a much greater rate than would be the case by diffusion alone. It is due to this bursting mechanism and the accompanying greatly increased rate of momentum transport from the wall to the fluid that turbulent boundary layers produce far greater drag on a vehicle than do laminar boundary layers. The bursting process is recognized as the main source of turbulence production in turbulent boundary layers (Kim *et al* 1971; Blackwelder & Eckelman 1979; Cantwell 1981; Robinson 1991).

While it is accepted that the streamwise vortices are critical in this process, the evolutionary dynamics behind the bursting process are not yet clear. Earlier reviews of the bursting process (Robinson 1991 and references therein) explained that low-speed streaks of fluid,

generated by streamwise vortices, were ejected outward from the wall after going through some transitional oscillations, generating most of the turbulence production in the boundary layer. Further studies of this process during the last decade aided but the use of DNS simulations has modified some of those earlier concepts. DNS simulations (Hamilton *et al* 1995) have proposed a mechanism for the regeneration of near-wall turbulence structure. This includes the formation of streaks by streamwise vortices, and the breakdown of streaks and regeneration of the streamwise vortices. The formation of high and low speed-streaks is generated by the "sweeping" and "ejection", respectively, of near-wall fluid by the coherent structures towards the wall or away from the wall. This process, also described by Jeong *et al* (1997) as cross-stream advection generated by the vortical structures, is a major source of negative and positive Reynolds stress in the boundary layer. Schoppa & Hussain (2000*a,b*) have indicated that the wallward motion enhances the drag and heat transfer by steepening the wall gradient of streamwise velocity. This has been confirmed by Orlandi & Jiménez (1994). Further simulations by Jeong *et al* (1997) have shown that the coherent structures are elongated quasi-streamwise vortices inclined nine degrees in the vertical plane and tilted in the horizontal plane. Furthermore, they indicate that vortices of alternating sign overlap in the streamwise direction. Schoppa & Hussain (2000*a,b*) have successfully used this later model to show that combined transient growth and instability of lifted, irrotational low-speed streaks generates new streamwise vortices. Thus completing the regeneration cycle of the turbulent fluctuations in the boundary layer. These recent simulations have shown that "bursting" process does not require a "violent" break up of the streaks. Instead, this is rather a dynamic process by which growing disturbances of ejected low-speed streaks generate new streamwise vortices, and the mechanism by which these new streamwise vortices extract energy from the mean flow to create alternating low- and high-speed streaks (*e.g,* Jiménez & Pinelli 1999; Gottero & Onorato 2000; Schoppa & Hussain 2000*a,b*).

2.3   Sublayer Control Principles

Interrupting this delicate, nonlinear, Biot-Savart-induced lifting mechanism between adja-

cent streamwise sublayer vortices before bursting can occur has long been an objective in fluid mechanics and aerodynamics. As noted in §1, it has been demonstrated both in laboratory experiments and in numerical simulations that this can be accomplished by acting on the streamwise vortices in any of a number of ways so as to offset the Biot-Savart induced velocities that lead to the sudden bursting. For the present microactuator arrays, the individual actuators serve as point volume sources that displace (either positively or negatively) a fixed volume of fluid between the wall and the inner layer. This is shown schematically in Fig. 2.3. The motion that this volume source field induces serves to displace the streamwise vortices along the spanwise direction, thereby locally increasing or decreasing the separation between the two elongated vortices in a streamwise vortex pair. This counteracts the Biot-Savart induced motion of the vortices on each other, thus interrupting the bursting process.

As for a closed-loop feedback control approach that drives an array of such individually addressable "point" microactuators, there are two schools of thought regarding the best way to do this. The first, which may be termed the "deterministic" approach, is to use sensors to identify the wall shear stress or wall pressure signature of a pair of streamwise vortices that are about to burst, and then use collocated actuators to manipulate the vortices in such a way as to delay or defeat the bursting process. An example of this is the "opposition control" approach (Choi *et al* 1993, 1994; Hammond *et al* 1998; Rebbeck & Choi 2001) discussed briefly in §1. The second, which might be termed a "stochastic" approach, ignores the detailed dynamics of the bursting process itself and instead uses an artificial intelligence procedure. In that case, a neural network between a group of sensors and actuators is trained over time in such a way as to minimize the wall shear stress. Both approaches have met with considerable and roughly comparable success in laboratory experiments and in numerical simulations, demonstrating reductions in the range of 20-30% in the wall shear stress.

The scenario outlined above involves *closed-loop* control of the *equilibrium* structure and dynamics of the boundary layer. An alternative uses *open-loop* control of the *nonequilibrium* dynamics in the near-wall region of the boundary layer. This is motivated by experi-

mental and numerical observations showing that, when a boundary layer is subjected to a sudden transverse pressure gradient or crossflow, the flow experiences temporary reductions in its turbulent transport. This suggests that it may be possible to sustain this effect by maintaining the boundary layer in a continual nonequilibrium state. One way this might be done is through spanwise oscillations of the wall relative to the streamwise vortices (*e.g.*, Jung *et al* 1992, Akhavan *et al* 1993, Laadhari *et al* 1994). Experiments and numerical simulations have shown that this produces significant reductions in turbulent transport and thereby reductions in the wall shear stress of up to 40%. The effectiveness depends on the oscillation frequency, with optimal drag reduction again occurring at $f^+ \approx 10^{-2}$. Moreover such an approach does not require any collocated array of sensors to determine the instantaneous pattern of sublayer vortices, or control logic to discern from this the appropriate set of actuator signals. The only requirement is for an occasional sensor to measure the average wall shear stress, which is needed to properly scale the oscillation frequency to achieve optimal drag reductions. This "oscillating wall" approach thus potentially provides a means for open-loop control of the sublayer vortices, and thus obviates the difficulties associated with collocating large arrays of sensors, actuators, and local processing. In practice, it is the fluid above the wall that would be oscillated by a set of microactuators designed to generate volumetric displacements above the wall and thereby induce oscillatory spanwise motions of the fluid in the inner layer. However, while the inherent simplicity of open-loop control based on this oscillating wall approach is appealing, Appendix A shows that it cannot be practically implemented with the electrokinetic microactuators that are the subject of this study. This study therefore focuses on closed-loop control using electrokinetic microactuator arrays with a collocated array of sensors and appropriate control processors.

2.4 Actuator Spacing, Frequency, and Flow Rate Requirements

Irrespective of the control approach used and the microactuator type it implies, it is necessary to have an array of actuators that allow the streamwise sublayer vortices to be acted

upon appropriately. Key performance requirements involve the microactuator spacing, frequency, and flow rate needed to achieve adequate displacement of individual sublayer vortical structures. For closed-loop control approach based on individual point microactuators, from the forgoing summary of the sublayer vortex structure and dynamics it is apparent that such actuators must be separated by typically 100 wall units, and displace a volume of fluid with an equivalent hemispherical radius of the order of 10 wall units l_τ, with a step response that corresponds to a scaled frequency of $f^+ = 10^{-2}$.

With this information, it is possible to determine the size and performance requirements to which these conditions correspond for various types of vehicles. These performance requirements will depend on the fluid type (principally air or water, which differ in their density and viscosity), the vehicle speed, and the vehicle length. More precisely, the universal structure and scaling of equilibrium turbulent boundary layers shows that the local sublayer properties, and hence the local microactuator performance requirements, depend on the local boundary layer thickness δ, the local fluid speed U at the "edge" of the boundary layer, the local pressure gradient dp/dx, and the fluid properties ρ and μ. Of these, the direct effect of the pressure gradient is relatively weak; it is the indirect effect of the pressure gradient on the boundary layer thickness δ that dominates. This permits an analysis for each vehicle type without requiring a detailed boundary layer calculation for a specific vehicle geometry. In effect, the performance requirements can be obtained at any streamwise position on the vehicle for a variety of pressure gradient parameters Π ranging from strongly favorable to moderately adverse by evaluating u_τ as described in §2.1. This means solving for τ_w, which can be written as

$$\tau_w = \frac{\nu U^2}{\lambda^2} \tag{2.1}$$

In (2.1), λ can be obtained by solving the equations

$$\lambda = \frac{1}{\kappa} \ln\left(\frac{\mathrm{Re}_\delta}{\lambda}\right) + 5 + \frac{2\Pi}{\kappa} \tag{2.2}$$

and

$$\beta = \left(\frac{1+\Pi}{\kappa\lambda}\right)\frac{\delta}{\tau_w}\frac{dp}{dx} = -0.4 + 0.76\Pi + 0.42\Pi^2 \tag{2.3}$$

where $\kappa = 0.41$, $Re_\delta = (0.057 x U Re_x^{-1/13})/\nu$ and the polynomial shown in (2.3) is a fit to a large number of turbulence boundary layer data done by Das (1987).

Accordingly, Fig. 2.4 shows the results obtained for the required point microactuator spacing and frequency response at four downstream locations ($x/L = 0.25, 0.5, 0.75,$ and 1.0) and for four different pressure gradients. Vehicles for which results are shown in this figure are summarized in Table 2.1. It is apparent, both from the results shown and from fundamental considerations, that vehicle speed is the principal factor that drives both the actuator spacing and frequency requirements. These requirements are relatively benign for the UAV application, where actuator spacings of several millimeters and step response of 100 Hz are sufficient to act on virtually every sublayer streak. At the other extreme, the supersonic fighter and transport aircraft require actuator spacings of 100-200 μm and step response of 10-90 kHz. The various hydronautical applications, which differ from the aeronautical applications due to the $O(10^{-3})$ lower kinematic viscosity, require microactuator spacings roughly 300 μm but frequencies of only about 1 kHz. Figure 2.5 gives the equivalent DC volume flow rate which the microactuators must be able to achieve for each of these vehicle types in order to impulsively displace the required volume of fluid during the available sublayer vortex passage time. Of key relevance is that the flow rate requirements for hydronautical applications are typically one to two orders of magnitude lower than for aeronautical applications. For essentially all the hydronautical applications, the equivalent steady flow rate required is in the range of 10 μL/min.

For electrokinetic microactuators that are intended for use in dense arrays, the maximum flow rate achievable by each actuator is limited by the area per actuator available for the electrokinetic pumping channels, as will be seen in §4. As a consequence, the flow rates in Fig. 2.5 are closely connected with the microactuator spacings in Fig. 2.4. This is shown in Fig. 2.6, where the maximum flow rate achievable is shown as a function of the spacing between individual microactuators within the array. The dashed line shows the result for simple geometric scaling of a given actuator design, for which the flow rate Q increases with actuator spacing l as $Q \sim l^2$. The practical implication of this is that a microactuator array designed for use in full-scale hydronautical applications can simply

be geometrically scaled-up in size by a factor of 15 to provide the required microactuator array for a UAV-scale aeronautical application. The other aeronautical applications, however, would require microactuator arrays that can achieve higher electrokinetic pumping efficiencies, namely higher values of the equivalent DC flow rate Q per unit microactuator area l^2. For this reason the MEKA-5 microactuator array developed in this study (see §5) has been designed for full-scale hydronautical applications, with 25,600 individual electrokinetic microactuators arranged on 325 µm center-to-center spacings in a 7×7 cm^2 array. The same array can be directly scaled up – with no increase in per-actuator performance required – for the UAV-scale application.

These frequency and flow rate requirements represent what is needed to act on essentially every streamwise vortical sublayer structure in the turbulent boundary layer. While the actuator spacing requirements are inflexible, adequate control may be possible with somewhat lower frequency performance. This would involve acting on some, but not all, of the sublayer vortical structures. In fact, it is only necessary to act on those structures that are at the point of incipient bursting, since it is this vortex bursting phenomenon that the microactuators are intended to suppress.

Vehicle class	Length (m)	Speed (m/s)	l_τ (μm)	f_τ (kHz)
Transport aircraft (wing)	3	200	1.8-3.1	15-41
Supersonic fighter (wing)	5	300	1.3-2.1	30-80
UAV (wing)	1	30	25-54	0.05-0.22
Naval surface ship (hull)	180	30	3.6-5.0	0.41-0.84
Submarine (hull)	170	10	2.9-4.2	0.5-1.2
Torpedo	5	10	2.7-4.5	0.5-1.4
Automotive (body)	2	30	10-19	0.4-1.4

Table 2.1.   Full-scale aeronautical and hydronautical vehicles types considered in §2.4, giving overall vehicle length L and speed U used to obtain viscous sublayer characteristics for various values of the pressure gradient parameter Π at locations x/L = 0.25, 0.50, 0.75, and 1.00. The resulting l_τ values determine the required performance characteristics shown in Figs. 2.4-2.6 for active sublayer control on each vehicle type at full-scale operating conditions.

(a)
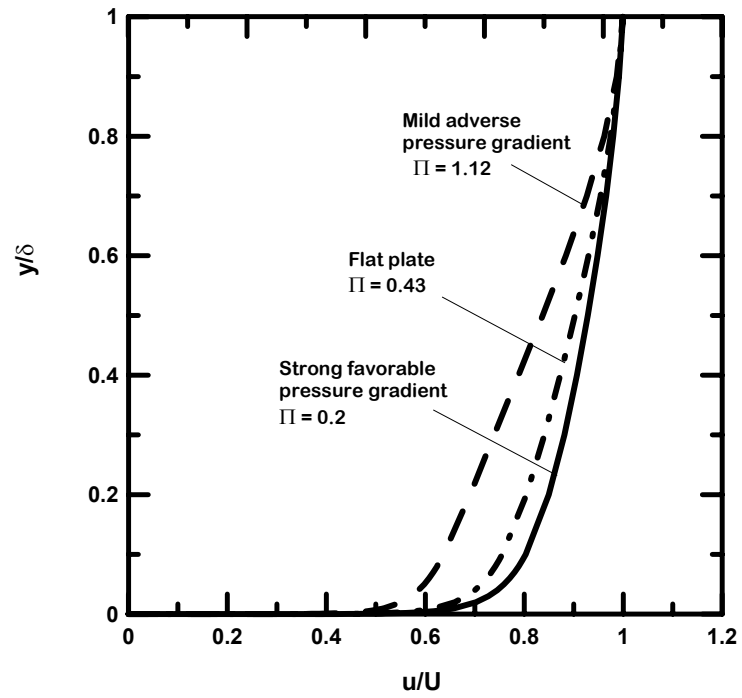
(b)
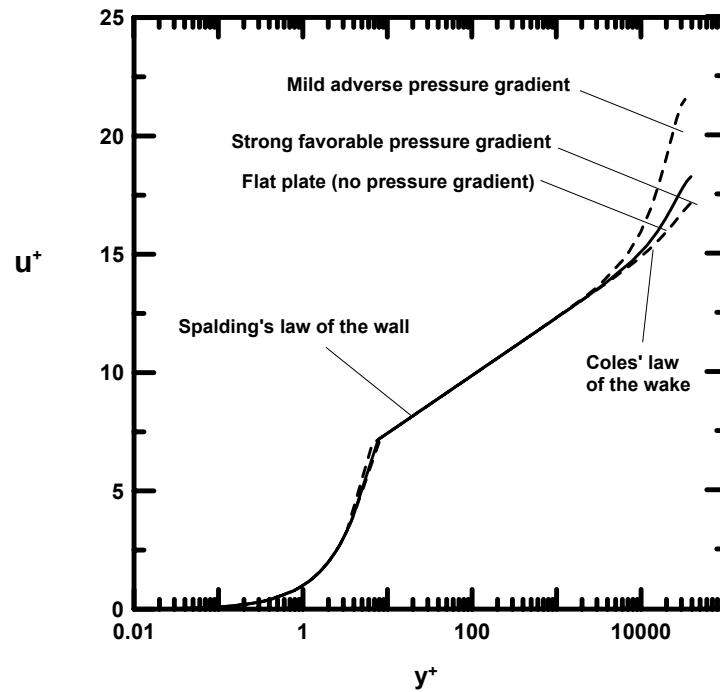
Figure 2.1.　　Typical mean velocity profiles in turbulent boundary layers for different values of the pressure gradient parameter Π, showing the resulting profile shape in *(a)* outer-law variables, and *(b)* inner-law variables.

(a)
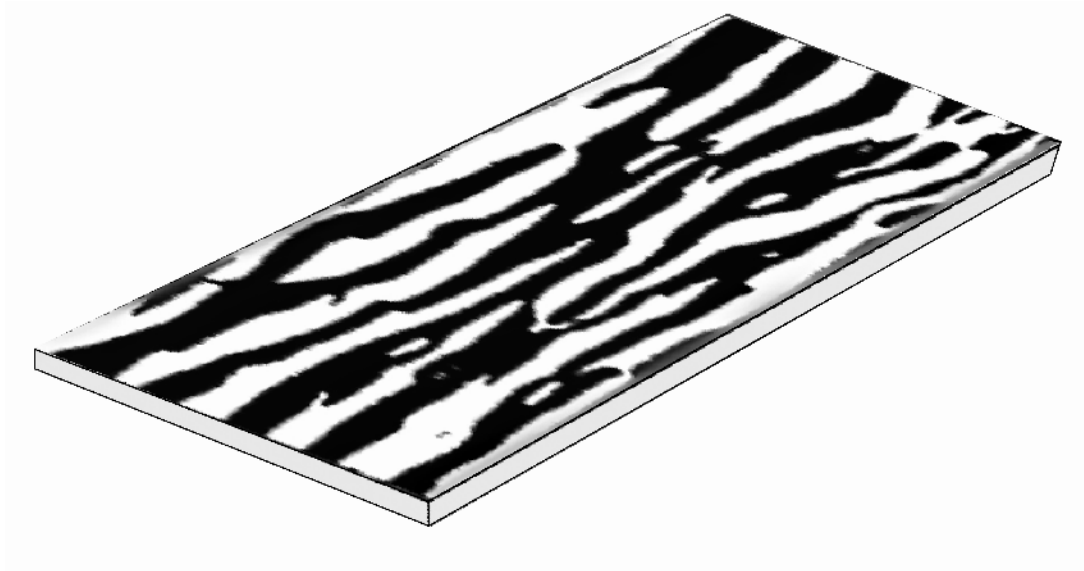
(b)
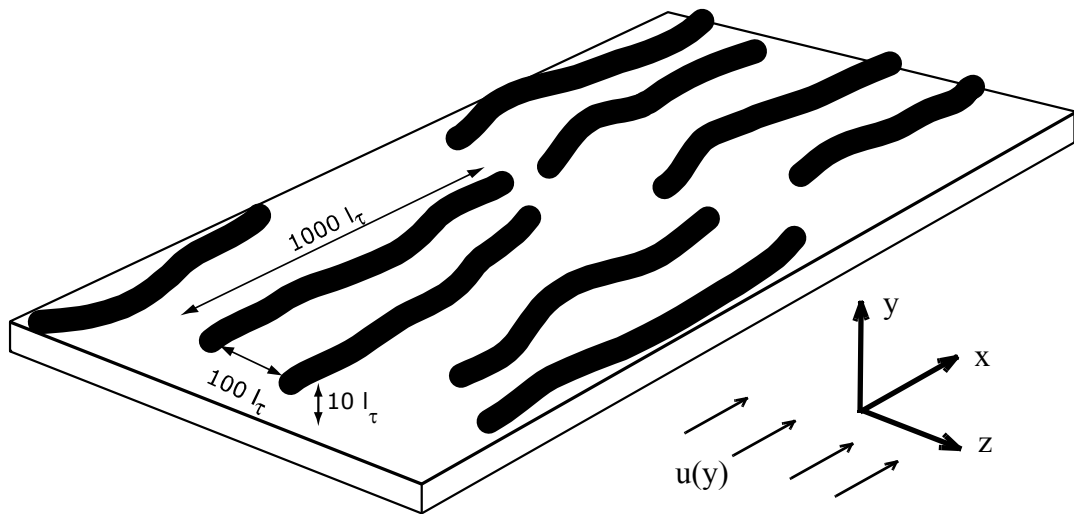
Figure 2.2.   Schematics indicating the structure of streamwise vortices in the near-wall region of turbulent boundary layers, showing *(a)* typical pattern of high- and low-speed streaks, and *(b)* idealized representation of the near-wall streamwise vortical structures.
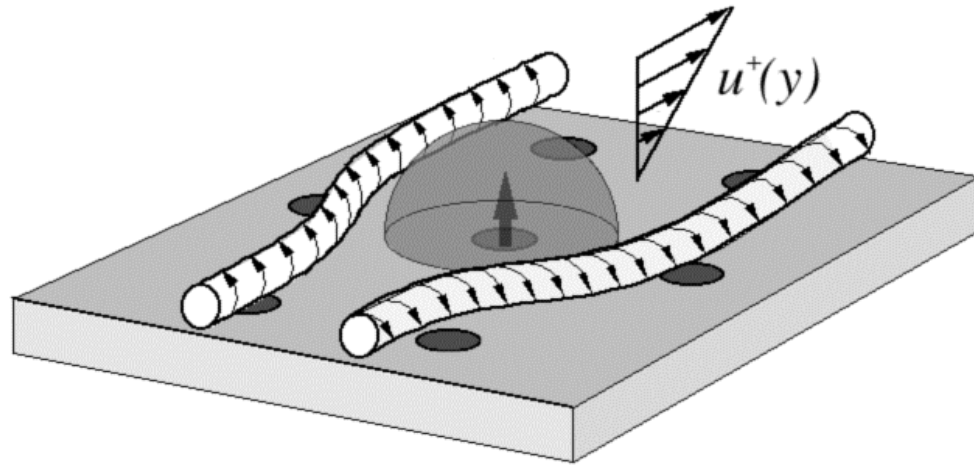
Figure 2.3.   Idealized notional representation showing the lateral displacement of streamwise sublayer vortices induced by volumetric pumping from an actuator. Note that the Reynolds number Re associated with the flow issuing from the actuator must be $O(1)$ or smaller, so that the actuator flow serves as a point volume source to provide effective lateral displacement. At larger Re values, the flow issuing from the actuator would fundamentally change to become jet-like, and would then no longer induce effective lateral displacements.
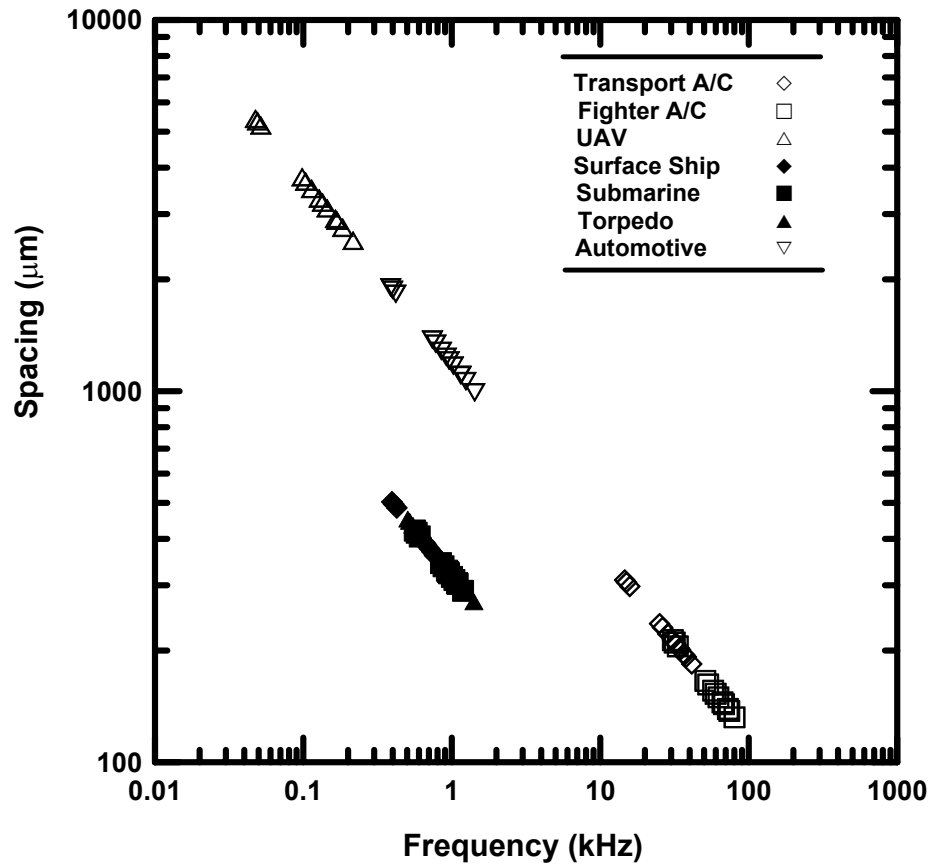
Figure 2.4.   Microactuator spacing and frequency requirements for active sublayer control by manipulation of streamwise vortical structures as indicated in Fig. 2.3, showing results for aeronautical and hydronautical vehicle types listed in Table 2.1. Note that hydronautical applications all require microactuator arrays with approximately 300 μm actuator spacings and 1 kHz frequency response.
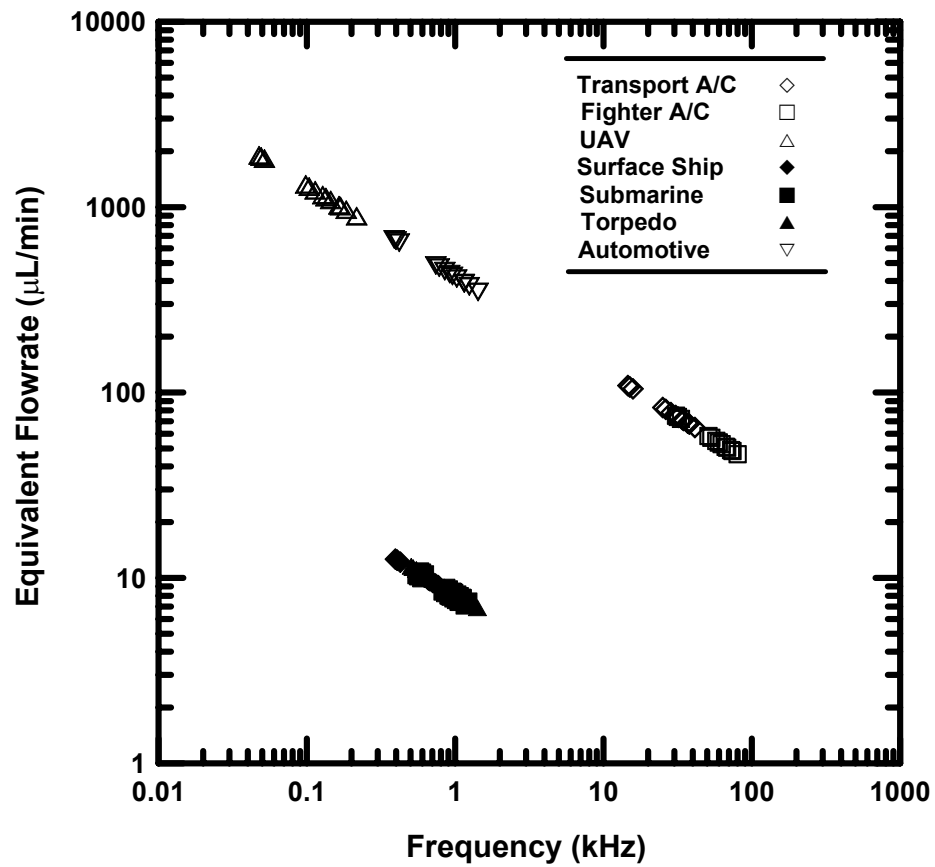
Figure 2.5.   Equivalent steady volumetric flow rates required for active sublayer control by manipulation of streamwise vortical structures as indicated in Fig. 2.3, showing results for aeronautical and hydronautical vehicle types listed in Table 2.1. Hydronautical applications only require flow rates in the range of 10 µL/min, while aeronautical vehicle applications typically require one to two orders of magnitude larger flow rates.
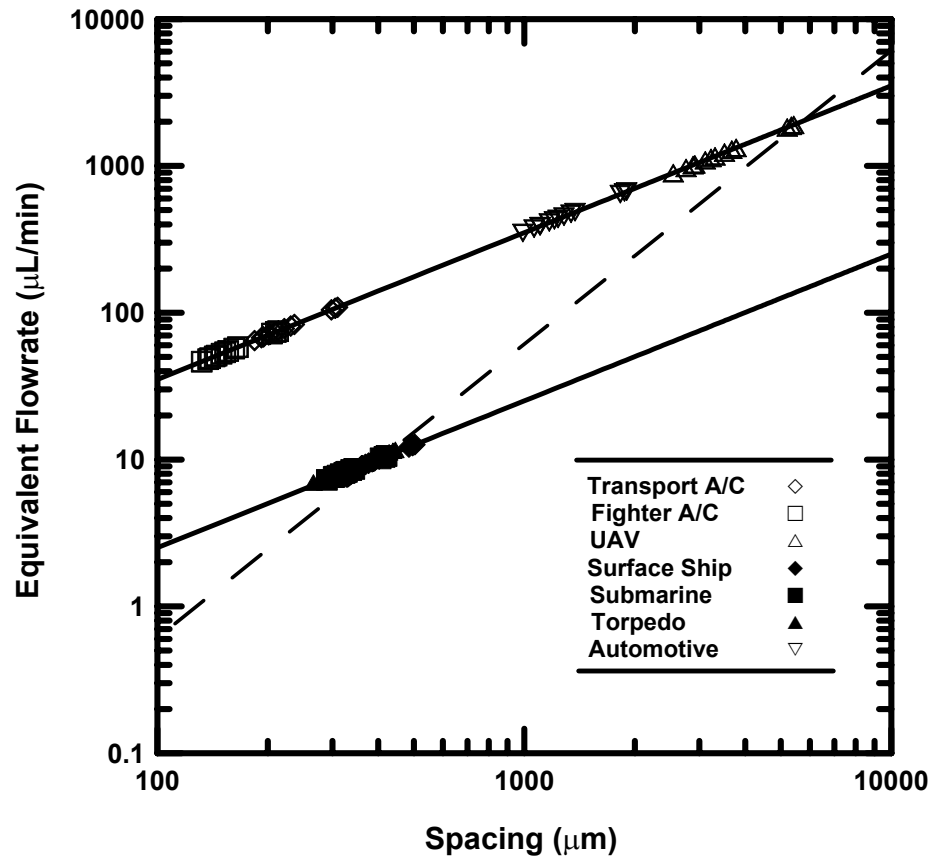
Figure 2.6.   Combined results from Figs. 2.5 and 2.6, with dashed line showing coupling between microactuator spacing and flow rate, as noted in §2.4, corresponding to simple geometric scaling of any given microactuator design. Increased actuator spacings provide increased area for electrokinetic pumping channels, which in turn provide for larger volume flow rates.

CHAPTER 3

SYSTEM ARCHITECTURE FOR MICROACTUATOR ARRAYS

The small actuator spacing required for sublayer control on real vehicles, as seen in §2, implies that large and dense arrays of microactuators must be used to cover key parts of the vehicle surface, as indicated in Fig. 3.1. However, the inherently local nature of the sublayer vortex dynamics and bursting process suggests that such large arrays can be composed of much smaller independent "unit cells", each with their own sensors, control processing, and actuators. This highly local nature of the problem thus permits a system architecture for such microactuator arrays that greatly simplifies the sublayer control of turbulent boundary layers. This section describes a system architecture, developed as part of this study, based on this unit-cell concept that is sufficiently simple to realistically permit integration of the present electrokinetic microactuators into a complete system for active sublayer control on full-scale vehicles under realistic operating conditions.

3.1   Unit Cell Concept

The typically 300 μm spacing between microactuators required for hydronautical vehicles of 100 m scale, such as a submarine hull, implies that of the order of 30 billion individual microactuators would be required to cover the entire vehicle surface. The massive difficulty of integrating such a large number of actuators, with a comparably large number of sensors and an appropriate control processing capability, can be greatly simplified by taking advantage of the inherently local nature of the sublayer structure and dynamics. In particular, the length of the sublayer vortices typically extends over only about 1000 wall units l_τ, and the bursting process occurs between adjacent counter-rotating pairs of these

31

vortices that are typically separated along the spanwise direction by only about 100 wall units l_τ and are typically located about 10 wall units l_τ above the wall as noted in §2. Moreover, the bursting process itself is principally dependent on the separation between the pair of counter-rotating sublayer vortices, and is largely independent of the locations and dynamics of other distantly-located sublayer vortices. This inherent locality suggests that sublayer control of the turbulent boundary layer over the entire vehicle can be broken down into elementary "unit cells", the size of which is set by these length scales associated with the bursting process. Moreover, this also suggests that dynamical interactions between such unit cells should be comparatively weak in relation to the interactions between sublayer vortices within a given unit cell. Any such interactions would extend at most to the next adjacent unit cells, and to a good approximation such cell-to-cell interactions could be neglected altogether. The unit cells then become fully independent, each with their own sensors, control processing, and actuators. Since the number of sensors and actuators within such unit cells is then relatively small, the problem of integrating them into a complete control system becomes correspondingly simpler.

The extent of this simplification depends on the minimum length scale to which these unit cells can be reduced. The 1000 l_τ average length of the near-wall structures suggests that this is the maximum dimension along the streamwise direction that could be required for such unit cells. Further reduction is possible by recognizing that incipient bursting occurs far more locally than this, over a smaller length of the sublayer vortex pair. A reasonable upper limit on the required streamwise dimension of the unit cells would thus be about 500 l_τ to allow detection of the incipient bursting configuration and subsequent actuation to interfere with this process.

In the spanwise direction, the coherent structures are separated, on average, by about 100 wall units l_τ. Since sublayer control involves acting on pairs of such sublayer vortices near incipient bursting, and since dynamical interactions via Biot-Savart induction are significant only between adjacent vortices, it appears reasonable that the spanwise dimension of the unit cell should be large enough to accommodate a given vortex pair and its next adjacent spanwise neighbors. This would suggest that a spanwise dimension of 500 l_τ, equal

to the streamwise dimension of the unit cell, would be sufficient. Unit cells much larger than this would not appear to be necessary, and would simply increase the number of sensors and actuators that must be integrated into the local unit-cell control system.

Based on this reasoning, the fundamental size of the unit cells in this system architecture is 500 l_τ in both the streamwise and spanwise directions. Moreover, the 500 $l_\tau \times$ 500 l_τ unit cells in this architecture are taken to be completely independent of each other, though cell-to-cell interactions between adjacent unit cells could be readily incorporated by having each of the cell-based control processors share information with adjacent cells.

Figure 3.1 schematically shows how this concept can be used to group the sensors, actuators, and processing over an entire vehicle into such unit cells, each composed of an $n \times n$ arrangement of elementary sensor and actuator pairs together with local unit-cell processing capability. Given the unit-cell dimensions noted above and the actuator spacings noted in §2, it is apparent that n will typically be in the range of $4 \leq n \leq 6$.

Furthermore, the relatively small number n^2 of sensor-actuator pairs in each such unit cell allows the resident processing capability that "connects" these sensors and actuators to be greatly simplified. While most previous work has examined comparatively elaborate control processing approaches based on fundamental control theory, many of which require comparatively sophisticated local processing capability to implement, the unit-cell approach permits investigation of potentially far simpler methods. In particular, the number of sensors and actuators is sufficiently small that true "processing" at the unit-cell level may be discarded entirely, and replaced by a simple "look-up table" approach. In this case, the actuator states are directly implied by the sensor states via a look-up table stored in a simple programmable logic array (PLA) in each unit cell. In this manner, on each clock cycle the new sensor states are used to determine the new actuator states, thus eliminating the need for any true processing capability. Additional details of this look-up table approach, including how the look-up table in the PLA is determined, are discussed in §3.3.

Moreover, given the typical dimensions of these unit cells and the dimension of the silicon wafers on which microfabrication technologies, such as photolithography and other MEMS processes, can be used to parallel-fabricate large numbers of such unit cells, it is natural to group these unit cells into "tiles", as also shown in Fig. 3.1. Each tile contains the number of unit cells that can be fit into a square array on a single wafer. For typical unit-cell sizes and wafer sizes, this dictates roughly 250×250 unit cells in each tile. Each tile has a single pair of electrical leadouts, with an internal bus structure that distributes power to each of the unit cells. These tiles form the basic elements used to cover desired parts of the vehicle surface on which sublayer control is to be accomplished.

Note that this novel system architecture based on the unit-cell approach and the considerable simplifications that it implies for active sublayer control systems are essentially independent of the type of actuators or sensors used. A similar architecture could be applied to many different types of active sublayer control approaches, with similar practical advantages for realistically implementing active sublayer control.

3.2 Unit Cell Components

As indicated in Fig. 3.2, each unit cell in this system architecture is composed of a collocated array of wall shear stress sensors, electrokinetic microactuators, and local digital signal processing (DSP) capability. This section briefly describes the key aspects of the major components that make up each of the fully-independent unit cells on each tile, consisting of an $n \times n$ array (with typically $4 \leq n \leq 6$) of sensors and actuators connected via the unit-cell control logic.

3.2.1 Microactuators

Each unit cell contains an $n \times n$ array of electrokinetic actuators that provide the volume displacements within the near-wall region of the turbulent boundary layer to laterally displace the streamwise sublayer vortices. Although the fundamental unit-cell architecture

can accommodate essentially any type of actuator, the electrokinetic microactuators that are the principle focus of this study offer several benefits that make them potentially well suited for active sublayer control. The electrokinetic principle on which these microactuators function (see §4) requires no moving parts, with the volumetric pumping being induced by an impulsively applied electric field. As a result, these electrokinetic microactuators can be significantly more robust than many other actuators based on moving parts. Moreover, the scalings that govern the electrokinetic effect provide significant performance advantageous for actuators fabricated at the microscale. In particular, such electrokinetic microactuators can achieve an extremely high impulse response, and equivalent steady flow rates sufficient to meet the requirements noted in §2 for active sublayer control under full-scale vehicle operating conditions. Such microactuators can also be readily sized to fit with the unit-cell architecture, and do not involve any parts that protrude into the flow.

Furthermore, such electrokinetic microactuators can be fabricated with a comparatively simple three-layer design, as indicated in Fig. 3.3. This design involves a top layer containing the individual actuator nozzles and electrodes together with leadouts to the unit-cell DSP, a middle layer containing the electrokinetic driver channels filled with a porous polymer matrix in which pumping of the electrolyte occurs, and a bottom layer that serves as a common electrolyte reservoir for the unit cell (or, alternatively, for the entire tile).

Power for the electrokinetic microactuators is distributed throughout the tile via a simple bus structure composed of parallel horizontal and vertical line conductors in the top layer across the entire tile, as indicated in Fig. 3.2. The common electrolyte reservoir serves as the other electrode. The high level of redundancy provided by the top-layer bus structure ensures continuity of a conductive path to all actuators on the tile even in the event of a local damage site on the tile or a local failure along any of the line conductors. A set of leadouts run within the top layer from each individual actuator electrode to a terminal located near one of the common power bus lines. On each clock cycle, the DSP selectively connects each electrode terminal to the power bus, with either positive or negative

polarity, to provide for positive or negative volume displacement by each individual actu-
ator, or else leaves this connection open to provide for zero displacement by the actuator.

3.2.2 *Sensors*

Detection of streamwise vortical structures at the upper edge of the viscous sublayer is
accomplished by an $n \times n$ array of wall shear stress sensors collocated with each microac-
tuator in the unit cell. The detailed design and fabrication of the wall shear stress sensors
is discussed in §6. The unit-cell architecture in Fig. 3.2 uses one wall shear stress sensor
for each actuator, located between adjacent actuators.

Many of the usual concerns about shear stress sensor calibration and accuracy can be
relaxed in this system approach, since the role of each sensor is not to measure the wall
shear stress distribution below the vortical structures, but rather simply to identify the
presence of a vortical structure just prior to bursting with reasonably high probability of
detection. Thus the instantaneous wall shear stress sensor outputs can be compared to a
local running average value obtained from a simple (*e.g.*, RC) low-pass filter located in
the resident DSP on each unit-cell. When the sensor output exceeds a preset multiple of
this running average, then the state of the i-th sensor in the processing electronics is set to
$S_i = 1$ (or to $S_i = \pm 1$ if the sensors have directional capability). Otherwise the input from
the sensor is set to $S_i = 0$. A simple circuit design that generates the sensor state S_i corre-
sponding to each wall shear stress sensor is shown in Fig. 3.4. The sensor states are shown
schematically in Fig. 3.5.

The complete set of sensor states $\{S_i\}$ for $i = (1, 2, ..., n_S)$, where n_S is the number of sen-
sors in each unit cell, provides the input to the unit-cell processing electronics. The run-
ning average essentially eliminates the need for calibrating each sensor, and eliminates
difficulties caused by changes in the vehicle speed and attitude or by the particular loca-
tion of the sensor-actuator pair on the vehicle. Sensor drift over time scales significantly
longer than the averaging time thus becomes irrelevant, and sensor accuracy does not need
to be high since the sensor output is thresholded in the manner described above.

Since all interactions between the sensors and actuators occur at the unit-cell level, each unit cell contains its own independent processing capability. Because of the relatively small unit-cell size that the dynamics of the sublayer bursting process allows, it may be possible to greatly reduce the required sensor capabilities and unit-cell processing capabilities. The role of the local unit-cell processing is to use the n_S sensor states $\{S_i\}$ on each clock cycle to determine the n_A actuator states $\{A_i\}$, where $A_i = +1$, 0, or -1 corresponds respectively to positive volume flux (blowing), zero volume flux, or negative volume flux (suction). Note that the actuators are not modulated; they are either *on* (± 1) or *off* (0). Thus the voltage of the top-layer electrode for each actuator is set to $A_i V_{ref}$, where V_{ref} is the voltage of the common power bus that runs between the unit-cells. The processing circuit thus effectively acts as a three-state bridge between this power bus and the electrode contact for each of the microactuators in the unit-cell. The relationship between the sensor state vector and the actuator state vector is via a simple lookup table, described in the following section.

3.3   Look-Up Table Control Logic

The set of sensor states $\{S_i\}$ implies a set of actuator states $\{A_i\}$. Functional approaches of the type $\mathbf{A} = f(\mathbf{S})$ may be appealing in their generality and rigorous connection to control theory, but are likely to require significantly more processing capability than can be readily accommodated within each unit-cell. Moreover, such an approach would overlook the fact that the physics of the sublayer structures greatly restrict this functional dependence and thus provide opportunities for considerable simplification. For example, since the processing is purely local at the unit-cell level and the unit-cell size can be made relatively small, it may be possible to use a simple look-up table approach (*e.g.*, a programmable logic array) that eliminates the need for complex processing, as indicated schematically in Fig. 3.6.

Such a look-up table approach can be implemented at various levels of approximation. The simplest is to make use of the nominally streamwise structure of the sublayer vortices, and thereby reduce the number of spatial dimensions in both the sensor and actuator arrays to just one. This can be done by logically grouping the n_S sensors in the unit cell into nC_S columns along the streamwise direction, and then obtaining a single sensor column state CS_i for each column (*e.g.*, by a majority rule among the sensor states $\{S_i\}$ within the column). Similarly, the n_A actuators are grouped into streamwise columns, and a single actuator column state CA_i is used to drive all the actuators in that column. This reduces the logic circuit requirements to setting the nC_A-element column state vector $\{CA_i\}$ from the nC_S-element column state vector $\{CS_i\}$, and can be done by the programmable logic array shown schematically in Fig. 3.7. In that case, the logic array may contain a set of matrix coefficients that provide the actuator state vector for any given sensor state vector, as indicated in Fig. 3.8.

For the relatively small number of columns provided by the unit-cell architecture, the number of possible sensor column vector combinations may be sufficiently small that each of the appropriate actuator column vectors can be explicitly determined from simple model-based considerations. Alternatively, irrespective of whether the unit-cell processing is to be done in one or two spatial dimensions, since the lookup table remains static and is the same for all unit-cells it can be generated from a detailed simulation study. This might be done by a neural net approach that evolves to determine a look-up table which minimizes the wall shear stress within a unit-cell from discrete thresholded sensor inputs S_i. Such an approach to generating the look-up table may be able to incorporate recent advances in applications of control theory to wall shear stress reduction (*e.g.*, Kim 2001).

Figure 3.1.   Schematic indicating fundamental architecture for microactuator arrays based on a unit-cell structure developed in this study. Each unit cell is composed of small arrays of sensors and actuators, with local unit-cell control processing capability resident in each cell, as indicated in Fig. 3.2. Tiles containing large numbers of such units cells can be produced using microfabrication techniques.
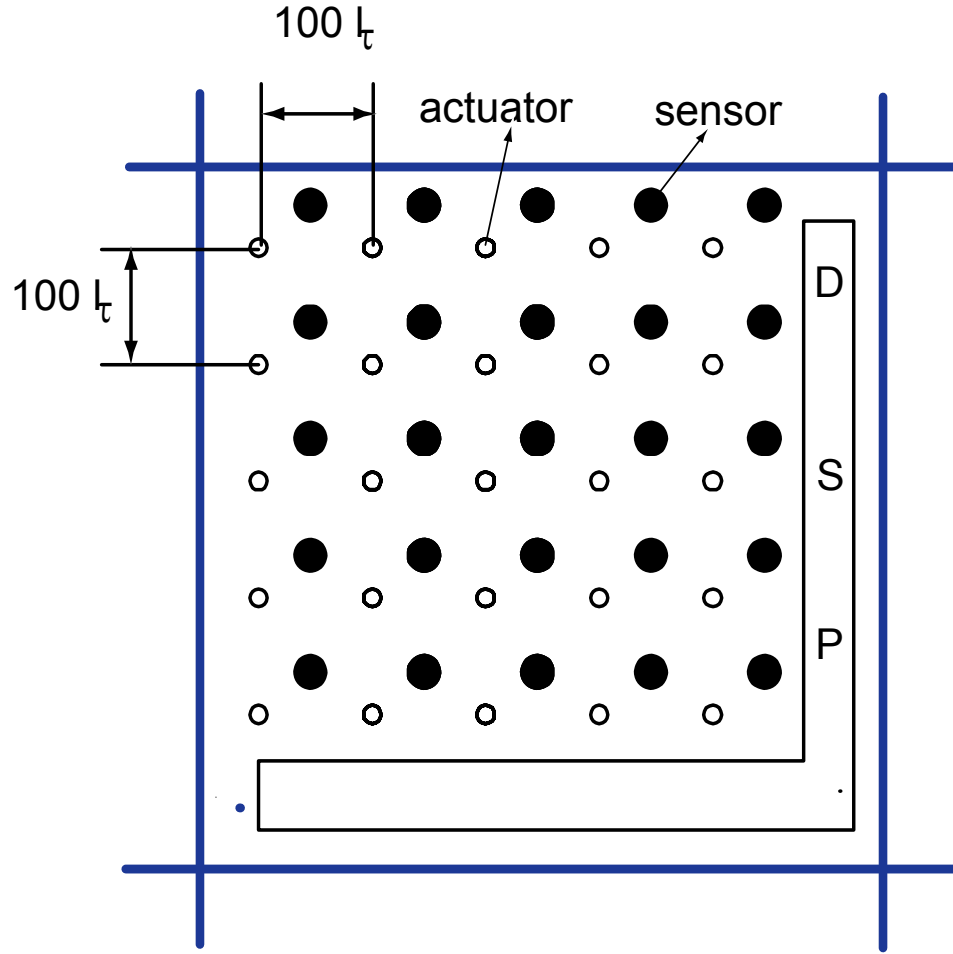
Figure 3.2.   Basic unit-cell architecture, showing collocated $n \times n$ arrays of typically $4 \leq n \leq 6$ microscale sensors and actuators spaced 100 viscous wall units l_τ apart, with space for unit-cell processing and with common voltage bus lines separating adjacent unit cells. The relatively small number of sensors and actuators in each unit cell permits simple look-up table approaches for the unit-cell processing.
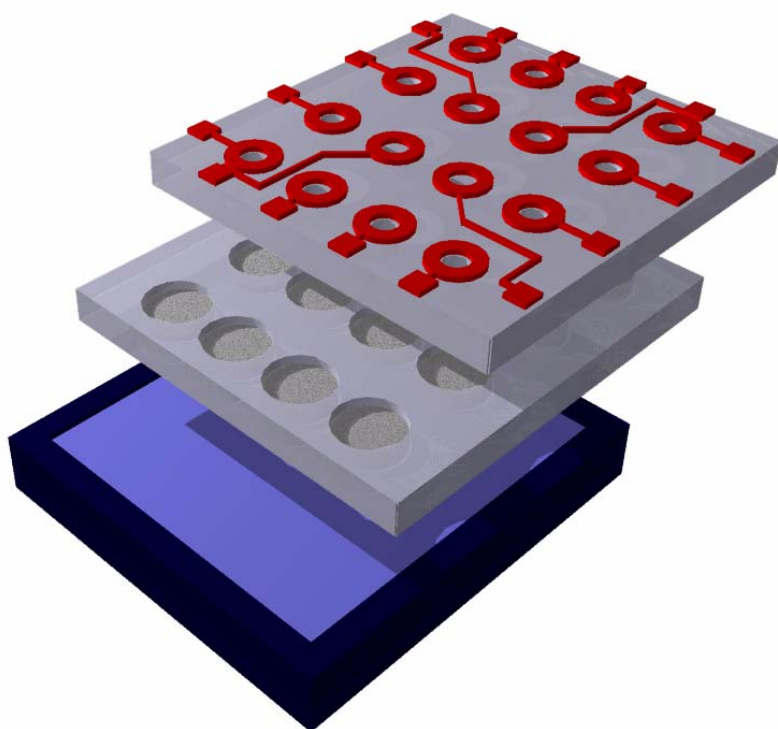
Figure 3.3.   Fundamental three-layer design of electrokinetic microactuator arrays at the unit-cell level, showing a top layer containing individual actuator nozzles, electrodes and leadouts, a center layer containing the electrokinetic driver channels in which electrolyte pumping occurs in response to an applied electric field, and an electrolyte reservoir and common electrode in the bottom layer.
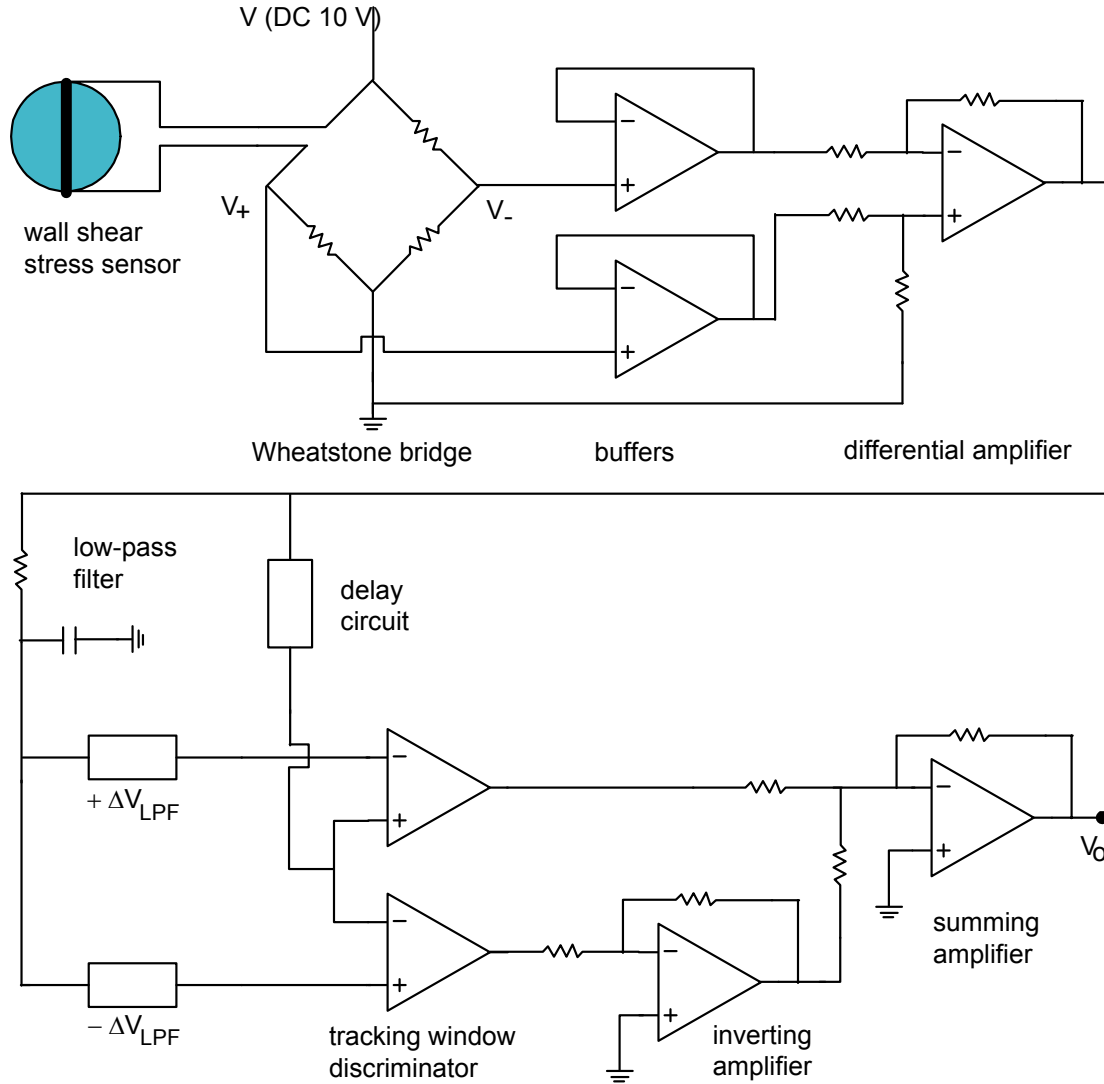
Figure 3.4. Simple circuit design that generates the sensor state S_i for each of the wall shear stress sensors within the unit cell as described in §3.2.2. Sensors outputs are thresholded relative to a running average to eliminate the need for individual sensor calibrations, sensitivity to sensor drift, sensitivity to location on the vehicle surface, and effects of changes in vehicle speed or attitude.
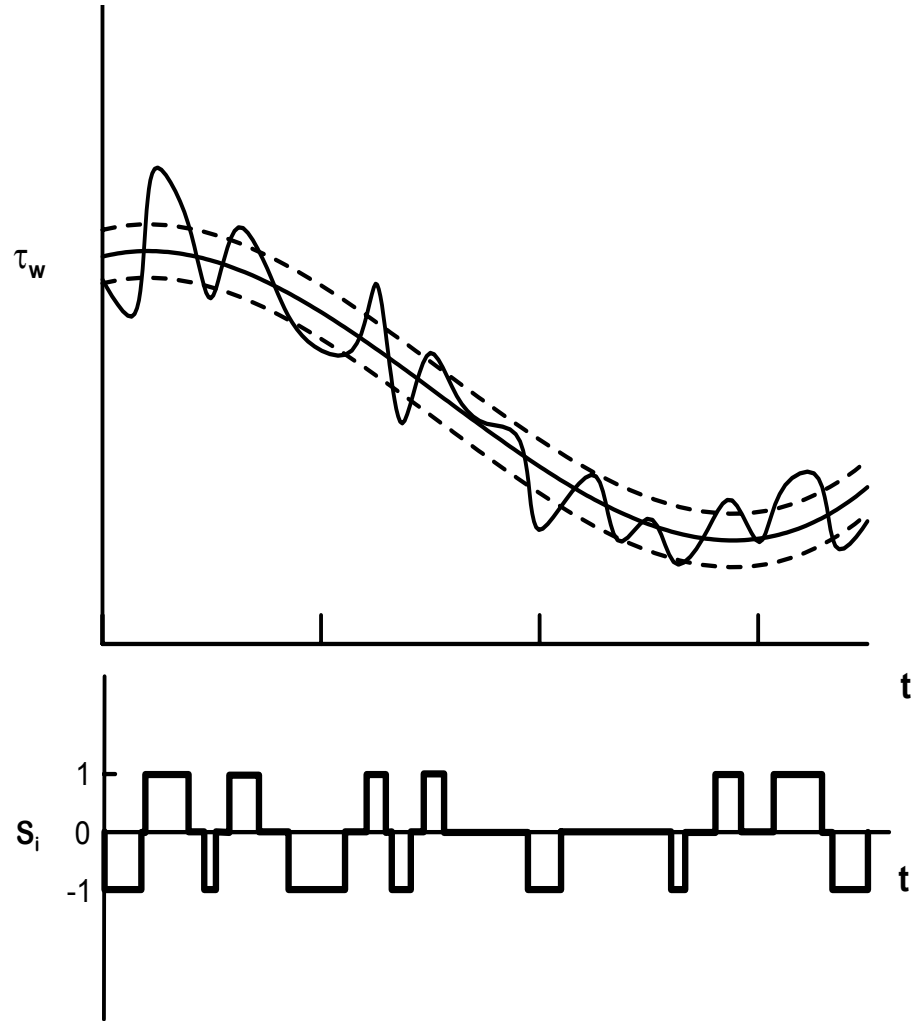
Figure 3.5.   Schematic indicating thresholding of wall shear stress measurements relative to a running average *(top)* to produce sensor states S_i *(bottom)*, which in turn imply unmodulated actuator states A_i via the PLA look-up-table. When $A_i = +1$ the corresponding actuator produces positive volume displacement, negative displacement when $A_i = -1$, and no displacement when $A_i = 0$.
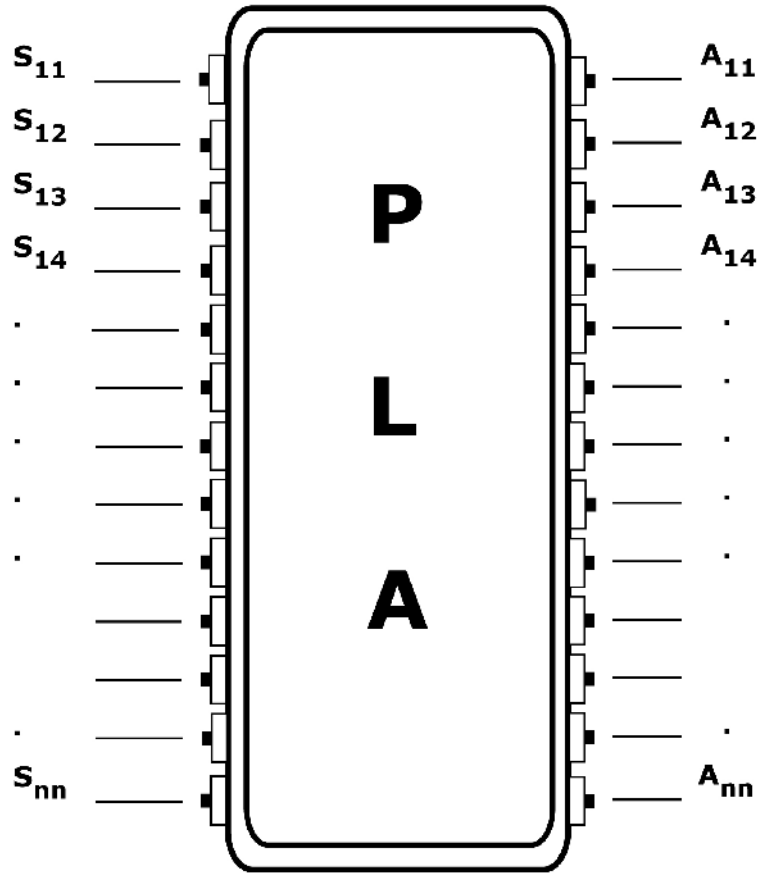
Figure 3.6.   Representation of a unit-cell programmable logic array (PLA) showing sensor state vector $\{S_i\}$ input to PLA formed from all individual sensor states within the unit cell, and the actuator state vector $\{A_i\}$ output from PLA that determines each of the individual electrokinetic microactuator states. The relatively small vector sizes permitted by the unit cell architecture may allow a simple look-up table in the PLA.
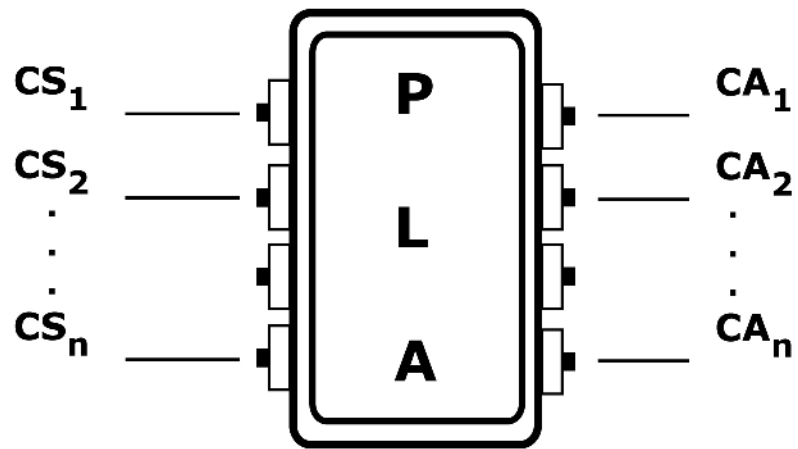
Figure 3.7.   Reduction in sensor and actuator state vectors described in §3.3 due to overall one-dimensional structure of sublayer vortical structures, with correspondingly reduced requirements for the unit-cell programmable logic array (PLA).

$$\begin{bmatrix} A_1 \\ A_2 \\ A_3 \\ A_4 \end{bmatrix} = \begin{bmatrix} R_{11} & R_{12} & R_{13} & R_{14} \\ R_{21} & R_{22} & R_{23} & R_{24} \\ R_{31} & R_{32} & R_{33} & R_{34} \\ R_{41} & R_{42} & R_{43} & R_{44} \end{bmatrix} \begin{bmatrix} S_1 \\ S_2 \\ S_3 \\ S_4 \end{bmatrix}$$

Actuator   Response   Sensor
Vector   Matrix   Vector
$\{A_i\}$ R_{ij} $\{S_j\}$
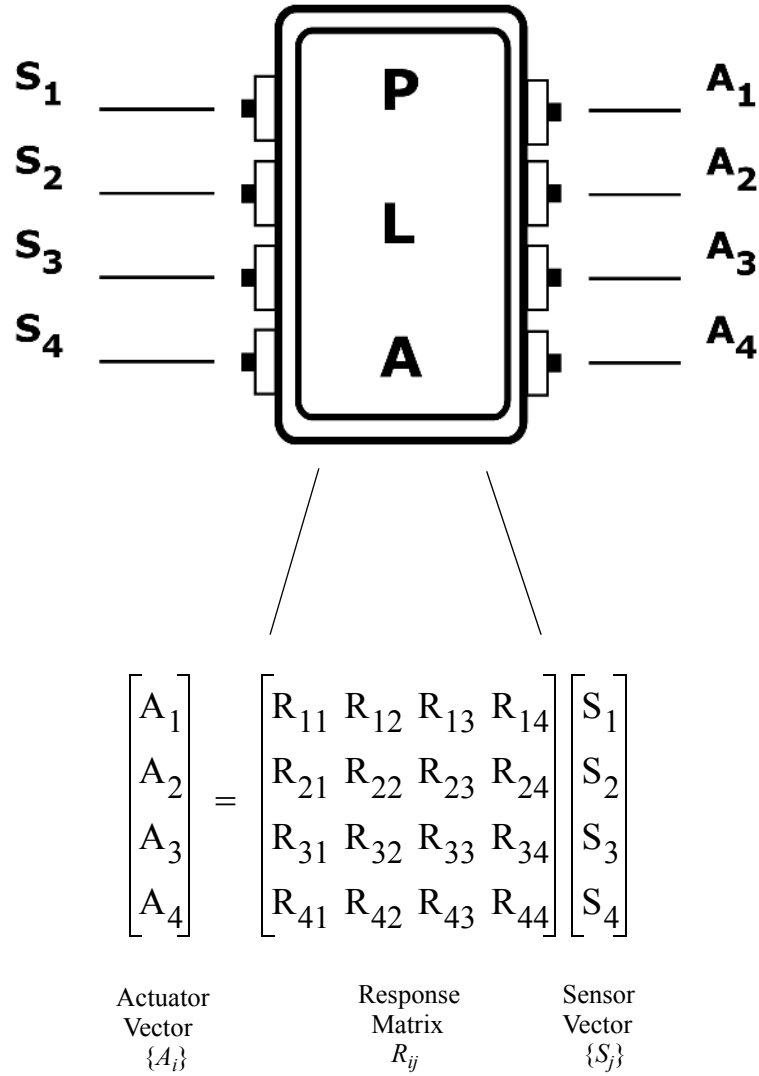
Figure 3.8.   Minimal programmable logic array (PLA) content in each unit cell, giving actuator state vector $\{A_i\}$ as a linear function of the sensor state vector $\{S_i\}$ for a restricted subset of possible sensor states. Several such response matrices R_{ij}, each applicable for such a restricted set of sensor states S_i, would be contained within the PLA on each unit cell.

CHAPTER 4

ELECTROKINETIC THEORY

4.1 Electrokinetic Flow

The electrokinetic microactuators that are the subject of this work function on the basis of the electrokinetic effect (*e.g.*, Potter 1961; Burgreen & Nakache 1964), first noted by Reuss (1809). While this effect inherently operates at the microscale, it is widely used in a variety of practical devices and processes to produce macroscale effects. Examples include transport processes in emulsions and suspensions, as well as soil remediation processes, to name just a few. The present study is the first attempt to exploit its potential advantages as the basis for a new class of microscale actuators suitable for active sublayer control in turbulent boundary layers at full-scale vehicle operating conditions.

The electrokinetic effect occurs at the interface between two phases, typically a solid and a liquid, that are in direct contact with one another. In the case of the present electrokinetic microactuators, this interface is between a solid polymer and an electrolytic fluid. An ionic "double-layer" forms naturally at such an interface, as discussed in §4.2. Four different types of electrokinetic phenomena can occur as a result of interaction between this ionic double-layer and an electric field. These can be classified on the basis of whether it is the *liquid* phase or the *solid* phase that moves, and whether the electric field is *imposed* to create the motion or is a *result* of relative motion induced between the two phases. The electrokinetic phenomena that result from the four possible combinations are termed electroosmosis, electrophoresis, streaming potential, and sedimentation potential. The latter two are produced by an imposed motion of, respectively, the liquid or the solid, each of which results in a current due to the flow of ions in the double-layer, and thereby produces

an associated electric potential. The former two are produced by an imposed electric field, which produces an electromagnetic force on the ions in the double-layer and thereby induces motion on them. The ions then collisionally transfer momentum to induce motion, respectively, in the bulk liquid or on the solid particles.

The term *electroosmosis* is used for the case where an imposed electric field induces a flow in the liquid phase, and it is this manifestation of the electrokinetic phenomenon that drives the present electrokinetic microactuators. Such an electroosmotic flow, shown schematically in Fig. 4.1, results when an electric field is applied to a liquid electrolyte in contact with a charged solid surface, producing a displacement of the liquid with respect to the stationary surface. In practice, this stationary surface might typically be a thin capillary tube or a fine porous matrix, with the electrolyte filling the open volume. In either case, it is the presence of the ionic double-layer and its interaction with the imposed electric field that is central to the electrokinetic flow principle on which these microactuators are based, and thus to the operating performance which these microactuator arrays can achieve.

For this reason, §4.2 reviews the physical processes involved in the double-layer formation, including how the solid surface acquires its charge and how this interface charge forms the double-layer and the associated zeta potential. Following this, §4.3 reviews the theoretical basis of steady electrokinetic pumping that can be accomplished by subjecting this double-layer to a *steady* electric field. Finally, §4.4 then develops simple hydrodynamic models, developed as part of this study, which describe the frequency response of electrokinetic pumping by an *unsteady* applied electric field, in order to determine the impulse response of electrokinetic microactuators.

4.2 Double-Layer Formation

There are four fundamental physico-chemical mechanisms by which a solid surface can acquire an "interface charge" through contact with a liquid electrolyte; these have been

widely studied (*e.g.*, Hunter 1981; Crow 1988; Bockris & Khan 1993) and form the basis of the ionic double-layer origin. This interface charge can arise from *(i)* the adsorption of ions, *(ii)* the loss or gain of lattice ions, *(iii)* the absorption of ionic surfactants, or *(iv)* the ionization of surface acid or basic groups. Perhaps the most important for biological and polymer systems is the latter, which occurs as a result of chemical interactions between surface acid or basic groups in contact with the electrolyte solution. This is the case, for example, in proteins with the ionization of carboxyl and amino groups to respectively produce COO^- and NH_3^+ ions, or in mineral substances such as clay with the ionization of silanol (Si-OH) groups, as shown in Fig. 4.2. In this study, first-generation electrokinetic actuators were fabricated from silica capillaries having 100 μm inner diameter, and filled with 1-5 μm diameter glass beads to form a porous solid structure, as shown schematically in Fig. 4.3*a*. The surfaces of the glass beads were initially covered with Si-OH groups, which ionizes when brought in direct contact with a liquid electrolyte to produce SiO^- surface ions when the electrolyte pH >2, or to produce $SiOH_2^+$ surface ions when the electrolyte pH < 2. The current-generation electrokinetic microactuators that have resulted from this study work on a similar principle, but are fabricated from a porous polymer matrix structure (Peters *et al* 1998*a,b*) with average pore size around 1 μm, shown schematically in Fig. 4.3*b*. In this case the polymer is doped with sulfonic acid groups, which have the general formula $R\text{-}SO_4H$, where R can represent any of a number of different organic structures. The ionization of this acid that results from contact with an electrolyte, shown in Fig. 4.2*a*, produces surface sulfate ions with the general formula $R\text{-}SO_4^-$.

Ionization of the surface acid or base groups leaves an excess negative charge on the surface and an excess positive charge in the liquid. The negative charges on the wall are balanced by positive counter-ions in the electrolyte buffer solution, with the counter-ion concentration decreasing exponentially with increasing distance from the wall in accordance with a Boltzman distribution, as will be seen in §4.3. At the same time the negative co-ion concentration decreases as the wall is approached, since these ions in the electrolyte buffer are being repelled by the negative wall charge. Sufficiently far from the wall, the counter-ion and co-ion concentrations are the same. The interaction between the wall charges and the oppositely-charged counter-ions in the electrolyte buffer gives rise to a

so-called "double-layer" structure near the wall, shown schematically in Fig. 4.4.

This double-layer structure of the counter-ions in the vicinity of the wall is comprised of an immobile "inner" layer and a diffuse "outer" layer. The inner layer results from counter-ions that are electrostatically held by the oppositely-signed surface charge. These are solvated ions – ions surrounded by a layer of solvent (in most cases water molecules) – that are in very close proximity to the charged surface and remain immobile with respect to it, forming what is sometimes called a "Stern" layer. The strong electrostatic attraction between the wall charges and the counter-ions in this inner (Stern) layer prevents these ions from moving under the influence of an applied electric field. However, further away from the wall the electrostatic attraction of counter-ions by the wall charge is no longer sufficient to overcome the electrostatic repulsion between these same-signed counter-ions. As a result, the remaining counter-ions required to balance the wall charge will be kept in relatively close proximity to the wall due to their electrostatic attraction by the wall charge, but will form a relatively diffuse layer due to their mutual electrostatic repulsion. The counter-ions within this diffuse outer layer (sometimes referred to as the "Gouy" layer) are free to drift under the influence of an applied electric field, and it is their motion in the presence of an applied field that forms the basis of the electrokinetically induced flow. For the charge states considered here, the counter-ions will migrate toward the cathode. The boundary between these inner and outer layers is often referred to as the shear plane, since this "slip plane" separates the immobile inner-layer ions and the diffuse outer-layer ions.

The detailed structure of the charge distribution within the outer layer can be obtained from fundamental analyses of the physical processes involved; this will be examined in §4.3. The resulting separation of charges between the wall and double-layer gives rise to a decreasing electric potential with increasing distance from the wall. The potential difference between the shear plane and the wall is termed the "zeta potential", and provides a measure of the total driving potential (per unit applied field strength) available for electrokinetic pumping. In general, solid-liquid pairs that produce larger zeta potentials are more effective for electrokinetic pumping.

4.3 Electrokinetic Pumping

The Navier-Stokes equation can be used to obtain the detailed outer-layer structure and the resulting electrokinetic pumping that it induces under the influence of an applied electric field (*e.g.*, Burgreen & Nakache 1964; Rice & Whitehead 1965). In its general form for constant viscosity, this equation can be written as

$$\rho\frac{DV}{Dt} = -\nabla p + \mu\nabla^2 V - F. \tag{4.1}$$

Under steady-state conditions, for the axisymmetric flow that results in an infinitely long capillary or pore channel this can be written in polar coordinates as

$$\mu\frac{1}{r}\frac{d}{dr}\left(r\frac{dv_z}{dr}\right) = -P_z - F_z \tag{4.2}$$

where P_z is the pressure gradient $-dp/dz$ and F_z represents the electric body force generated by an axial electric field E_z on the net charge density $\rho(r)$ in the double-layer. This force can be written as

$$F_z = E_z\rho(r). \tag{4.3}$$

The charge density $\rho(r)$ at a distance r from the surface can be written using the Boltzman distribution, which gives the number n_i of ions of a particular kind i which are at a potential ψ above that of a solution containing uniformly distributed ions, namely

$$\rho(r) = \sum_i n_i e z_i = e\sum_i \hat{n}_i z_i e^{-ez_i\psi/(kT)}. \tag{4.4}$$

where $n_i = \hat{n}_i e^{-ez_i\psi/kT}$. For a simple electrolyte which ionizes into equally charged ions of valence z, this charge density becomes

$$\rho(r) = \hat{n}ez(e^{-ez\psi/kT} - e^{ez\psi/kT}), \tag{4.5}$$

which can be simplified to

$$\rho(r) = -2\hat{n}ez\sinh\frac{e\psi}{kT}. \tag{4.6}$$

This can be further simplified for small values of $e\Psi/kT$ using the approximation

$$\sinh\left(\frac{e\psi}{kT}\right) \approx \frac{e\psi}{kT}. \tag{4.7}$$

This approximation is in good agreement with experimental results up to values of

$\psi \approx 50 mV$ as discussed by Overbeek & Wiersema (1967), Levine *et al* (1974), and Bock-ris & Khan (1993).

Using (4.7), (4.6) can be written for an electrolyte with monovalent ions as

$$\rho(r) = -2\hat{n}e^2\psi/(kT).$$
(4.8)

Equation (4.8) can be solved with the aid of the Poisson equation, which relates the potential ψ *(r)* to the charge density $\rho(r)$ as

$$\frac{1}{r}\frac{d}{dr}\left(r\frac{d\psi}{dr}\right) = \frac{\rho(r)}{\varepsilon},$$
(4.9)

where $\varepsilon = \varepsilon_r\varepsilon_o$. Here ε_o is the permittivity of vacuum and ε_r is the relative permittivity of the electrolyte. Substituting (4.8) into (4.9) gives the Poisson-Boltzman equation in cylindrical coordinates as

$$\frac{1}{r}\frac{d}{dr}\left(r\frac{d\psi}{dr}\right) = \kappa^2\psi,$$
(4.10)

where $\kappa = (\varepsilon kT/(2e^2\hat{n}))^{-1/2}$ is the double-layer thickness. In kinetic theory, κ is known as the Debye length. Typical values of the Debye length for aqueous electrolyte solutions can range from 0.5 to 1000 nanometers (van Oss 1994) and decreases with increasing ion concentration $\hat{n}$ in the electrolyte as $\kappa \sim \hat{n}^{-1/2}$, suggesting that the double-layer thickness can be made be exceedingly small.

The solution to (4.10) is

$$\psi = \zeta\frac{I_o(\kappa r)}{I_o(\kappa w)},$$
(4.11)

where w is the radius of the capillary, $\psi = \zeta$ at $r = w$ and I_o is the zero-order modified Bessel function of the first kind. Substitution of (4.11) into (4.8) then gives

$$\rho(r) = -\varepsilon\kappa^2\zeta\frac{I_o(\kappa r)}{I_o(\kappa w)}.$$
(4.12)

with this known charge density, the equation of motion in (4.2) can then be rewritten as

$$\mu\frac{1}{r}\frac{d}{dr}\left(r\frac{dv_z}{dr}\right) = -P_z - E_z\left(\varepsilon\kappa^2\zeta\frac{I_o(\kappa r)}{I_o(\kappa w)}\right).$$
(4.13)

For the present electrokinetic microactuators, no pressure gradient is applied, and the flow instead results entirely from the applied electric field E_z. Solving (4.13) under these conditions, the velocity v_z is obtained as

$$v_z(r) = -\frac{\varepsilon\zeta}{\mu}E_z\left(1 - \frac{I_o(\kappa r)}{I_o(\kappa w)}\right).$$ (4.14)

Except in the double-layer region $r \approx w$, (4.14) can be simplified to

$$v_z(r) = -\frac{\varepsilon\zeta}{\mu}E_z.$$ (4.15)

The ionic mobility Ω is defined from (4.15) as

$$\Omega \equiv \frac{\varepsilon\zeta}{\mu}.$$ (4.16)

The volume flow rate Q can be obtained by integrating (4.14) over the cross-sectional area of the capillary or pore channel to give

$$Q = \pi w^2 \Omega E_z\left(1 - \frac{I_o(\kappa r)}{I_o(\kappa w)}\right),$$ (4.17)

which simplifies for capillaries with radius much larger than the double-layer thickness to

$$Q = \pi w^2 \Omega E_z.$$ (4.18)

The pressure achieved in a plugged capillary can be obtained by first solving (4.13) as

$$v_z(r) = \frac{P_z}{4\mu}(w^2 - r^2) - \frac{\varepsilon\zeta}{\mu}E_z\left(1 - \frac{I_o(\kappa r)}{I_o(\kappa w)}\right),$$ (4.19)

and then integrating to obtain the flow rate Q similarly to (4.17). For such a plugged capillary, the net flow rate is zero. Using this condition, the solution can be obtained for the pressure gradient as

$$P_z = 8\mu\Omega\left(1 - \frac{I_o(\kappa r)}{I_o(\kappa w)}\right)\frac{E_z}{w^2}.$$ (4.20)

Again, for $\kappa w > 1$, (4.20) can be simplified to

$$P_z = 8\mu\Omega\frac{E_z}{w^2},$$ (4.21)

and hence the force F achieved by the actuator channel when plugged is

$$F = 8\pi\mu\Omega E_z L,$$ (4.22)

53

where L is the length of the channel.

These scalings are for a single channel. For a channel of radius R consisting of $(R/w)^2$ individual pores each of radius w, the flow rate in (4.22) becomes

$$Q = \pi R^2 \Omega E_z \qquad (4.23)$$

with the resulting flow speed $U = Q/\pi R^2$, and the force F achieved in a plugged actuator becomes

$$F = 8\pi\mu\Omega\left(\frac{R}{w}\right)^2 E_z L. \qquad (4.24)$$

Benchtop testing conducted with electrokinetic microactuators formed from capillaries packed with glass beads of size w and operated under steady applied fields (§5.1) verified that the pressure increased linearly with applied voltage ΔV and varied with bead diameter (and hence effective channel radius) as w^{-2}, as suggested by (4.21). The volume flow rate Q also was observed to increase linearly with applied voltage and the ionic mobility Ω as in (4.23), verifying the applicability of these scalings to the present electrokinetic micro-actuators.

Note in (4.23) that the flow rate achieved is independent of the pore radius w, but the force in (4.24) increases as the pores are made smaller. This suggests that by fabricating electrokinetic channels with sufficiently small pores, it may be possible to achieve flow rates adequate to meet the requirements in §2.3 while at the same time achieving sufficiently high pressures in any plugged actuators to allow these to unplug themselves. Moreover, as will be seen in the following section, such electrokinetic actuators fabricated at the microscale can have extremely high frequency response owing to the small time scales required for collisional (diffusion) transport of the induced flow across the channel.

4.4 Hydrodynamic Models of Frequency Response

As noted in Fig. 2.5, practical microactuators for sublayer control must operate at frequen-

54

cies around 1 kHz for hydronautical applications, and at frequencies as high as 90 kHz for the most demanding aeronautical applications. For electrokinetic driver sections based on porous channels with extremely fine pores, the resulting pore Reynolds number Uw/ν will be very low, and thus inertial damping of the unsteady response should be negligible. Furthermore, the extremely short time scale on which the Coulomb force equilibrates with the ion drag suggests that, in the presence of a time-varying applied field, the frequency response of microactuators based on the electrokinetic principle will be very high. The ultimate frequency response limits of such unsteady electrokinetic microactuators have not been fundamentally examined in the literature, however assuming that capacitances are properly managed there are two distinctly different physical processes that can limit their performance. The first is frequency response limitations in the coupling between the electric field and the ion drift in the outer layer, however owing to the physics associated with this process it may be anticipated that this response limit will be considerably higher than the requirements in Fig. 2.5. The second limit is due to inertial damping by the flow within the electrokinetic driver matrix. In order to estimate the theoretical frequency response attainable with such electrokinetic microactuators, this section develops simple models based on the hydrodynamics of electrokinetically driven flow to assess the potential frequency response and the key parameters that set the response limit.

The response of the electrokinetic flow in a typical pore of radius w to an unsteady applied field can be approximated by simple hydrodynamic models in two closely related limits. One limit applies when the electrokinetic double-layer thickness is much smaller than the pore radius w, as is typically the case in practical applications. The motion induced in the double-layer by either an impulsively applied electric field, or by a sinusoidally oscillating applied field, is then equivalent, respectively, to Stokes' first or second problem for the flow induced by viscous diffusion above a moving wall. The "wall" in this case is the thin double-layer, shown schematically in Fig. 4.5, and viscosity acts to diffuse the induced motion within it throughout the pore. The solutions to both of Stokes' problems are completely classical, and thus attention here will be focused on their implications for the frequency response of electrokinetic flows. In both cases, the motion is confined to a "Stokes layer" with thickness $\delta \approx \sqrt{\nu t}$ adjacent to the wall within which vis-

cous diffusion is able to induce flow.

Stokes' second problem corresponds to the motion induced in the fluid by a sinusoidally oscillating wall, and is most directly associated with the concept of frequency response. This case applies to the motion induced in the bulk electrolyte outside the double-layer by a sinusoidally time-varying applied electric field, which produces a sinusoidal motion in the thin double-layer directly adjacent to the wall. The resulting velocity field in this case is self-similar, and given by

$$u(y, t) = U_{eq} e^{-\eta} \cos(\omega t - \eta),$$ (4.25)

where $\eta \equiv y / \sqrt{2\nu/\omega}$ is the wall-normal similarity coordinate.

Figures 4.6a,b respectively define the actual flow rate Q'_{AC} that results from such a sinusoidally-induced motion during each volumetric displacement "stroke" of the actuator, and the flow rate Q'_{DC} that would result during the same time by steady electrokinetic pumping. Inertial effects in the induced flow are negligible when "quasi-steady" performance is achieved, namely when $Q'_{AC}/Q'_{DC} = 1$. The flow rate Q'_{AC} for a circular channel or pore is

$$Q'_{AC} \equiv \int_{t_o}^{t_o + T/4} \int_0^w u(r, t) 2\pi r (dr) dt,$$ (4.26)

which can be approximated by

$$Q'_{AC} \approx \frac{T}{4} 2\pi w \delta U_{eq}^{AC},$$ (4.27)

where U_{eq}^{AC} is the average velocity in the Stokes' layer directly adjacent to the wall, and T is the period corresponding to each stroke of the actuator. Substituting for T and δ in (4.27) results in

$$Q'_{AC} \approx \frac{\pi^2}{\sqrt{2}} w \nu^{1/2} \omega^{-3/2} U_{eq}^{AC} Q.$$ (4.28)

An electrokinetic microactuator of radius R filled with a porous matrix with pore size w contains $N \approx (R/w)^2$ pores. From (4.31) the total flow rate Q'_{AC} produced by these N pores in the entire actuator becomes

56

$$Q'_{AC} \approx \frac{\pi^2}{\sqrt{2}}\frac{R^2}{w}\nu^{1/2}\omega^{-3/2}U_{eq}^{AC}.$$ (4.29)

When a single capillary or pore is driven by a steady (DC) field, as shown in Fig. 4.6b, then the resulting flow rate Q'_{DC} is

$$Q'_{DC} = \frac{T}{4}\pi w^2 U_{eq}^{DC}.$$ (4.30)

Similarly, for the entire actuator the total flow rate Q'_{DC} can be written as

$$Q'_{DC} = \frac{\pi^2}{2}R^2\omega^{-1}U_{eq}^{DC}.$$ (4.31)

The ratio of these two flow rates then allows the influence of inertial effects to be evaluated as

$$\frac{Q'_{AC}}{Q'_{DC}} \approx \sqrt{2}\frac{\nu^{1/2}}{w}\omega^{-1/2}\frac{U_{eq}^{AC}}{U_{eq}^{DC}}.$$ (4.32)

From (4.32) a cut-off frequency $\omega_c \equiv \nu/(2w^2)$ can be deduced below which the actuators will show "quasi-steady" performance, and above which a roll-off will occur as shown in Fig. 4.7. Assuming an aqueous electrolyte with kinematic viscosity comparable to that of water ($\nu \approx 10^{-6}$ m²/s), this indicates a cut-off frequency of the order of 500 kHz for 1 μm pores. For the porous polymer matrix used to fabricate the arrays in this study, the average pore size is roughly 1 μm, and this would suggest essentially loss-less frequency response up to around 500 kHz.

Stokes' first problem corresponds to the case where the wall is impulsively set into motion, as would apply for an impulsively applied electric field. The flow velocity with increasing distance from the wall and with increasing time again has a similarity solution in terms of the complementary error function. The resulting thickness δ of the layer adjacent to the wall within which viscous diffusion is able to induce flow is given by $\delta \approx \sqrt{\nu t}$. The volume flow rate, defined as

$$Q(t) \equiv \int_0^w u(r, t)2\pi r dr,$$ (4.33)

can be readily integrated to give

$$Q(t) \approx \pi w\sqrt{\nu t}U_{eq}$$ (4.34)

where U_{eq} is the equivalent wall velocity, in this case the velocity in the outer-layer induced by the electrokinetic flow. Defining the steady flow rate $Q_{DC} = \pi w^2 U_{eq}$ achieved by a steady (DC) applied voltage across the electrokinetic driver channel, the ratio of the unsteady to steady flow rates is given by

$$\frac{Q(t)}{Q_{DC}} \approx \frac{\sqrt{\nu t}}{w}. \tag{4.35}$$

Thus a characteristic startup time $\tau \equiv (w^2/\nu)$ can be deduced from (4.35). Assuming an aqueous electrolyte with kinematic viscosity comparable to that of water ($\nu \approx 10^{-6}$ m²/s) and $w \approx 1$ μm pore sizes, this would indicate that the unsteady flow rate in (4.35) will remain essentially the same as the steady flow rate up to applied frequencies of the order of 10^6 Hz. In other words, essentially no loss of electrokinetic pumping performance will be seen until the frequency of the applied electric field approaches 1 MHz. The volumetric pumping capabilities of electrokinetic microactuators operated at frequencies below this can be directly inferred from equivalent steady DC flow rates.

The second limit applies when the double-layer thickness is greater than the pore radius, in which case the electrolyte throughout the pore contains a largely uniform concentration of ions. The electrokinetic forcing then induces motion directly throughout the fluid, and thereby acts like a body force. The response is thus equivalent to the oscillatory flow induced in a pipe by a sinusoidally varying pressure gradient. This limit also has an exact solution (Sexl 1930) that can be used to assess frequency response limits applicable to that case. However, since the double-layer thicknesses in the present electrokinetic microactuators are much smaller than the pore sizes, this limiting case does not appear to be directly relevant. For actuators fabricated with much smaller pore sizes, or for liquid-solid pairs with much larger Debye thicknesses, this would be the appropriate limit for determining the frequency response.

These considerations indicate that it should be possible to meet the frequency response requirements for all of the vehicle types in Fig. 2.5 with electrokinetic microactuators based on aqueous electrolytes and porous matrix structures having typically 1 μm pore radii in the electrokinetic channels.
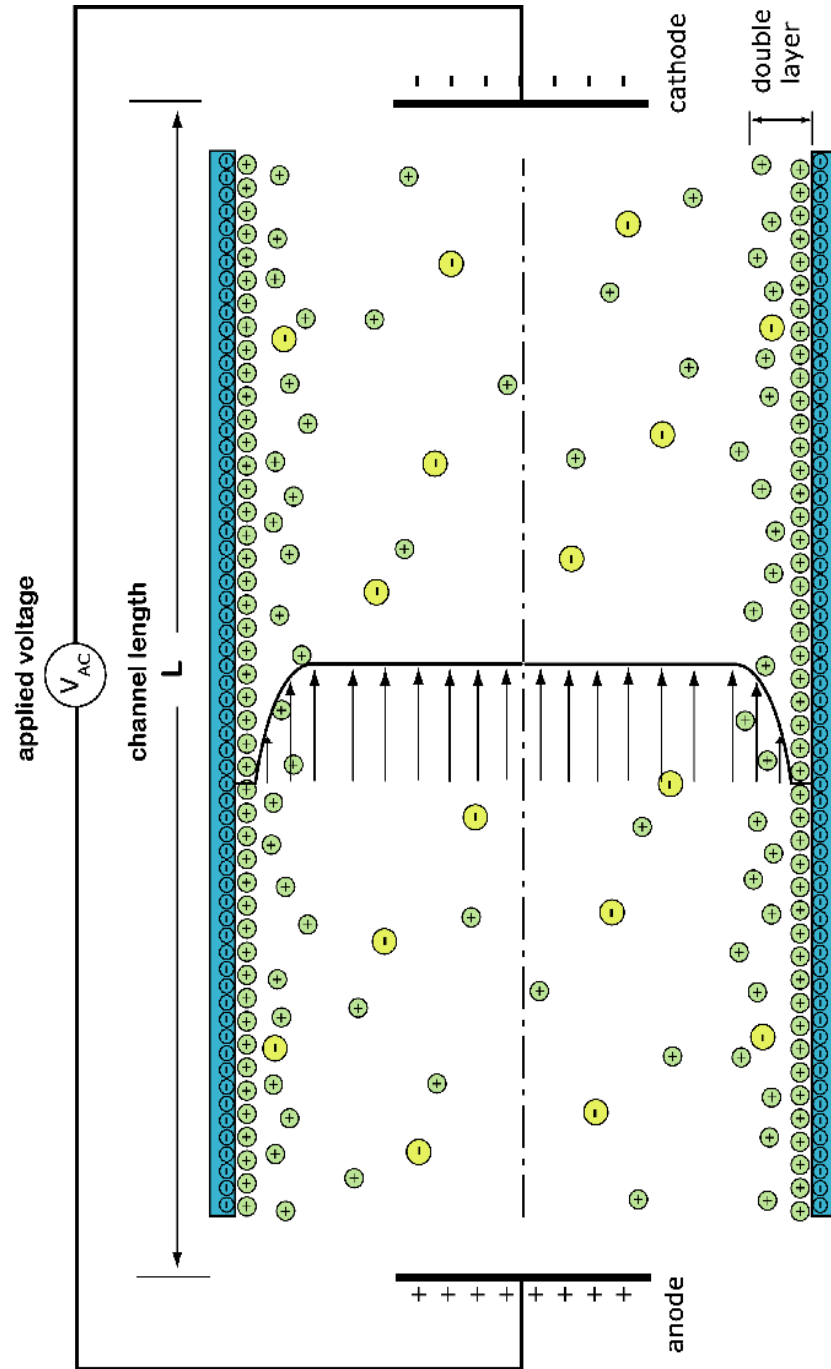
Figure 4.1.   Schematic showing electroosmotic flow induced by an applied electric field along a pore or capillary channel. The electric field induces drift in the mobile ions within the diffuse outer layer, which then collisionally transfer momentum to the electrolyte. Subsequent collisional transport (diffusion) transfers this motion throughout the channel.
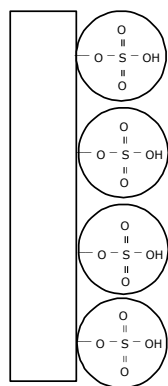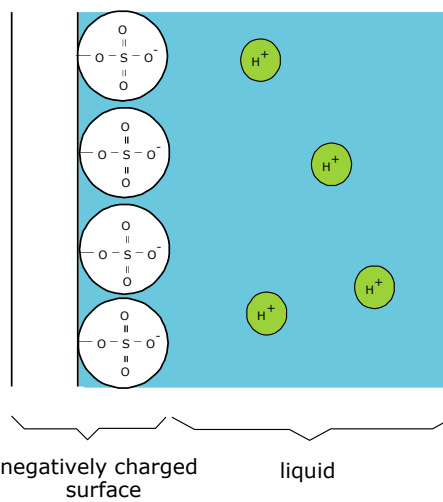
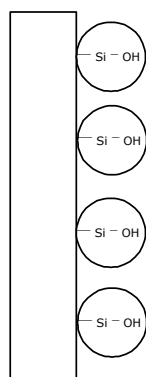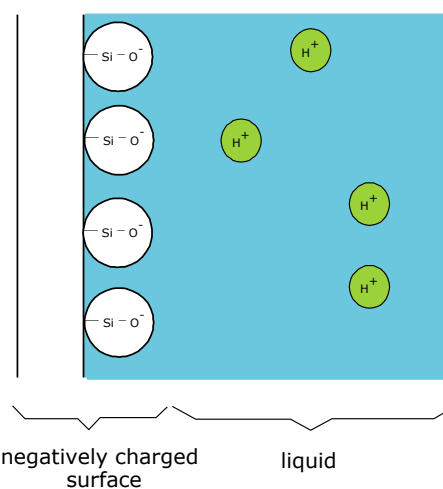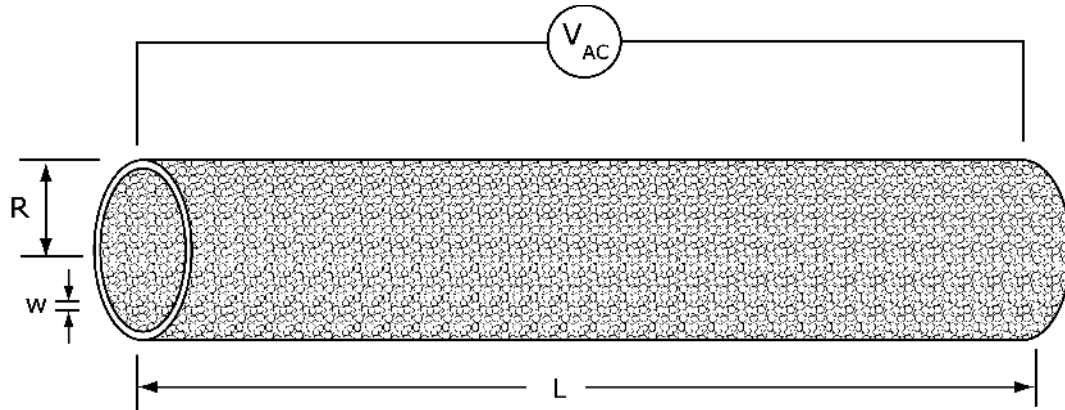Figure 4.2.   Schematics showing charge formation mechanism at a solid-liquid interface by ionization of *(a)* sulfonic acid groups, and *(b)* silanol groups.
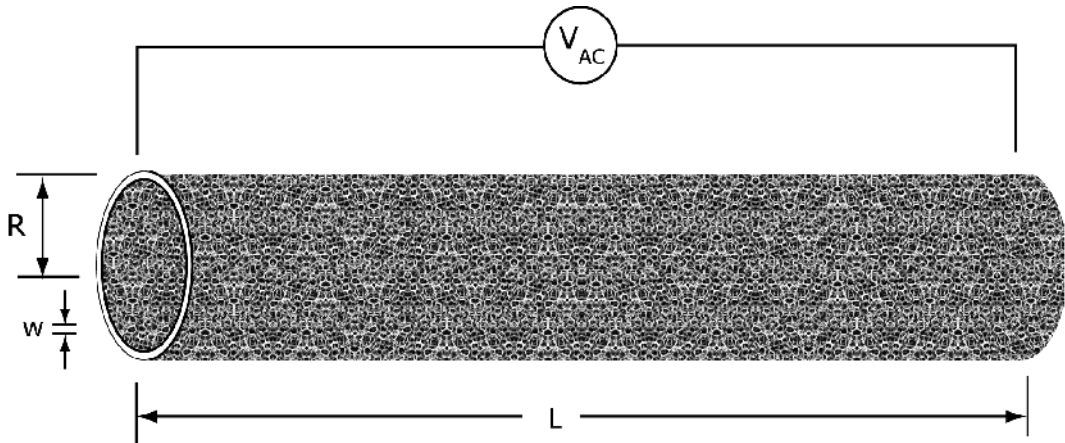
Figure 4.3. Schematic of typical solid matrix structures used to provide large double-layer surface areas, showing a typical electrokinetic driver channel filled with *(a)* micron-scale spherical glass beads, and *(b)* a porous polymer with micron-scale pore sizes.
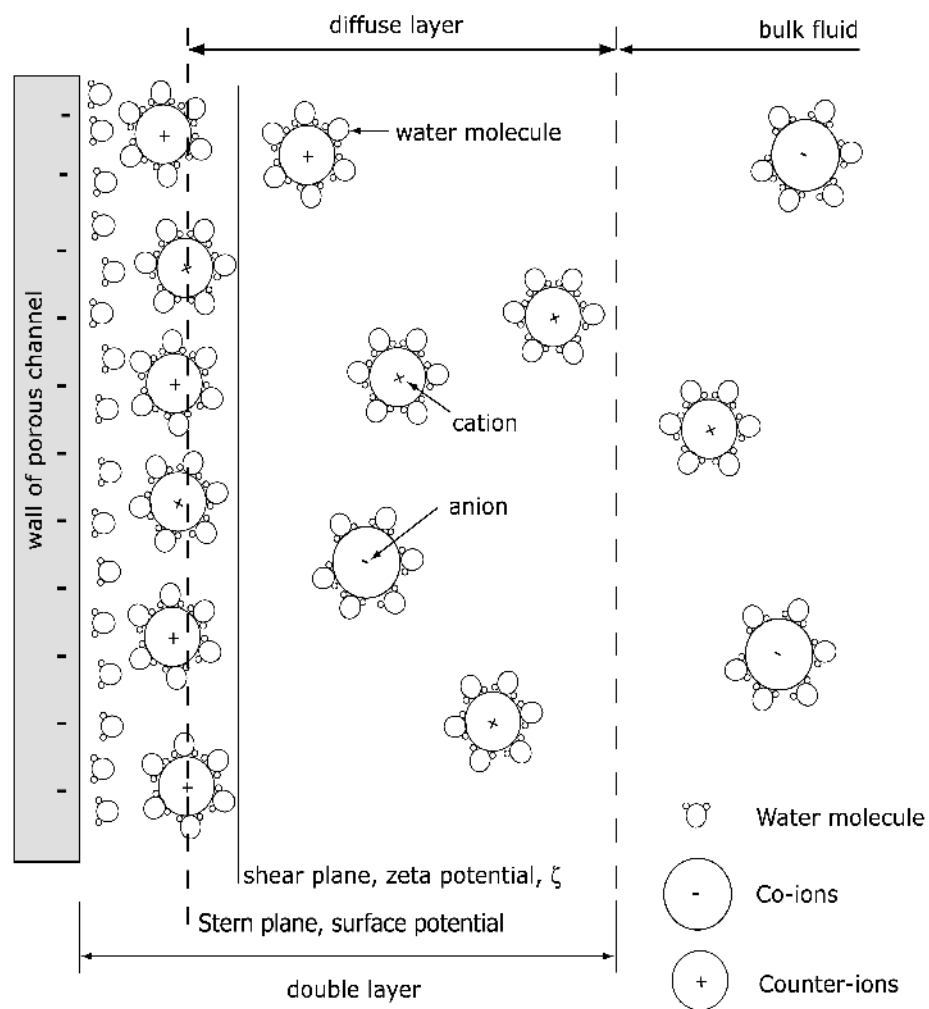
Figure 4.4. Schematic representation of the double-layer structure involved in electrokinetic flows, showing wall charges and immobile inner (Stern) layer, outer diffuse (Gouy) layer composed of hydrated counter-ions, and bulk electrolyte outside double-layer.
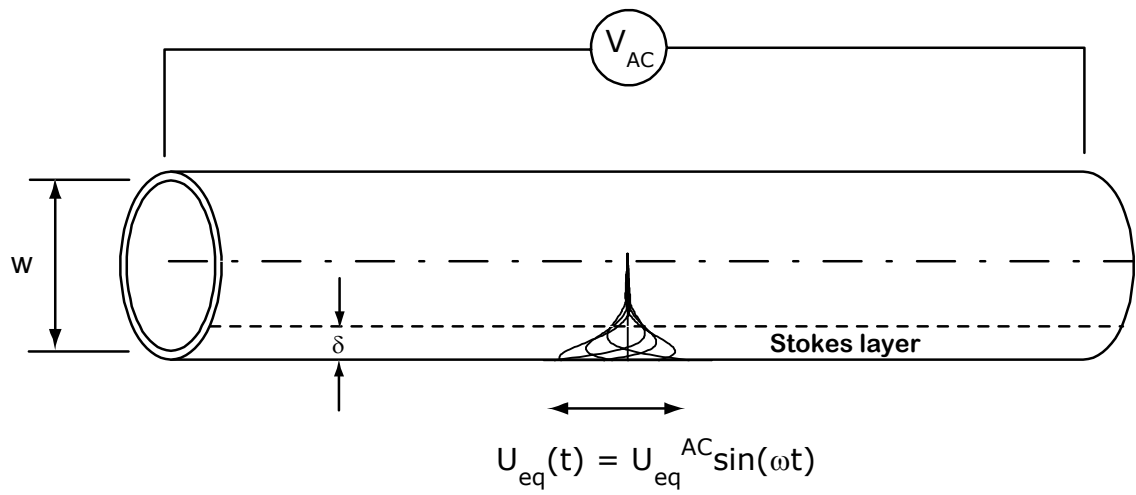
Figure 4.5.　　Schematic showing Stokes layer of thickness δ within which motion induced by a sinusoidally-applied electric field is confined. Oscillating "wall" in this case results from oscillating motion in the exceedingly thin double-layer immediately adjacent to the actual wall.

(a)

(b)
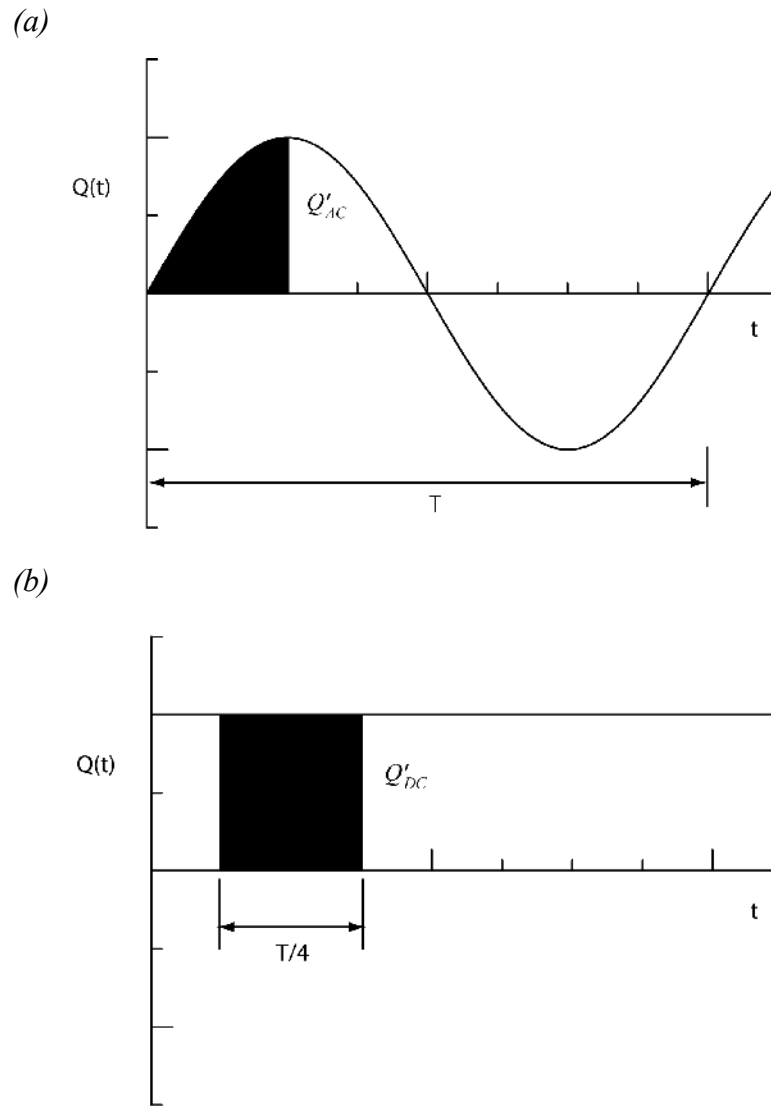
Figure 4.6.   Schematics defining *(a)* the volume Q'_{AC} displaced by electrokinetic pumping per actuator stroke time $T/4$ under a sinusoidally-applied electric field, and *(b)* the volume Q'_{DC} displaced during the same time $T/4$ under a steady applied electric field.
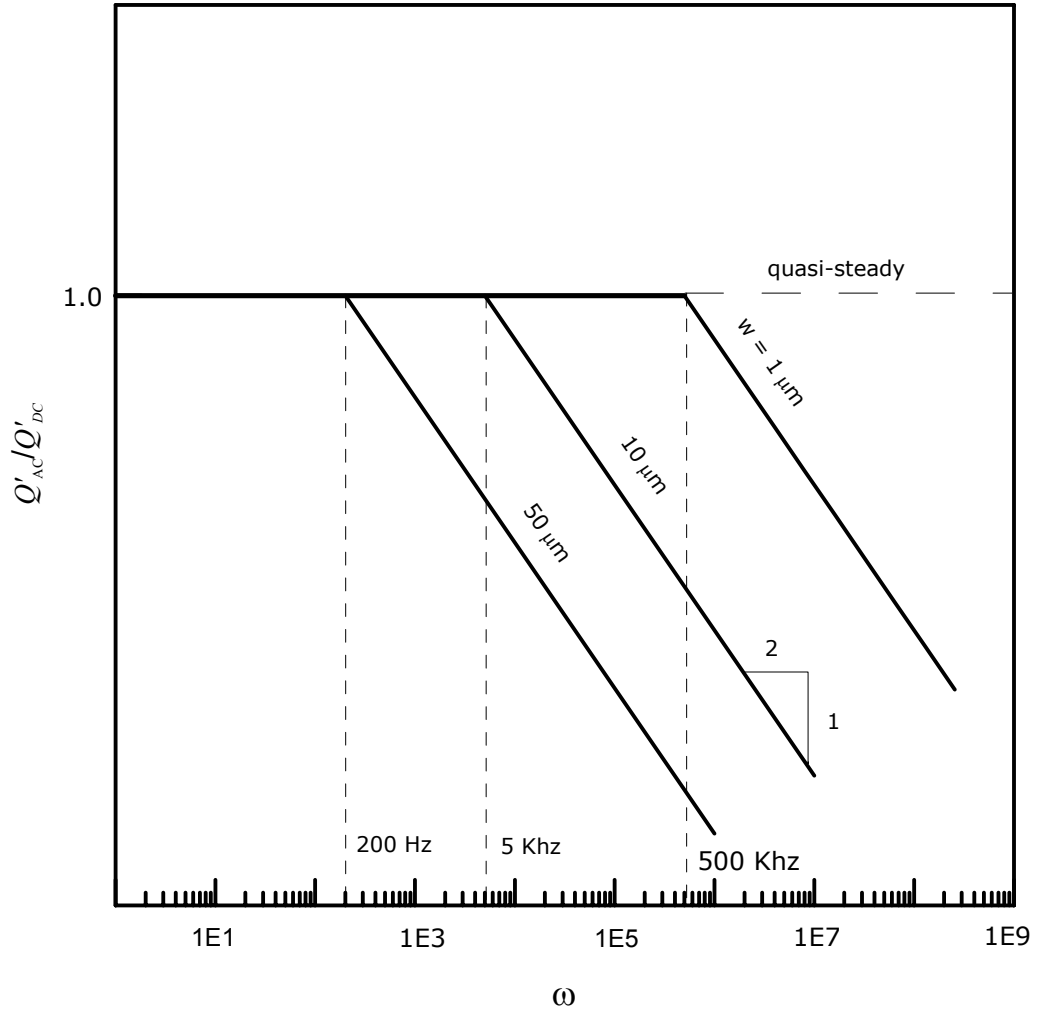
Figure 4.7. The ratio of Q'_{AC} to Q'_{DC}, defined in Fig. 4.6, from (4.32) for any sinusoidal component of frequency ω in an unsteady applied electric field. For $Q'_{AC}/Q'_{DC} \approx 1$, volumetric displacement achieved by electrokinetic pumping is in the quasi-steady limit with no losses due to inertia effects. Note that for 1 μm pore sizes as in §5, roll-off produced by inertial effects does not begin until frequencies above 500 kHz.

CHAPTER 5

ELECTROKINETIC MICROACTUATOR ARRAYS

5.1 Elementary Packed-Capillary Actuators

Initial experiments with electrokinetic flow as the fundamental basis for a new class of microactuator arrays were performed using simple packed capillaries to provide the double-layer surface that drives the flow. Testing of these actuators was done in collaboration with researchers in the Microtechnology Division at Sandia National Laboratories (*e.g.,* Dahm *et al* 1997) and continued in the initial phases of the present study. These initial "actuators" consisted of glass capillaries with 100 μm inner diameter, packed with glass beads of various diameters ranging from 0.5 μm to 5 μm, and filled with various aqueous electrolytes that provided differing zeta potentials. The glass beads created effective interstitial channels at submicron scales. The purpose of these experiments was to verify the applicability of the scaling results in §4 for such packed-capillary electrokinetic pumps at these scales under steady (DC) applied fields. The configuration used for these tests is shown schematically in Fig. 5.1.

Results verified the $Q \sim w^2 E_z$ scaling in (4.18) of the flow rate Q with pore size w (*i.e.,* bead diameter) and applied field strength E_z, and the $\Delta p \sim E_z L/w^2$ scaling (4.21), to pore sizes w at least as small as those produced by the 0.5 μm glass beads. In view of the exceedingly small Debye length scales associated with the double-layer thickness, which typically is in the range of 10-100 nm, the observed applicability of these scalings even at the smallest bead diameter (500 nm) is not entirely surprising. Nevertheless, the results confirmed that fabrication of electrokinetic microactuators with pore sizes down to at least these scales does not invalidate these fundamental performance scaling laws. This indi-

cates that electrokinetic microactuators based on porous matrix structures having average pore sizes of 1 μm, for which the entire range of pore sizes should be within the range applicable to the tests above using 0.5 μm beads, should allow large values of pressure rise Δp to be achieved in plugged actuators, while causing essentially no reduction in volume displacement rate Q for open actuators. All subsequent micro-electro-kinetic-actuator (MEKA) arrays developed in this study were based on electrokinetic flow produced in such micron-scale porous matrix structures.

5.2   Three Layer Design

The technology for creating porous polymer matrix structures, with 1 μm scale pore sizes, that can be suitably doped to provide electrokinetic flow (Peters *et al* 1998*a,b*) provided the basis for a fundamental three-layer design of electrokinetic microactuator arrays. This three-layer design, shown schematically in Fig. 5.2, uses a center layer containing individual electrokinetic driver channels formed in an appropriate substrate material, as discussed in the following sections, and filled with this porous polymer matrix structure. The porous matrix structure can be readily created throughout these individual channels by introducing the polymer in liquid form immediately after mixing its two principal constituents. Dopants are previously added to these principal polymer constituents as needed to provide the desired acidic or basic groups on the solid surface; the particular choice and concentration of dopants depends on the intended electrolyte and the desired zeta potential. Dissolved oxygen is removed from the liquid polymer mixture by repeated vacuum pumping before curing. Subsequent crosslinking of the polymer in the curing step, during which the liquid-filled center layer is placed between glass plates and "baked" at 40-60 °C for several hours, produces the porous structure within the center layer. Subtle changes in the polymer constituents and in the curing process can be used to control the resulting nominal pore size. The center layer in this three-layer design consists only of the individual electrokinetic driver channels filled with such porous polymer matrix structures, as shown in Fig. 5.3.

Once the curing process in the center layer is completed to produce the porous polymer, the resulting structure can be readily wetted with electrolyte by simple capillary wicking action. Continual contact with the electrolyte, and thereby continual wetting of the entire porous matrix throughout each individual actuator channel in the center layer, is provided by a common electrolyte reservoir in the bottom layer, as shown in Fig. 5.2. Since each unit cell acts as a zero-net-displacement entity, a fixed amount of electrolyte is maintained within each unit cell (or, alternatively, within each tile, as discussed in §3).

Note that no electrolyte is discharged from the unit cell; the electrokinetic flow induced in the electrolyte when an electric field is applied across any individual center-layer channel serves only to displace the working fluid (ambient fluid) from the top layer. This top layer, shown in Fig. 5.4, includes a nozzle directly above each actuator channel, as seen in Fig. 5.4*b*, in which working fluid is displaced by pumping of electrolyte in the center layer and issues through the top surface shown in Fig. 5.4*c*. In cases where the electrolyte must be separated from the working fluid, as would typically be the case for hydronautical applications, a thin layer of flexible membrane material would be sandwiched between the center and top layers. The top layer also contains a circular disk electrode for each actuator channel, with leadouts to connectors near the periphery of the unit cell. These are connected with either positive or negative polarity by the unit-cell control circuitry to the common voltage bus that runs between unit cells. This provides for a positive or negative electric field along each actuator channel between the top-layer electrode and the common electrode in the electrolyte reservoir in the bottom layer, producing positive or negative pumping of the electrolyte, and thereby producing positive or negative displacement of the working fluid from the top surface.

This basic three-layer design allows for dense arrays comprised a large numbers of such actuators to be fabricated in thin conformally-applicable tiles that accommodate the unit-cell system architecture described in §3, and that may in principle be easily applied to the surface of real vehicles. Elements of this basic three-layer design have been developed in successive generations of electrokinetic microactuator arrays described in the following sections. The most advanced of these arrays (MEKA-5) consists of a complete tile of

25,600 such individual electrokinetic microactuators, spaced on 325 µm centers and organized into a 40 × 40 array of unit cells, each with a 4 × 4 arrangement of actuators, and fabricated from this fundamental three-layer design.

5.3   MEKA-0 Microactuator Array

Based on the results from experiments with elementary packed channel actuators, an initial 3 × 3 array of electrokinetic microactuators, shown in Figs. 5.5*a-e*, was fabricated and used for performance testing. This array is somewhat smaller than the typical 5 × 5 unit-cell indicated in Fig. 3.2, however its purpose was principally for an initial exploration of the major challenges involved in unit cell fabrication, and for initial performance testing of unsteady (AC) electrokinetic flows. For added simplicity, this initial array was sized to the requirements of the UAV-scale application in Figs. 2.4 and 2.5, and thus consisted of individual microactuators with 1000 µm diameters and 2000 µm center-to-center spacings. The basic three-layer design in Fig 5.2 was used, with electrokinetic driver channels in the center layer and an electrolyte reservoir in the bottom layer, but with electrodes and leadouts formed on the top surface of the center layer.

The electrokinetic driver channels were in this case mechanically drilled into a 3 mm thick glass substrate. This was intended as a preliminary process used for this initial fabrication only, and not intended to represent a fabrication process suitable for eventual mass production. Note that the center-layer thickness determines the length-to-diameter ratio of the electrokinetic channels, which should be kept large enough ($L/D > 3$) to maintain reasonably straight electric field lines within the channel.

An individual ring electrode with a leadout to an electrical contact was formed on the top surface around the periphery of each of the microactuator channels using standard metallization and photoetching techniques, as can be seen in Figs. 5.5*c-e*. Due to chipping that occurred in the channel drilling process, as shown in Figs. 5.6*a-d*, the resulting edge quality was relatively poor. This caused some difficulties in maintaining electrode continuity

on the top surface of the center layer, however as Figs. 5.6*a,b* show the resulting ring elec-
trodes were still of acceptable quality. The bottom surface electrode is the common for all
the channels, and can be seen in Figs. 5.6*c,d.*

The individual center-layer electrokinetic driver channels in Figs. 5.6*a-d* were filled with
the porous polymer matrix structure described in §5.2. For the MEKA-1 array this used a
polymer consisting of several constituents, including butyl methacrylate with a solvent
and with a dopant to provide the zeta potential. The resulting porous polymer matrix
structure is visible as the white material in the channels in Figs. 5.5*c-e.* Filling of the
porous polymer with electrolyte was readily accomplished by simply applying a DC volt-
age across the top and bottom surface electrodes for each channel. The electrolyte quickly
wetted the entire channel and could be readily seen to flow from the top of each actuator.

DC performance testing was conducted using the apparatus shown in Fig. 5.7. This con-
sisted of an 8.5 mm in diameter by 2.5 mm in height electrolyte reservoir which had the
MEKA-1 array wafer located above it. The reservoir was filled with a 2mM sodium borate
buffer solution. When a steady voltage difference ΔV was applied across the electrodes,
the electrokinetic actuators steadily pumped the electrolyte into the graduated reservoir
shown in Fig. 5.7. The volume flow rate was measured over an extended time and the
results are shown in Fig. 5.8. Note that the total volume displaced increased linearly with
time, with the flow rate Q_{DC} being given by the slope of each set of symbols. The flow
rate achieved is seen to be proportional to the applied voltage, consistent with (4.23). For
these conditions, the porous polymer matrix material provided a volume flow rate Q_{DC} of
0.1 µL/min at an applied field strength E_{DC} of 33 V/mm. The ratio (Q_{DC}/E_{DC}) should thus
be independent of the field strength, and represents the fundamental characterization of
the electrokinetic pumping capability of the porous polymer matrix structure per unit
cross-sectional area of the actuator channels.

AC performance testing was also conducted to determine frequency response, by applying
a sinusoidally time-varying voltage difference. These measurements were performed with
a 1 mm diameter by 2 mm thick polymer electrokinetic pump, driven by a function gener-

ator into a Burr-Brown 3745 high-voltage op-amp. The applied voltage was varied from 5 V peak-to-peak up to 90 V peak-to-peak. In this case, the microactuator drove a small closed cavity containing an air bubble, and the time-varying pressure that developed in the cavity as the air bubble was compressed by the time-varying volume displacement achieved by the actuator was measured. A pressure transducer (Omega PX170-14GV) was used at low frequencies, and a microphone (Brüel & Kjær 4138 microphone with B&K 2618 preamp) at high frequencies. Results are shown in Fig. 5.9, giving the relative peak-to-peak variation in the signal from the transducer or microphone normalized by the manufacturer's response calibration. The f^{-1} scaling shown by the solid line is the theoretical result corresponding to loss-less AC performance; *i.e.*, the reduction in volume displacement per cycle resulting solely from the f^{-1} reduction in cycle period with frequency. The equivalent DC flow rate Q'_{DC} defined in Fig. 4.6*a* is seen in Fig. 5.9 to be essentially constant up to applied frequencies at least as high as 10 kHz. The origins of the roll-off above 10 kHz remain unclear, and may be due to an experimental limitation. The measured frequency at which this roll-off begins would be consistent with the onset of inertial damping in a porous matrix structure with 10 μm pores, based on the considerations in §4.4, whereas the nominal pore size in the electrokinetic driver channels is believed to be about 1 μm. However it is also possible that, while the pore size in the present matrix is nominally 1 μm, the largest pores may be as large as 10 μm, and that these determine the inertial damping limit for the actuator. Irrespective of these considerations, the 10 kHz frequency response demonstrated in these tests meets the demands for most of the vehicles in Figs. 2.4 and 2.5, and far exceeds the requirements for all the hydronautical applications.

5.4 MEKA-1 Microactuator Array

Based on the performance seen with the MEKA-0 microactuator array in §5.3, a MEKA-1 array was fabricated to *(i)* assess laser drilling of the electrokinetic channels as an alternative to mechanical drilling, and *(ii)* explore design issues associated with larger unit cells. This 10 × 10 actuator array was fabricated in glass, as was the case for the previous

MEKA-0 array, and again sized for a UAV-scale application. The individual electrokinetic microactuator channels were 2000 μm in diameter and located on 4 mm center-to-center spacings. The layout for this MEKA-1 array is shown in Fig. 5.10.

Drilling of the electrokinetic driver channels in glass was in this case done with a CO_2 laser by a commercial vendor. This fabrication process is amenable to eventual mass production. A comparison of the resulting edge quality produced by this laser drilling process in MEKA-1 with that of the mechanically drilled holes in MEKA-0 is shown in Figs. 5.11*a,b*. Edge quality achieved at this scale with laser drilling was excellent, and more than adequate for metallization and electrode etching.

The 10×10 unit-cell size of this MEKA-1 array is considerably larger than the 6×6 unit-cell anticipated in Fig. 3.2 for the proposed system architecture, yet Fig. 5.10 shows that the required electrode leadouts can be readily accommodated. Like the MEKA-0 array, the bottom surface electrode is common for all channels. The channels were filled with the same porous polymer matrix as for the MEKA-0 array. Figures 5.12*a,b* show the resulting filled microactuator channels, where the 1 μm-scale porous polymer matrix structure again appears white. Note that the individual electrokinetic microactuator driver channels in the center layer can be readily filled with the polymer using the procedure outlined in §5.2.

5.5 MEKA-2 Microactuator Array

In view of the excellent edge quality achieved by the laser drilling process in the UAV-scale MEKA-1 array, the process was applied to develop a hydronautical-scale MEKA-2 array. The principal purpose of this array was to test the suitability of the CO_2 laser drilling process in a glass substrate at much smaller scales. Accordingly, this array consisted of a simple 3×3 matrix of electrokinetic driver channels, each with 300 μm diameter and 2 mm length, on 500 μm center-to-center spacings.

The resulting hole quality is shown in Figs. 5.13*a,b*, where both the top (entry-side for the laser beam) and bottom surfaces are shown. As can be seen, the smaller channel diameters in this case produced much poorer results from laser drilling than was the case for the 2000 μm diameter channels in the MEKA-1 array. These difficulties were driven by fabrication glass substrate material. Since glass was not intended as a final substrate material, subsequent arrays examined fabrication with other substrate materials.

5.6   MEKA-3 Microactuator Array

The CO_2 laser drilling process was adapted for a MEKA-3 array by changing the substrate material from glass to acrylic, which is also readily amenable to laser drilling. The MEKA-3 array, shown in Figs. 5.14*a,b*, consisted of a 5×5 matrix of electrokinetic driver channels, each 300 μm in diameter and 2 mm long, and with 1000 μm center-to-center spacings.

Figure 5.15*a* shows close-up views of the hole quality resulting on the exit side from laser drilling process at this scale in acrylic. Edge quality was generally excellent and more than adequate for metallization. There was indication of melt flow around the periphery of the hole, with further indications of a circumferential instability in the melt flow, but these do not compromise the hole quality needed for metallization. Figure 5.15*b* shows much poorer edge quality on the entry side of the acrylic. The degradation appears due to cratering produced by ejection of molten material from the hole, as well as melt flow along the surface. However, since only one side of the center layer needs to be metallized, this can be done on the entry side, where edge quality is higher.

The results obtained from this MEKA-3 fabrication with laser drilling in acrylic indicate that it is possible to mass produce the center layer in thin plastic films by such a process. However, acrylic is unsuitable as a center-layer substrate material since it is incompatible with the organic solvents used in the porous polymer process. There are other plastics that can be readily laser drilled and that are compatible with these solvents. For this reason,

the center layer for MEKA-5 array in the following section was produced in mylar, which can be laser-drilled and is suitable for use with the porous polymer process.

5.7   MEKA-5 Hydronautical Array

5.7.1   MEKA-5 Array Design

The MEKA-5 actuator array, shown in Figs. 5.16, demonstrated fabrication of a full hydronautical-scale array of electrokinetic microactuators and their integration with a top-layer containing the basic unit-cell structure and all electrical leadouts required for actuation. The array was fabricated in a 7×7 cm^2 tile, containing 25,600 individual electrokinetic microactuators with 250 µm channel diameters arranged on 350 µm center-to-center spacings, as indicated in Figs. 2.4 and 2.6 for full-scale hydronautical vehicle applications. These individual electrokinetic microactuators were grouped into 1600 individual unit cells arranged in a 40×40 unit-cell pattern on each tile, with each unit-cell composed of a 4×4 array of microactuators. As indicated in Fig. 5.17, every fifth row and column of microactuators in the tile was skipped to provide room for the resident unit-cell processing electronics. The top layer, shown in Fig. 5.18*a*, was fabricated using conventional MEMS processing steps. The center layer in Fig. 5.18*b* was fabricated with the same porous polymer matrix material in thin flexible mylar substrate material suitable for conformal application on a vehicle surface. The following sections describe these center-layer and top-layer fabrication processes used to develop this full-scale MEKA-5 hydronautical array.

5.7.2   MEKA-5 Center Layer Fabrication

Figures 5.19*a,b* show the center layer of the three-layer MEKA-5 hydronautical array tile. Each of the 25,600 individual electrokinetic microactuators has a 250 µm microchannel diameter and 350 µm center-to-center spacing between microactuators within a unit cell.

The channels were fabricated in flexible mylar substrate material, having 250 μm thickness to permit a high electric field E across the individual actuator channels at a low voltage difference. A potential difference of just 20 V across this 250 μm thick center layer produces the necessary field strength to achieve the 10 μL/min equivalent DC flow rate in Fig. 2.5 needed for active sublayer control on hydronautical vehicles, given the pumping capability of the porous polymer demonstrated in Fig. 5.8. The electrokinetic porous polymer matrix structure was filled in the liquid state in the microchannels by the two component polymerization process described in §5.2. The curing process produced a porous matrix with pore sizes in the range of 1 μm. Figure 5.20 shows an SEM image of the typical resulting pore structure. Note that pore sizes vary significantly, but are typically 1 μm or smaller, indicating a roughly 1 MHz theoretical frequency response limit based on the considerations in §4.4. The 10 kHz loss-less frequency response demonstrated with essentially the same porous polymer matrix in Fig. 5.9 is thus more than sufficient for the 1 kHz frequency response requirements in Figs. 2.4 and 2.5 for sublayer control on large hydronautical vehicles.

5.7.3   MEKA-5 Top Layer

The top layer of the MEKA-5 array was fabricated using photolithographic etching and other MEMS mass fabrication processes. This layer provides the 25,600 individual microactuator electrodes and leadouts, grouped into a unit-cell architecture as shown in Fig. 5.21. The layer was fabricated by a three-mask MEMS process consisting of an "electrodes mask", a "cavities mask", and a "nozzles mask", shown respectively in Figs. 5.21, and 5.22*a,b*. The fabrication process sequence developed for this MEMS top layer is shown in Table 5.1.

The major steps in this process are shown schematically in Fig. 5.23. A 525 μm silicon wafer was first used as a temporary substrate for the top layer. A 2 μm thick layer of aluminum was then sputtered on the top surface of this wafer – the entire MEKA-5 top layer was fabricated on top of this aluminum layer. The silicon wafer was used solely to provide support for the top layer and to permit handling during the fabrication process. Upon

completion of the fabrication process described below, this aluminum layer was etched away as shown in the last step in Fig. 5.23, to release the top layer from the silicon wafer.

As regards the fabrication of the top layer itself, a 6 μm thick layer of polyimide was first spin coated over the aluminum layer. Using the nozzles mask shown in Fig. 5.22*a*, the polyimide layer was then photolithographically patterned, unmasked, and exposed to define the 50 μm nozzle array. A layer of photoresist was then used to coat the entire surface. Using the electrode mask in Fig. 5.21, corresponding parts of this photoresist layer were then etched away. This defined the areas where the electrodes were to be located. A 4000 Å layer of chrome was then sputtered onto this surface, followed by another 4000 Å layer of gold. The use of Cr/Au for the electrodes proved to be important for the fabrication process, as early attempts to pattern the electrodes using platinum repeatedly failed because this material would consistently peel away from the underlying polyimide layer. A similar result occurred when gold alone was used. This Cr/Au double-layer was then patterned and unmasked using the electrode mask, and the photoresist then etched with acetone to expose the electrodes. Finally, a 125 μm thick layer of Su-8 material was deposited and selectively etched using the cavities mask shown in Fig. 5.22*b*. At this point, the top layer fabrication was complete, and the layer is released from the silicon support wafer by etching away the aluminum layer with a phosphoric-nitric-acetic acid mixture.

Fabrication of the complete top layer with this process sequence was done via MEMS Exchange in The University of Michigan's College of Engineering MEMS fabrication facilities. The three component sublayers that make up the top layer are named after the masks used to fabricate them. A full-tile view of the "electrodes sublayer" is shown in Fig. 5.24*a*. This sublayer provides Cr/Au electrodes for each of the 25,600 individual microactuators and the corresponding leadout for each actuator to a contact located near the edge of its unit cell. A region of this electrodes sublayer is shown in Figs. 5.24*b*, where the repeated pattern in twenty adjacent units cells can be seen. A closer view of a single unit-cell in this structure is shown in Fig. 5.25*a*, with the sixteen unit-cell contacts for each of the individual electrodes in the unit cell, together with the common voltage bus

lines that run between adjacent unit cells. These voltage bus lines can be readily seen in Fig. 5.25*b*. Future versions of this MEKA-5 array could contain a digital signal processing (DSP) layer that selectively connects each of these contacts to the bus line with either positive or negative polarity, depending on the actuation state vector implied by the sensor states. As described in §3, this could be readily done via a look-up table approach using a simple programmable logic array (PLA), in place of more traditional control logic approaches based on comparatively elaborate signal processing.

The "nozzles sublayer" is etched in polyamide and provides the 50 μm nozzles through which the pumping induced by the electrokinetic flow occurs. A full view of the "cavities sublayer" is shown in Fig. 5.26*a*. This sublayer, fabricated in Su-8 material as described in the process flow, serves two specific functions. It provides the necessary structural support for the top layer, and at the same time provides the necessary separation between the top of the porous polymer matrix structure associated each microactuator channel in the center layer and the corresponding top-layer electrode. A closer view of the cavities sublayer in Fig. 5.26*b* shows the 250 μm diameter cavities on 325 μm center-to-center spacings, and reveals the comparatively well-defined edges of these cavities that result from the fabrication process described above.

5.7.4   System Architecture for MEKA-5 Microactuator Array

The architecture for arrays like MEKA-5 is based on a 4 × 4 unit-cell composed of wall shear stress sensors and electrokinetic microactuators. The top-surface electrode for each microchannel has a leadout that runs to a contact near the edge of the unit cell. All the unit cells within the tile share a common ground electrode in the bottom layer. A power bus for the entire tile, held at constant reference voltage V_{ref}, runs along horizontal and vertical lines between the active areas of adjacent unit-cells. This redundancy makes the array highly fault tolerant to damage. The look-up table logic circuit provides a three-state bridge between the electrode contact for each of the microactuators and the corresponding closest power bus line. As noted in §3, on each clock cycle the actuator state vector $\{A_i\}$ obtained via the programmable logic array from the sensor state vector $\{S_i\}$ sets the volt-

age A_iV_{ref} of the top electrode for each actuator. This produces positive volume displacement on some actuators, negative displacements on some actuators, and no action on the remaining actuators. The space between adjacent unit cells on the MEKA-5 array appears sufficient to accommodate the relatively simple circuitry needed to implement this system architecture.

5.8   Laboratory Demonstration of Synthetic Vortex Manipulation

The various generations of electrokinetic microactuator arrays shown in the previous sections have demonstrated key performance and fabrication requirements for use of the electrokinetic principle in actuator arrays designed for active sublayer control under full-scale vehicle conditions. However, direct flow visualizations showing the lateral displacement of naturally-occurring sublayer vortices in turbulent boundary layers would be exceedingly difficult due to the very small size of these vortices and the fast time scales associated with them (see §2). Similarly, direct measurements of drag reduction resulting from active sublayer control using a set of such electrokinetic microactuators would require a complete control system, including sensors and control processing, which is beyond the scope of the present study. For these reasons, a set of flow visualization experiments was instead conducted to demonstrate lateral displacement of a synthetically-generated streamwise vortex in the vicinity of a wall by volumetric pumping from the wall. This is essentially the mechanism by which the present electrokinetic microactuators work, but allows the experiment to be conducted at much larger scales.

These experiments to demonstrate manipulation of synthetic streamwise near-wall vortices via wall pumping were conducted in a simple wind tunnel. The basic layout is shown schematically in Fig. 5.27. A streamwise vortex of circulation Γ was synthetically generated by a small rectangular wing held at a fixed angle-of-attack and located a small distance behind the leading edge of a flat plate mounted in the wind tunnel. The flat plate is shown in Fig. 5.28, and was mounted on a computer-controlled positioning stage that permitted precise positioning of the streamwise vortex within the field-of-view of the PIV

measurement system. The flat plate had a rounded leading edge and a flap to increase circulation and thereby prevent boundary layer separation. In this two-dimensional experiment, pumping from the wall was accomplished through a slot aligned with the flow, and the vortex displacement is measured in the crossplane flow. Because electrokinetic pumping is effective only at the microscale, the volumetric pumping in this case was accomplished by steady air injection at various rates through the slot from a pressurized plenum. The principle aim of the experiments was to demonstrate lateral displacement of the streamwise vortex by wall pumping, and to characterize the relative lateral displacement achieved as a function of the wall pumping rate, the vortex strength, and the position of the vortex relative to the location at which the wall pumping occurs.

5.8.1 Wind Tunnel Facility

The experiment was conducted in a low speed wind tunnel that was specifically designed and fabricated for this study. This suction wind tunnel, shown in Figs. 5.29-5.31, operated on an induced draft created by the ventilation system in the laboratory, which allowed for simple removal of the submicron-scale seeding particles. The three main sections of this wind tunnel are shown schematically in Figs. 5.29 and 5.30. A seeding section, shown in Fig. 5.29*a*, is located at the extreme upstream end, where the induced flow enters the tunnel and mixes with seed particles introduced through four jets issuing from the sidewalls. Effective mixing of the seed particles is enhanced by turbulence created from a set of randomly spaced holes of various diameters through which the induced air enters the tunnel. The flow then passes through a straightening section composed of a series of two screens, a perforated plate, and a honeycomb section (also evident in Fig. 5.29a) that reduces the free stream turbulence level in the test section to less than 3% at speeds as low as 0.1 m/s, as measured by the PIV system. The test section has interior cross-sectional dimensions of 36 cm × 30 cm and is 96 cm long. The test section has four glass windows for optical access of the PIV cameras through the side walls, as can be seen in Figs. 5.30*a,b*, to minimize the optical distortions produced by the acrylic test section walls. The locations of the four PIV cameras as well as their orientations with respect to the wind tunnel are shown in Figs. 5.32*a-d*.

5.8.2   Stereo Particle Image Velocimetry SPIV System

A unique dual-plane two-color stereo PIV system was assembled for these experiments, which in principle can permit highly resolved measurements of all nine components in the velocity gradient tensor field $\nabla\mathbf{u}(\mathbf{x},t)$. The basic layout of the DSPIV system is shown in Fig. 5.33. The system uses four frequency-doubled Nd:YAG lasers (Spectra-Physics) to provide beams at 532 nm (green) with roughly 10 nsec pulse length. Two of these beams are used to pump a dye laser, which provides output centered around 623 nm (red). The green and red beams from two of the lasers are formed into parallel light sheets that inter-sect the synthetic streamwise vortical structure. Each of the green and red light sheets is double-pulsed by time-separating the corresponding pulses from the two pairs of Nd:YAG lasers. Two stereo PIV systems (LaVision) are used to record particle images from the green and red light sheets. Optical filters allow each pair of cameras to see only one light-sheet color. The two SPIV systems are slaved together and operated via a custom master-slave software arrangement developed for this application by LaVision. Process-ing of the two separate stereo PIV image pairs produces the velocity field $\mathbf{u}(\mathbf{x},t)$ and, more importantly, the full velocity gradient field $\nabla\mathbf{u}(\mathbf{x},t)$, as indicated in Fig. 5.34.

In the current study, this system was operated in the single stereo PIV mode. The dou-ble-frame/double-exposure measurements were made with two fast shuttered PIV cameras (PCO SensiCam SVGA, 1280×1024 pixels, 6.7 mm $\times$ 6.7 mm pixel size). The double image from both cameras was stored in a single buffer. There are thus four frames in each buffer, with the order of each frame shown in Fig. 5.35. The 3-component vector calcula-tion was performed using the 3D stereo cross-correlation mode in the Davis 6.2.0 (LaVi-sion) software package. As is common in the evaluation of PIV recordings, the images were divided into 32×32-pixel "interrogation windows". The cross-correlation algorithm operates on the intensities inside each interrogation window, yielding one velocity vector for each window. With the interrogation window size set to 32×32 pixels, using a camera with a CCD chip having 1280×1024 pixels, the image is divided into 40×32 cells. The processing algorithm used a 50-percent overlap between neighboring interrogation win-dows, which produced a final image comprised of an array of 79×63 vectors (*i.e.,* 4977

uniformly-spaced vectors). Furthermore, an adaptive multipass algorithm was used in the Davis software which allowed for successively smaller final interrogation window sizes that would be possible without adaptive window shifting. This approach also improves the spatial resolution of the final vector field.

Two-dimensional velocity vectors were calculated for each of Camera 1 and Camera 2 by applying the stereo cross-correlation to four-frame buffers of the type shown in Fig. 5.35. The three-dimensional vector at each point was then calculated from the two-dimensional vectors obtained from Camera 1 and Camera 2 by using the local viewing angle and relative orientation of the two cameras. This was achieved by a transformation defined from mapping functions created for Camera 1 and Camera 2 during the stereo three-dimensional calibration process (*e.g.,* Soloff *et al* 1997). The resulting system of equations is overspecifed, and thus allows for an additional check to determine if the computed vectors are valid to improve the accuracy of the measurements.

The two 532 nm green beams, with energies in excess of 100 mJ, were combined in a laser sheet that crossed the test section perpendicular to the freestream flow. This laser sheet was approximately 1 mm thick and 2 cm wide. The laser flashlamps and Q-switches operate at 10 Hz to produce 10 ns pulse widths. The time separation between the two laser pulses that provided the highest good-vector percentage was found to be 90 μs for this experiment. This time delay, as well as the laser Q-switches and flashlamps, were controlled by a PC-based programmable timing unit (PTU) integrated with the rest of the PIV system software (LaVision DaVis 6.2). The PTU also synchronizes the triggering of the lasers and cameras.

5.8.3 PIV Results

All the PIV results shown in this section cover a field of view of 12 mm × 15 mm. The measurements thus span from the surface of the plate to 12 mm above the plate (the y-direction) and approximately 15 mm in the transverse direction (x direction). For convenience, the center of the wall actuator is defined as (x, y) = (0, 0). The measurements

were made 20 cm in the downstream direction (z direction) from the leading edge of the plate.

The first set of images, shown in Fig. 5.36, gives the transverse and streamwise velocity field for the laminar boundary layer over the flat plate at a streamwise velocity of $U = 0.6$ m/s. In this baseline case, the streamwise vortex generator was removed, so that there was no vortex in the flow. The Blasius solution for the laminar boundary layer thickness on a flat plate indicates an expected value for $\delta_{99\%}$ of 9.5 mm at these conditions. This value is comparable to the results shown in Fig. 5.37, where $\delta_{99\%}$ is found to be approximately 8 mm. The use of a flap at the trailing edge of the plate, set to a small angle to provide positive circulation around the plate and thereby produce a slight favorable pressure gradient, results in a reduced growth rate of the boundary layer and accounts for the smaller measured value of $\delta_{99\%}$. Figure 5.37 also verifies that the boundary layer velocity profile remains essentially the same at the various transverse locations shown. Typical vorticity and shear strain rate fields for this laminar boundary layer are shown in Figs. 5.38 and 5.39, respectively.

Next, the velocity field for the boundary layer with the synthetic streamwise vortex, created by the small wing upstream of the measurement location, is shown in Fig. 5.40. In this second baseline case, there was no flow issuing from the wall actuator. The center of the vortex is seen to be located approximately 4 mm above the plate, and less than 1 mm to the left of the center of the slot actuator. The downward motion of fluid created by the vortex on its left side significantly decreases the thickness of the boundary layer in that region, as seen in Fig. 5.41 at x = –5 mm. The opposite is true on the right side of the vortex, as seen in Fig. 5.41 for x = 5 mm. At x = 0 in Fig. 5.41, which is close to the center of the vortex, the streamwise component of the velocity shows an inflection point, as would also be expected. In addition, due to the presence of the vortex an accumulation of low speed fluid occurs near the wall at the right side of the vortex. In Fig. 5.42, the instantaneous and ensemble-averaged vorticity fields ω_z associated with the velocity fields in Fig. 5.40 show the presence of the streamwise vortex with a reasonably well-defined core. Similarly, the presence of the vortex in this viscous region generates the shear strain rate

field shown in Fig. 5.43.

The PIV results presented up to this point corresponds to the wall actuator being "turned off", so that there is no blowing (or suction) by the actuator at the wall. The resulting configuration is shown schematically in Fig. 5.44*a*, where a vortex of strength Γ is located at a distance $h = 4$ mm above the wall and at a distance $b = 1$ mm from the center of the slot actuator. When the wall actuator is "turned on", so that there is a constant volume flow rate q per unit actuator length introduced at the wall, then the resulting configuration is as shown schematically in Fig. 5.44*b*. In this case, when the vortex has the sense of circulation as shown and is located to the left of the actuator, then the volumetric pumping at the wall should displace the vortex to the left by a distance l from its original location.

Corresponding PIV results for the velocity field under the influence of such wall actuation are shown in Figs. 5.45-5.48. As anticipated, the vortex is seen to be displaced in the lateral direction to the left as a result of the low-speed fluid being pumped by the actuator. Furthermore, this low-speed flow is accumulated to the right of the actuator, as can be seen in Fig. 5.45, due to the influence of the region of the vortex with an upward motion. This tends to modify the boundary layer as shown in Fig. 5.46. Also, in the vorticity in Fig. 5.47, the vortex core can be readily seen to be moved to the left in relation to Fig. 5.41, directly demonstrating the lateral displacement of the vortex. Similarly, a reorientation of the shear strain rate occurs under the presence of wall actuation, as seen in Fig. 5.48. Similar PIV results were obtained at several different values of the volume flow rate q introduced by the wall actuator.

For a given initial position of the vortex relative to the actuator, the lateral displacement of the vortex induced by the actuation was seen to depend on the vortex strength Γ and the volume flow rate q. The PIV results indicate a strong correlation between the relative lateral displacement l/h of the vortex and the "relative pumping strength" q/Γ, as shown in Fig. 5.49. Furthermore, this plot shows that there is a relative pumping strength limit at which a plateau is reached, beyond which further increase in q/Γ produces little or no additional relative lateral displacement of the vortex. One possible explanation for this is

that, as was noted in Fig. 2.3, as the pumping strength q increases so does the local exit Reynolds number of the actuator flow. Eventually, the flow produced by the actuator will reach sufficiently high Reynolds number that it will exhibit a jet-like behavior, rather than the low Reynolds number radially-dominated flow indicated in Fig. 5.44. This would act to reduced the effectiveness of the actuator in producing lateral displacement of the streamwise vortex, consistent with the results seen in these experiments.
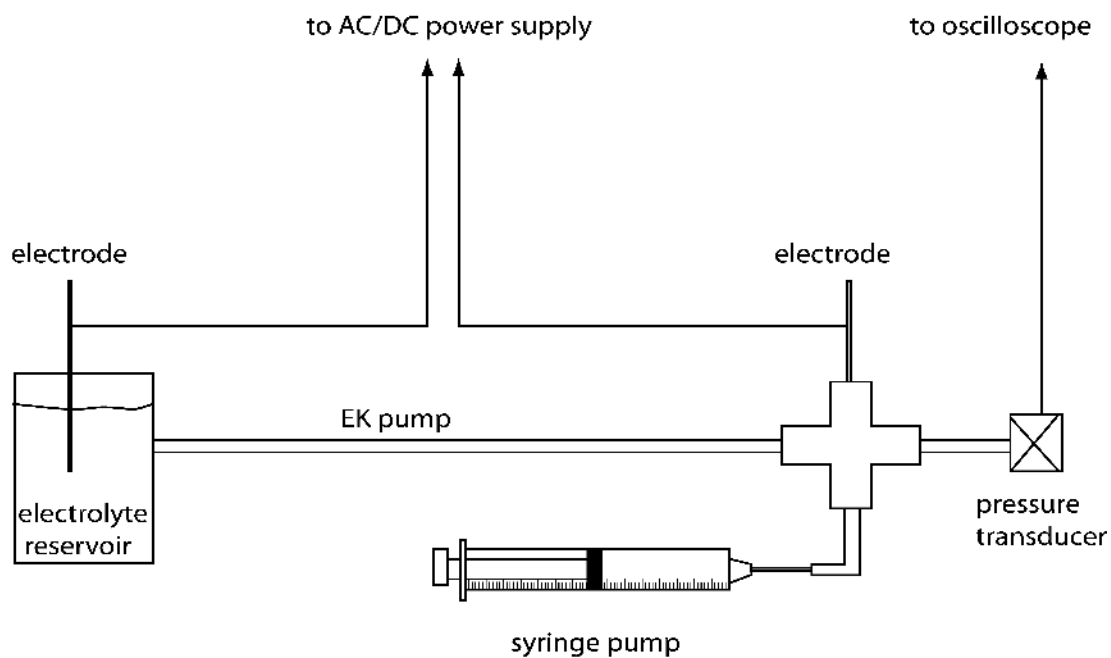
Figure 5.1.   Experimental configuration used for testing of elementary packed-channel actuators described in §5.1. Displacement of the syringe pump permitted volume flow rate measurements for various applied field strengths and electrokinetic pumping parameters. The pressure transducer permitted measurements of the pressure achieved in plugged actuators.
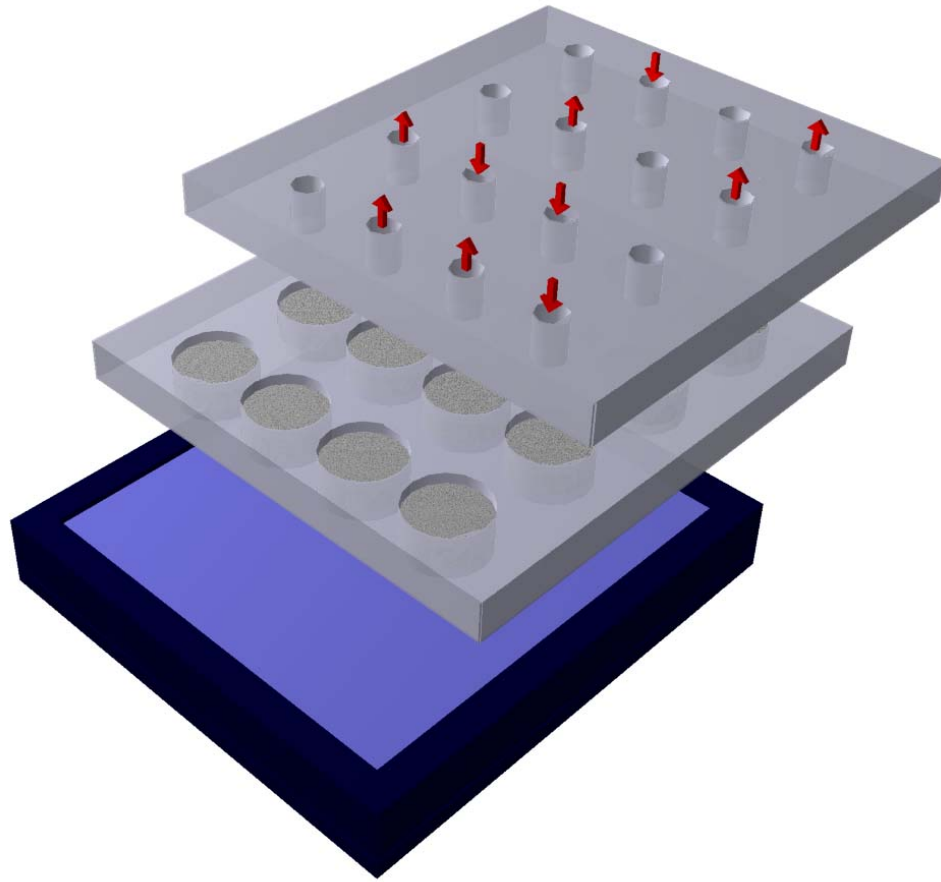
Figure 5.2.   Basic three-layer design of MEKA-0 through MEKA-5 electrokinetic microactuators arrays in §5, with center layer containing porous polymer matrix structure in which electrokinetic flow occurs. The 1 µm pore size indicates a theoretical frequency response limit near 500 kHz. Channel diameters ranged from mm-scales for the MEKA-0 and MEKA-2 UAV-scale microactuator arrays, to 250 µm for the MEKA-5 hydronautical-scale array, which contained 25,600 such individual microactuator channels.
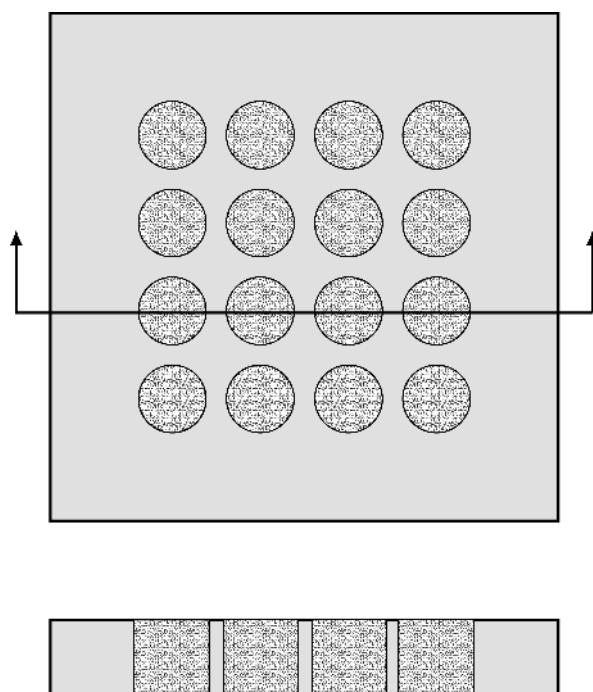
Figure 5.3. Typical center-layer structure showing electrokinetic driver channels filled with porous polymer matrix structure. Channels are fabricated to match the unit-cell actuator pattern, and completely filled with porous polymer. Electric field applied along channel length creates electrokinetic flow in porous matrix.
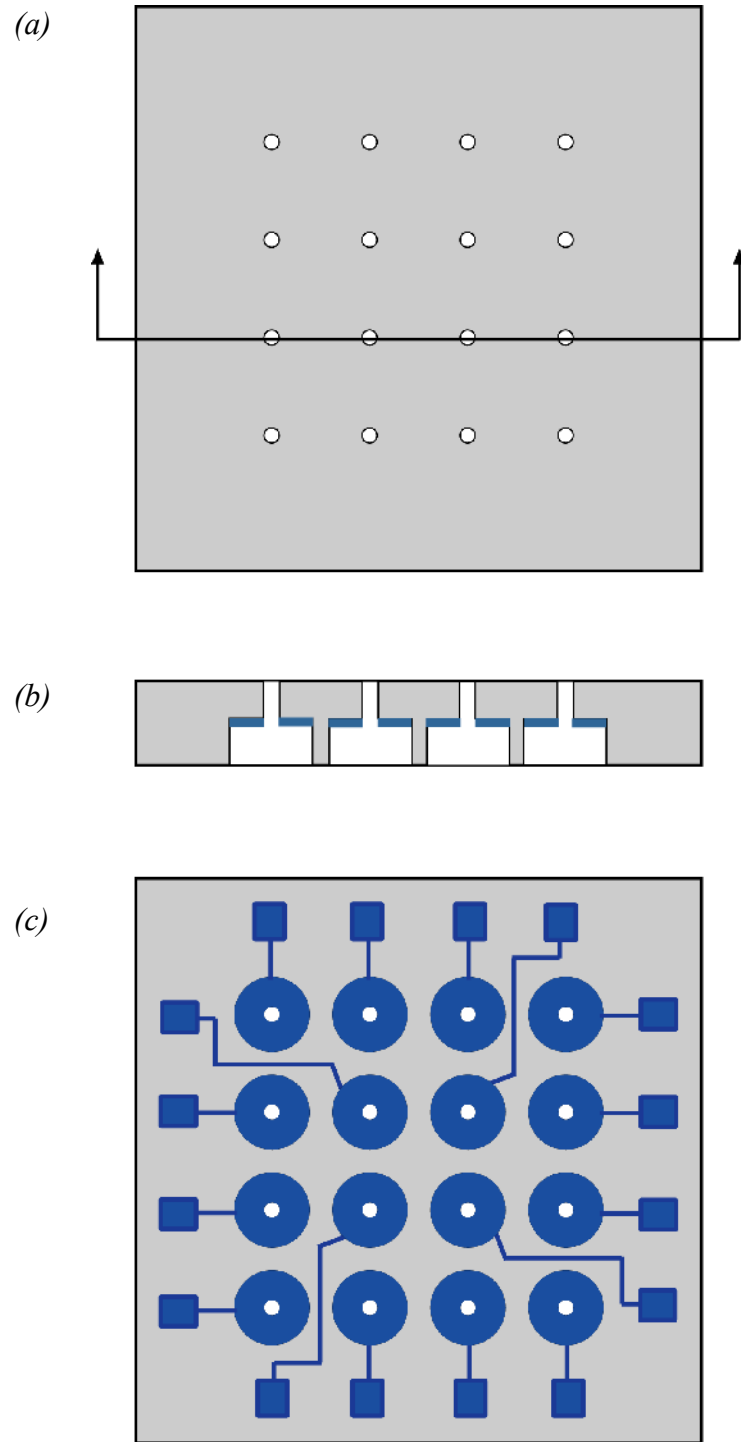
Figure 5.4 . Typical top-layer structure showing *(a)* actuator nozzles at top surface used to produce point volume source flow, *(b)* cross-sectional view showing cavity, electrode, and channels for each actuator, and *(c)* electrodes and leadouts to unit-cell contacts.
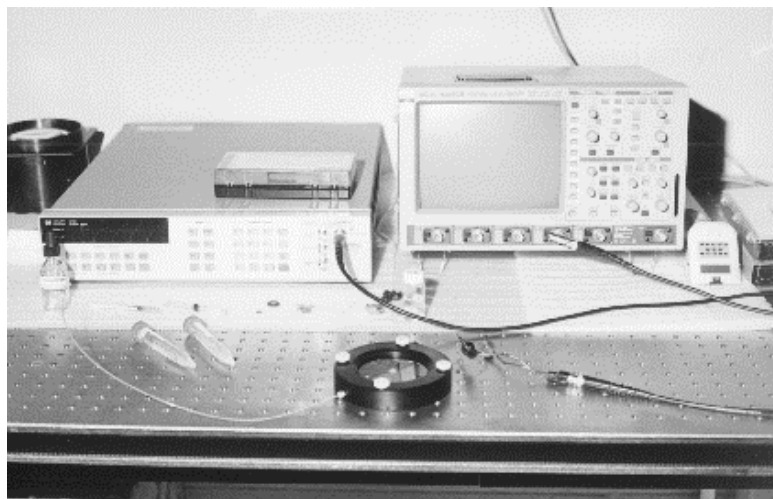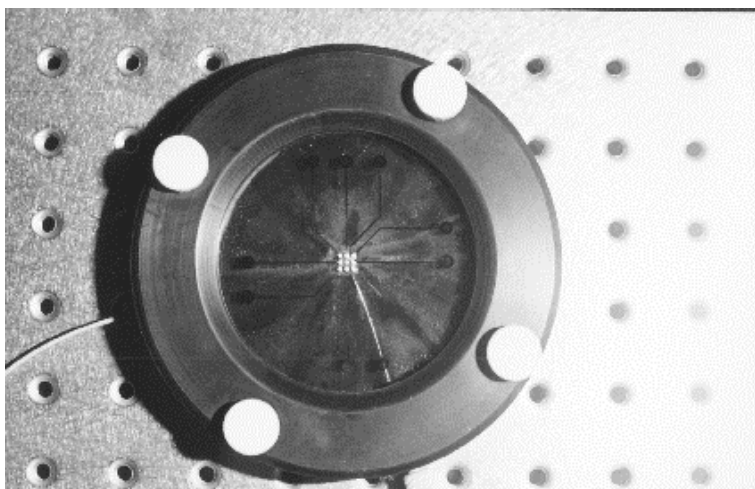
Figure 5.5.   MEKA-0 3 × 3 electrokinetic microactuator array, showing *(a)* experimental test set-up, *(b)* array in electrolyte reservoir, *(c)* array fabricated in glass, and *(d,e)* front and back surfaces of array showing metallization and porous polymer in channels.
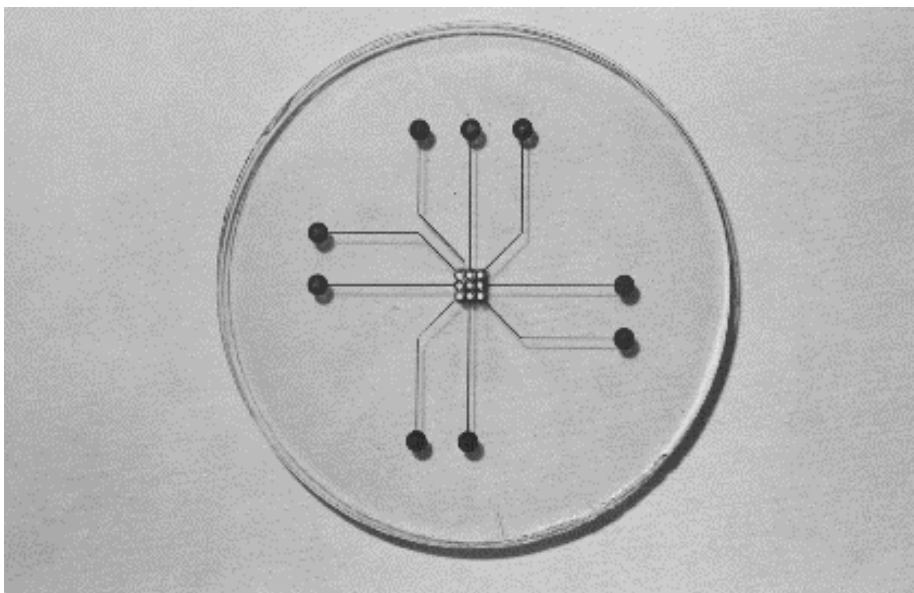
Figure 5.5.   (continued)

(d)
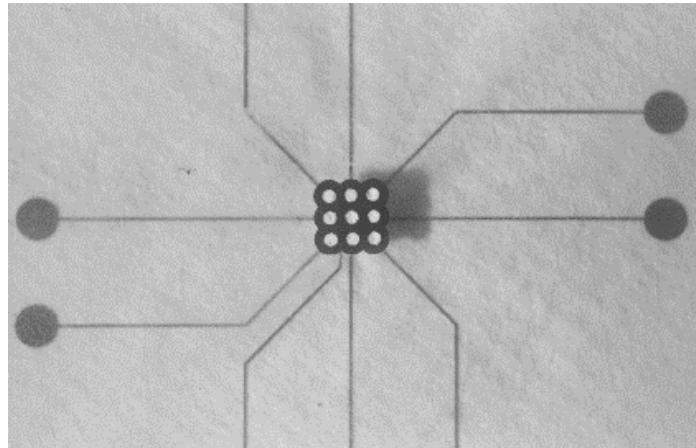
(e)
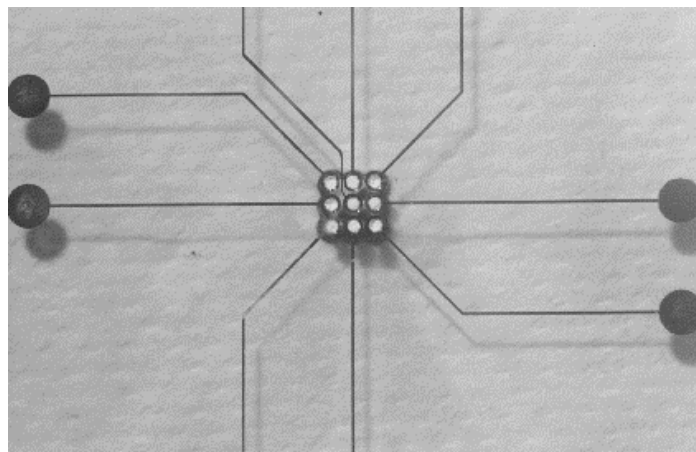
Figure 5.5.   (concluded)

(a)
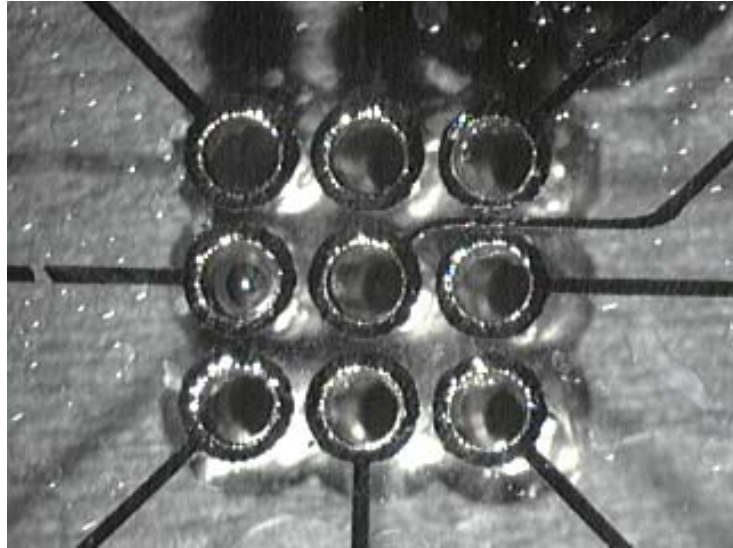
(b)

Figure 5.6.   Closeup views of MEKA-0 electrokinetic microactuator array prior to polymer filling, showing *(a,b)* top-surface ring electrodes for each actuator, *(c)* bottom-surface common electrode, and *(d)* channel edge chipping resulting from mechanical drilling in glass wafer.

(c)
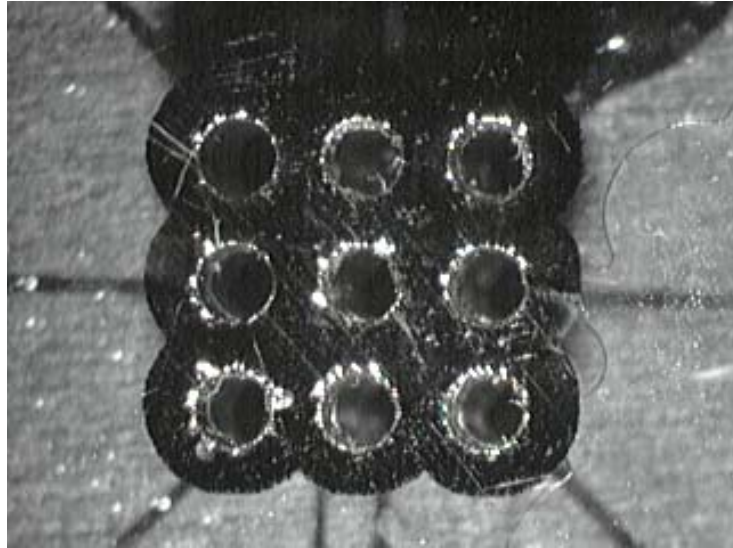
(d)
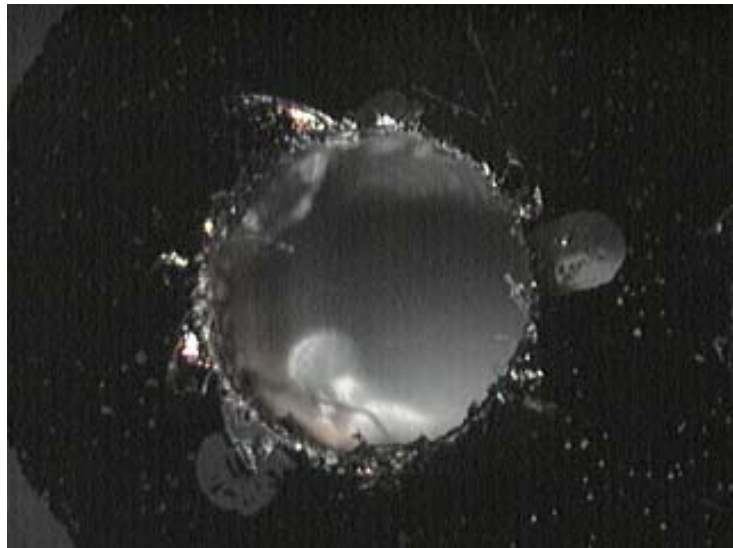
Figure 5.6.   (concluded)
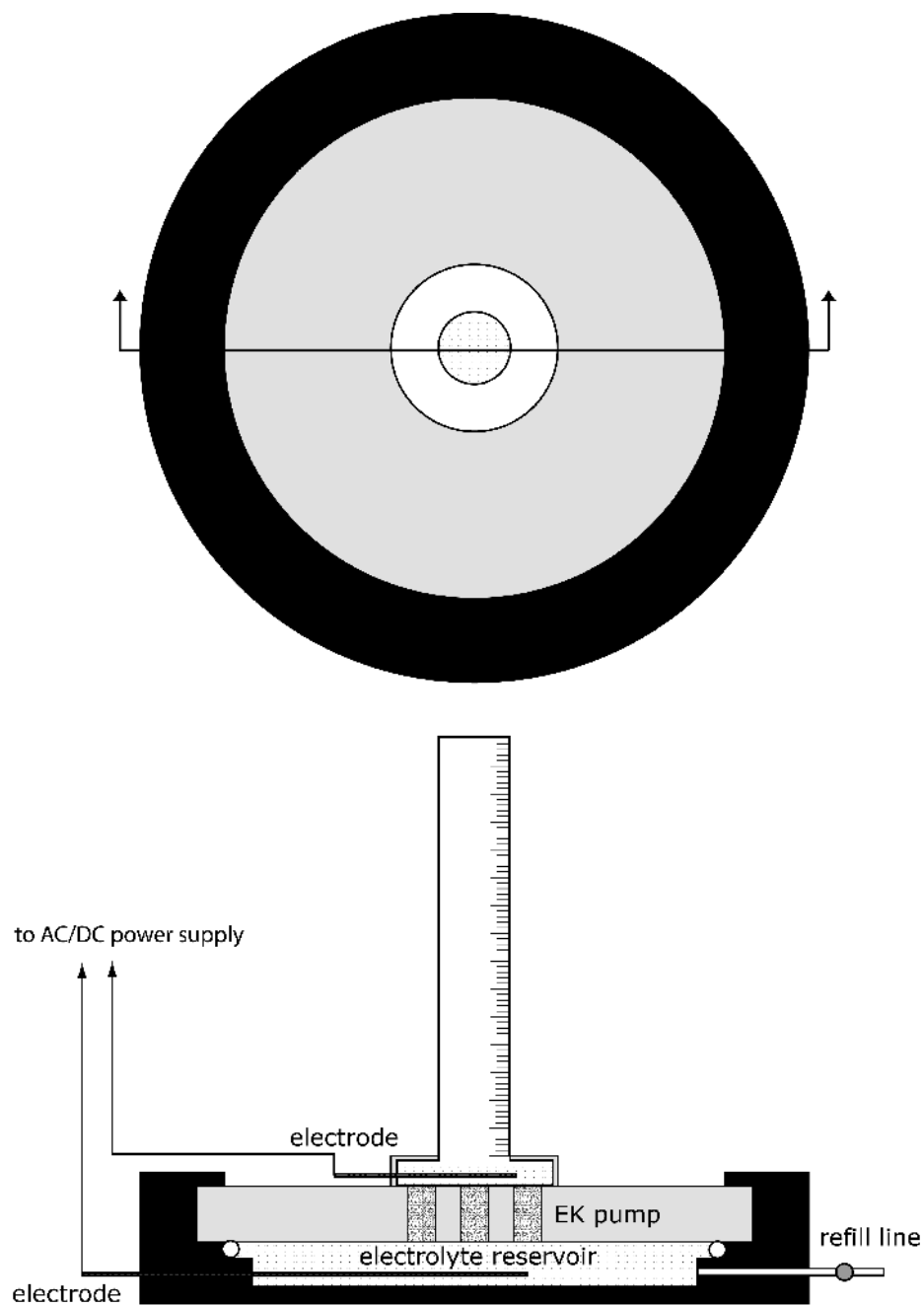
Figure 5.7.   Schematic of experimental apparatus used for steady flow rate measure-
ments with MEKA-1 electrokinetic microactuator array. Applied electric field strength
was determined from voltage of top-surface electrode and thickness of center layer.
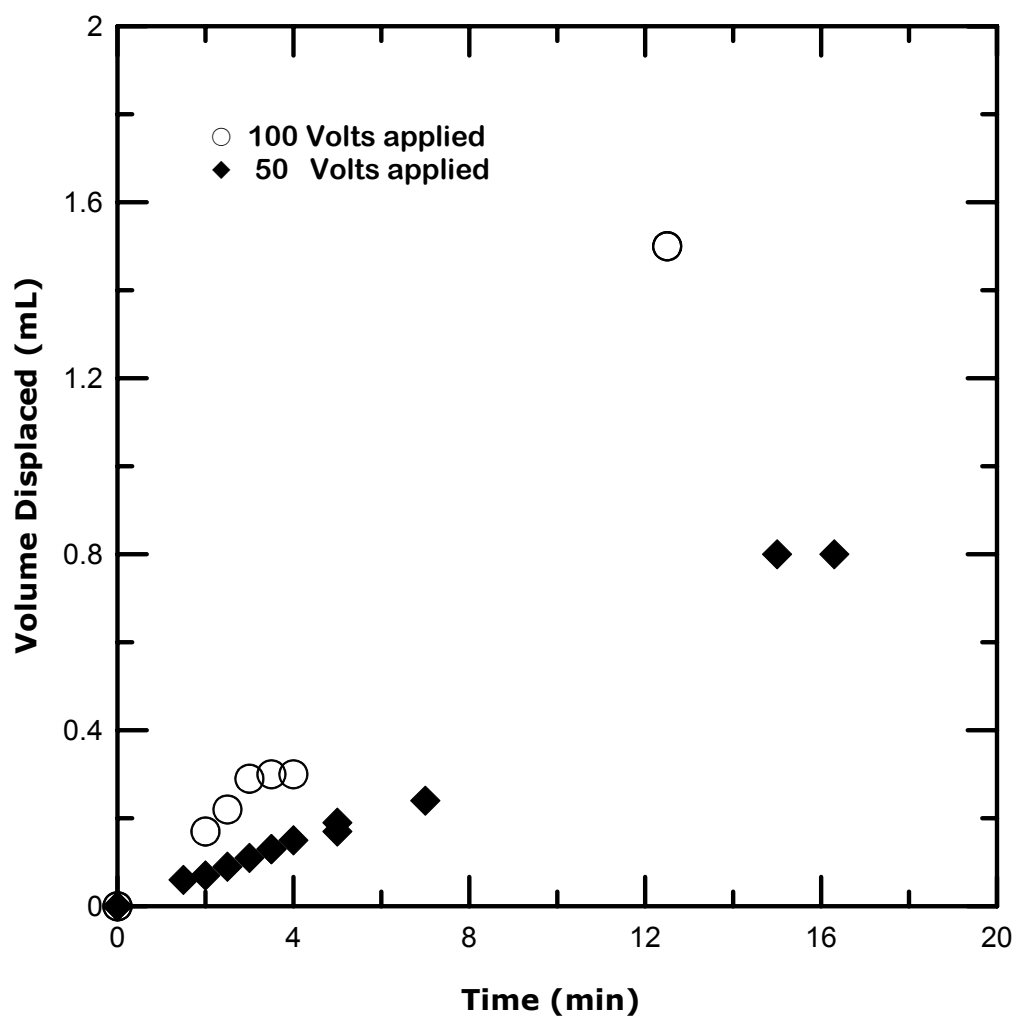
Figure 5.8.   Experimental results for steady electrokinetic pumping performance achieved with MEKA-1 array for two different applied voltages. Total displaced volume increased linearly with time, and varied with field strength as indicated in (4.23).
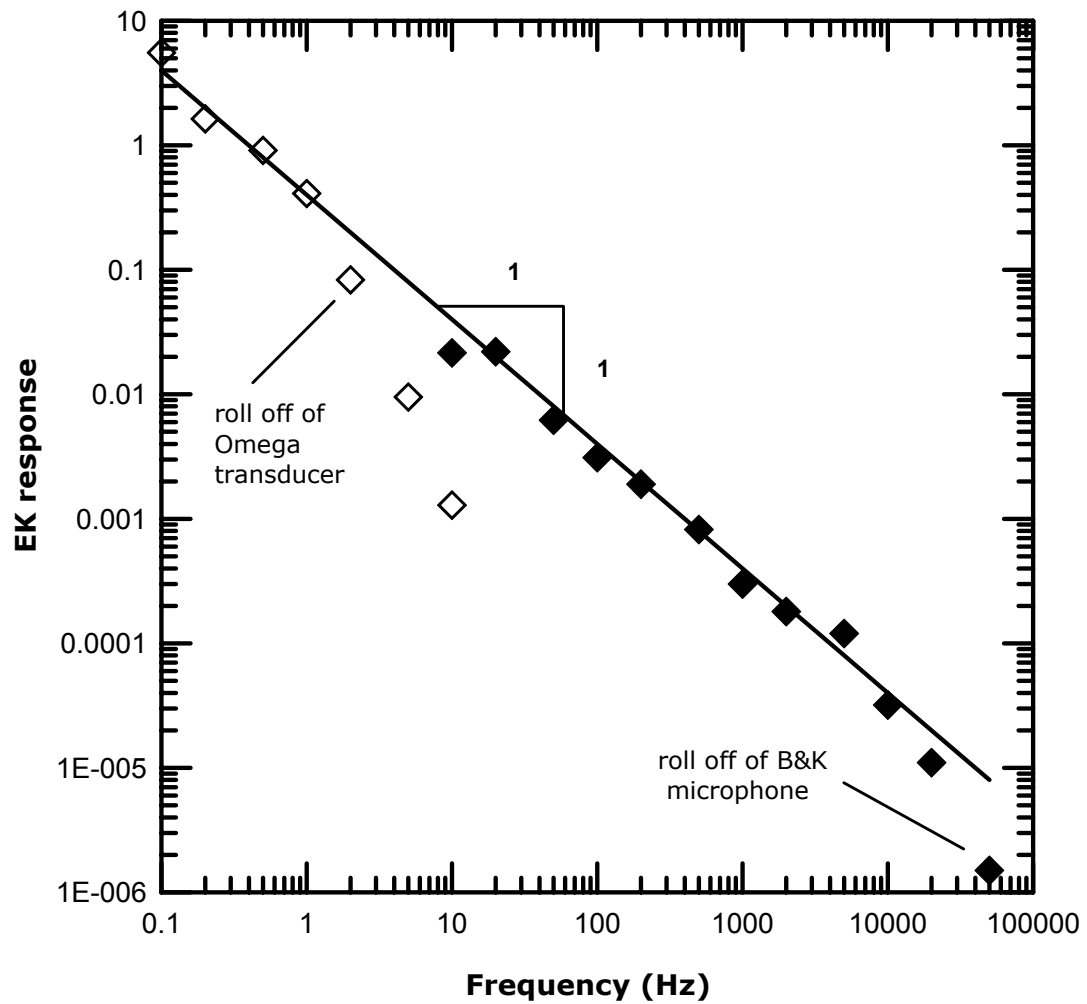
Figure 5.9.   Measured frequency response of an electrokinetic actuator for a sinusoidally time-varying applied field of various frequencies ω, showing results from a low-frequency pressure transducer and a high-frequency microphone. Solid line gives ω^{-1} roll-off corresponding to loss-less AC performance.
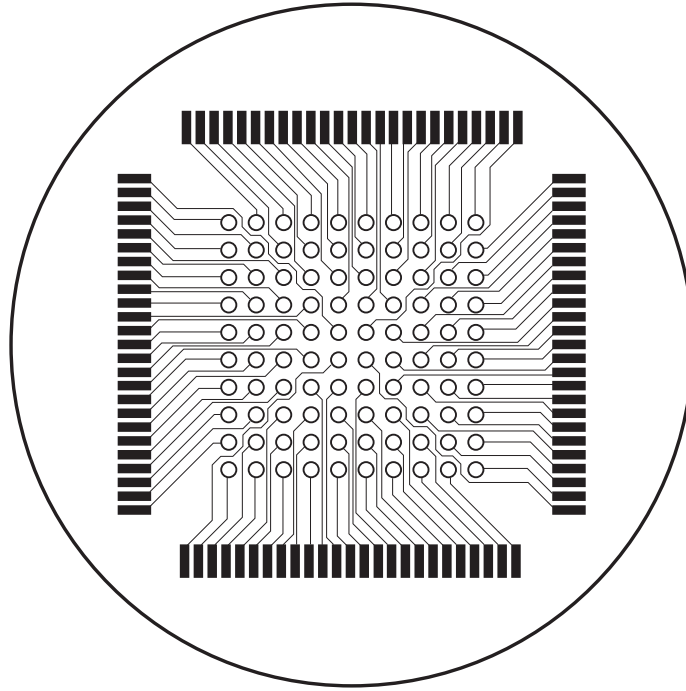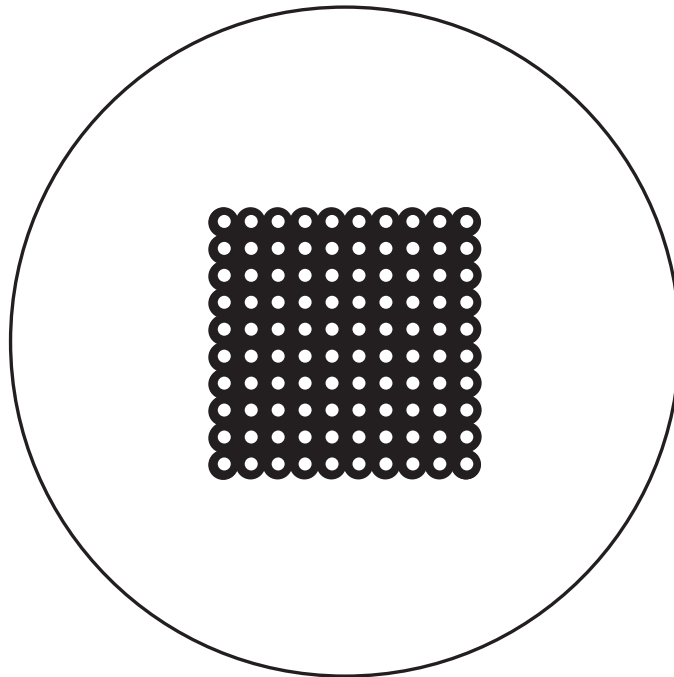
Figure 5.10. Electrode and leadout pattern for 10 × 10 MEKA-1 array , showing *(a)* individual top-surface ring electrode and leadout for each individual actuator channel, and *(b)* common bottom-surface electrode.

(a)
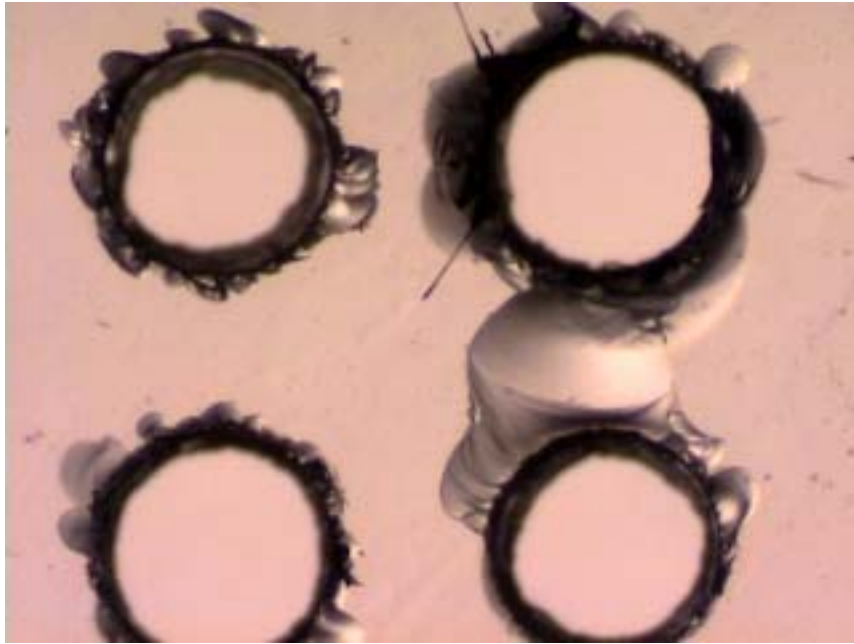
(b)
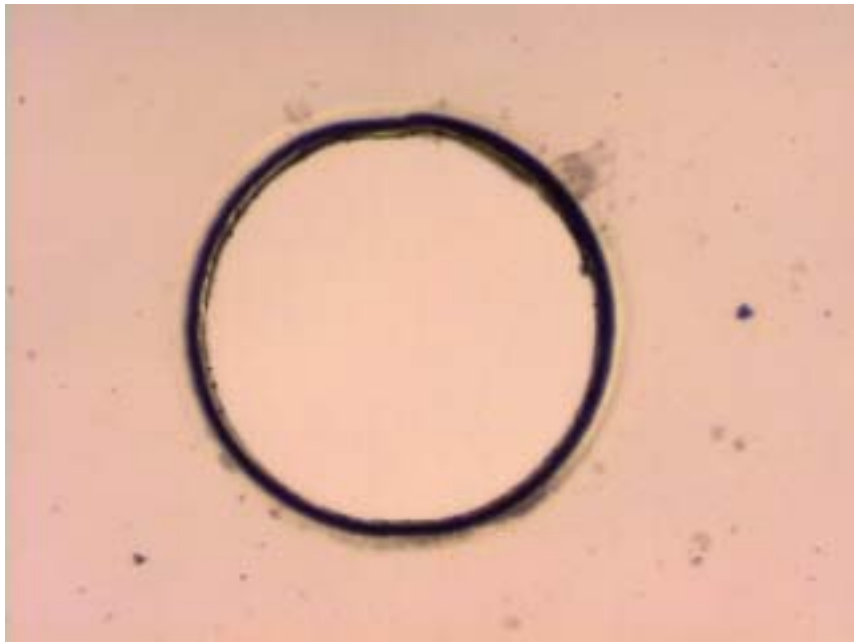
Figure 5.11. Comparison of actuator channel edge quality achieved by *(a)* mechanical drilling of glass substrate on MEKA-0 array, and *(b)* CO_2 laser drilling of glass substrate on MEKA-1 array.

(a)
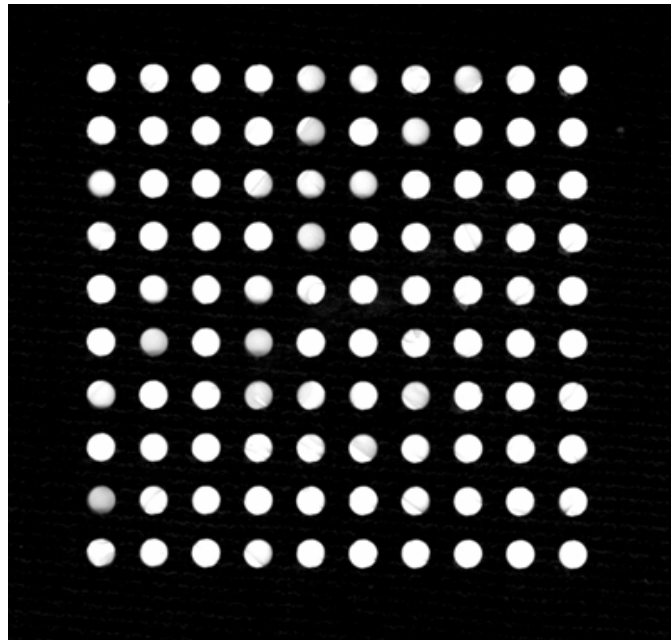
(b)
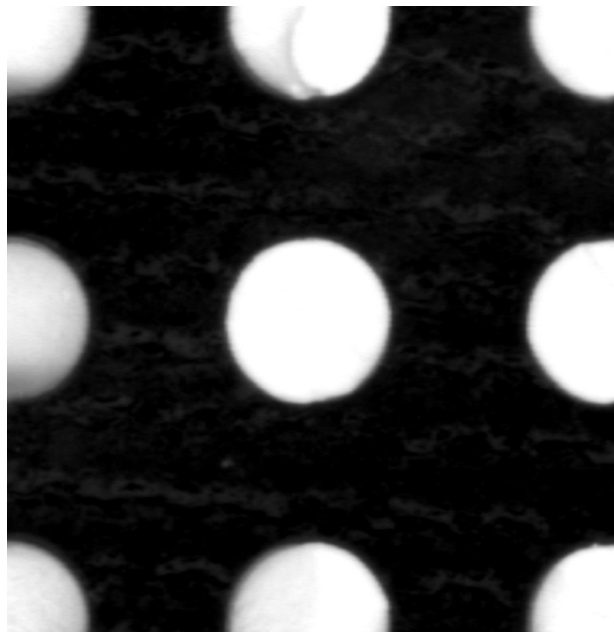
Figure 5.12.   Photographs of 1 µm porous polymer matrix structure filled in 10 ×
10 MEKA-1 array.

(a)
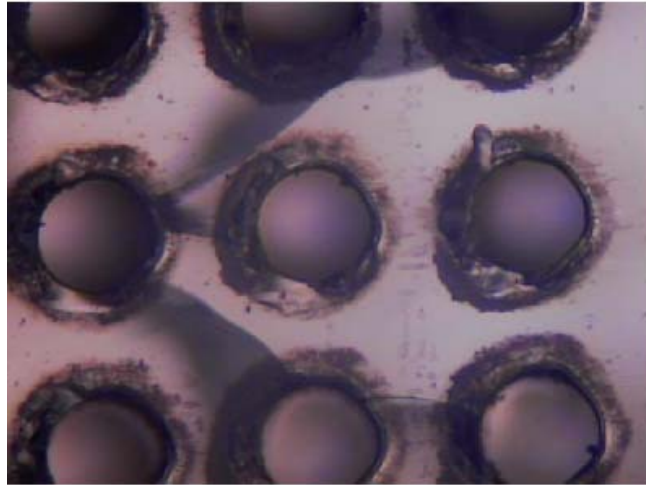
(b)
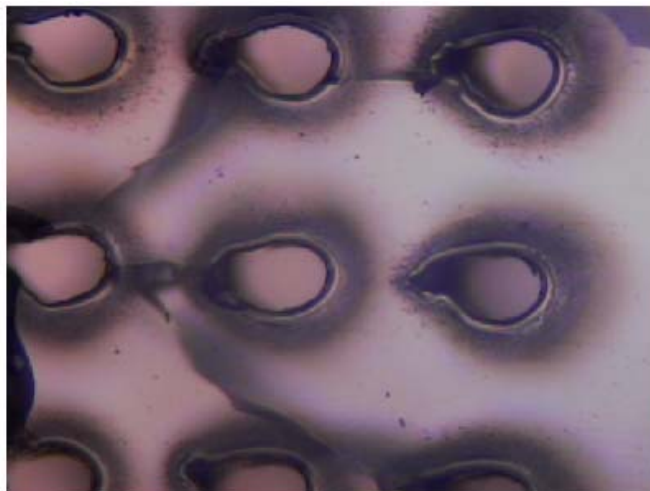
Figure 5.13.   Poor channel quality obtained by CO_2 laser drilling of 300 µm diameter holes on 500 µm center-to-center spacing in 2 mm thick glass substrate on MEKA-2 array, showing *(a)* entry side, and *(b)* exit side.

(a)

(b)
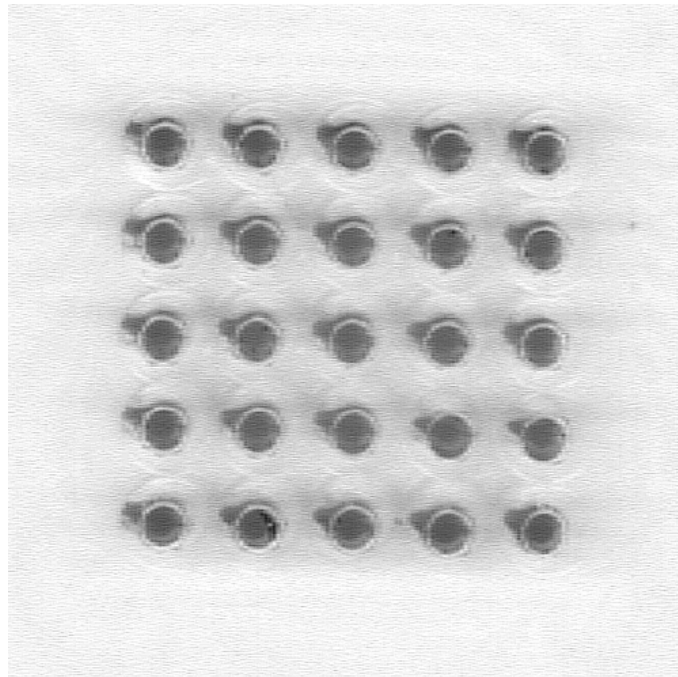
Figure 5.14. Actuator channels fabricated by CO_2 laser drilling of 300 μm diameter holes on 1000 μm center-to-center spacing in 2 mm thick acrylic substrate on MEKA-3 array, showing *(a)* complete wafer-scale view, and *(b)* exit-side view of actuator channels.

(a)

(b)
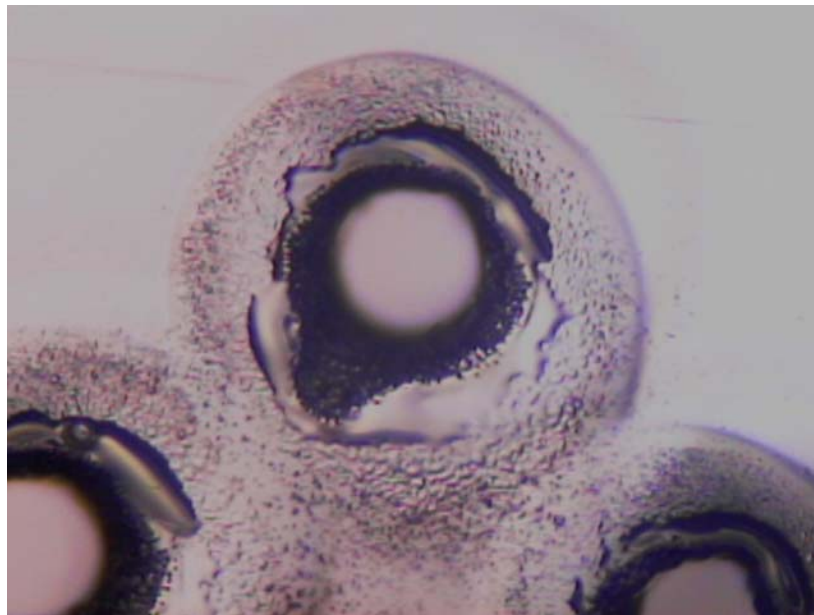
Figure 5.15. Close-up views of MEKA-3 actuator channels on *(a)* entry side, and *(b)* exit side.
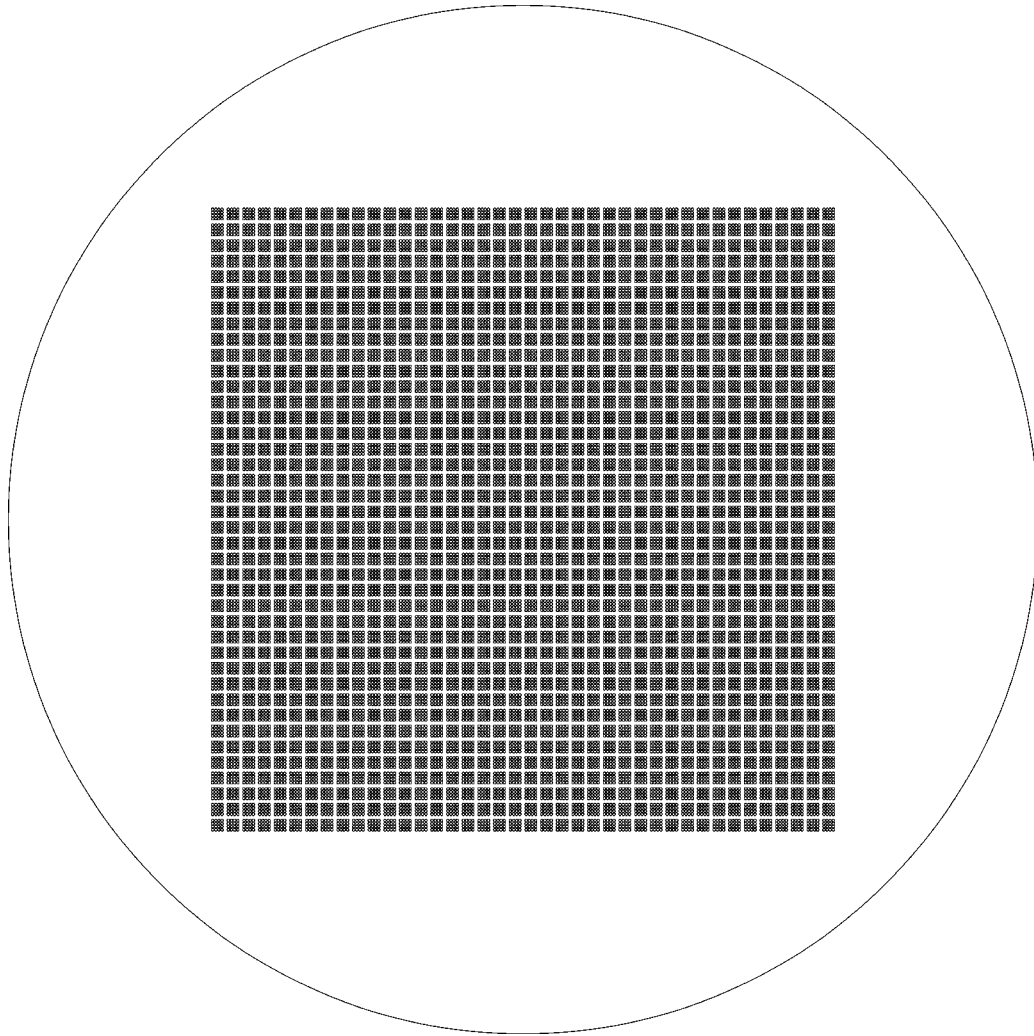
Figure 5.16.   Layout of electrokinetic microactuator channels in center layer of MEKA-5 full-scale hydronautical array, showing 25,600 individual microactuator channels grouped into a 40 × 40 pattern of unit cells, each containing a 4 × 4 unit-cell structure on 325 μm center-to-center spacing. Array is shown at actual size.
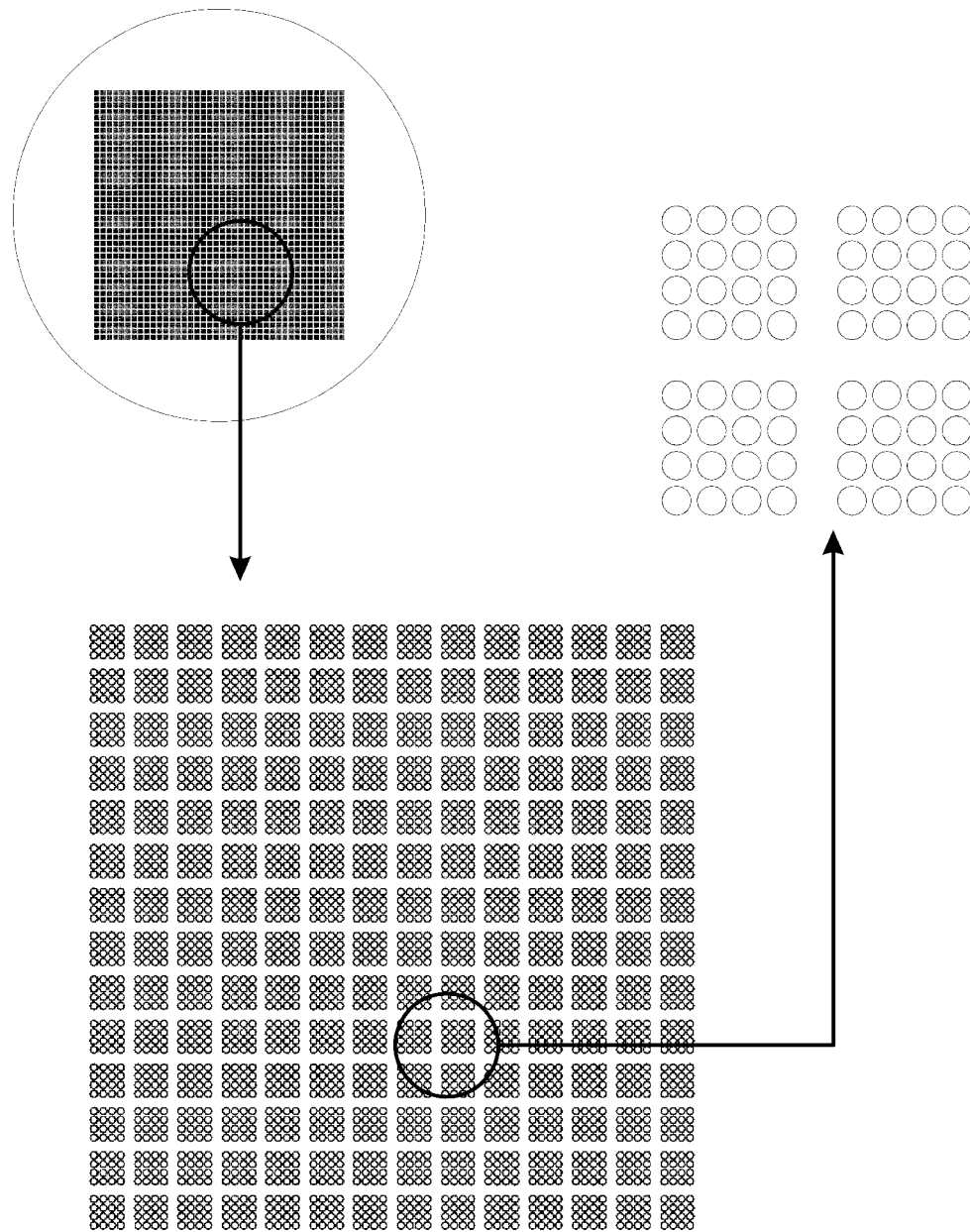
Figure 5.17. Unit-cell pattern on the MEKA-5 hydronautical-scale array, showing how full tile is arranged into individual 4 × 4 unit-cell structures. Every fifth row and column of actuators was skipped to provide space for unit-cell control processing.

(a) Top Layer

Cavity Layer   Electrode Layer   Nozzle Layer
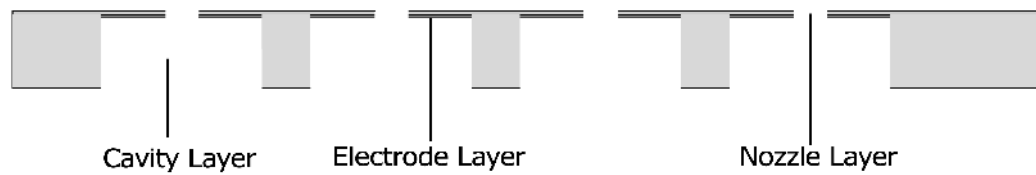
(b) Middle Layer
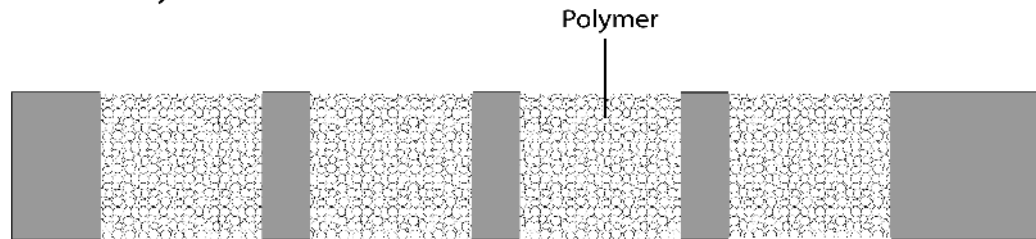
Polymer

Figure 5.18.   Basic elements fabricated in 25,600-element MEKA-5 hydronautical-scale array, showing *(a)* top layer with cavities, electrodes and leadouts, and nozzles, and *(b)* center layer with actuator channel and porous polymer matrix. Individual sub-layers are shown in Figs. 5.19-5.22. MEMS fabrication process steps are shown in Fig. 5.23.
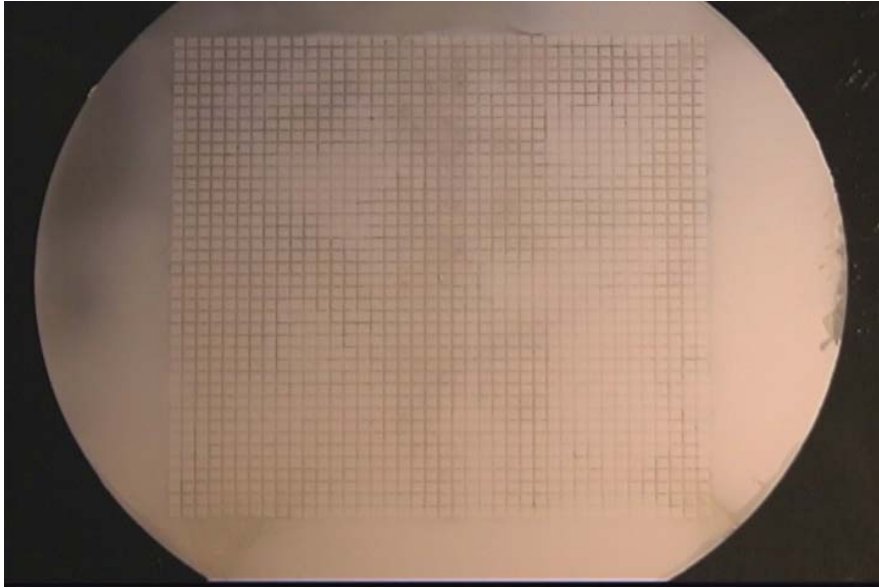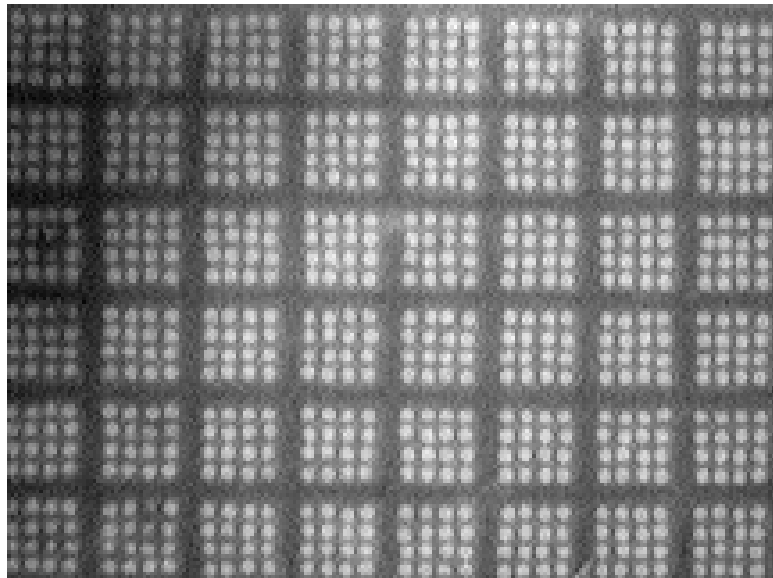
Figure 5.19. *(a)* Center layer of 25,600-element MEKA-5 hydronautical-scale array fabricated in thin flexible mylar, showing tile-scale view 250 μm diameter actuator channels filled with porous polymer matrix structure. *(b)* Close-up view of 250 μm diameter actuator channels filled with porous polymer matrix structure in MEKA-5 hydronautical-scale array, showing individual 4 × 4 unit-cells.
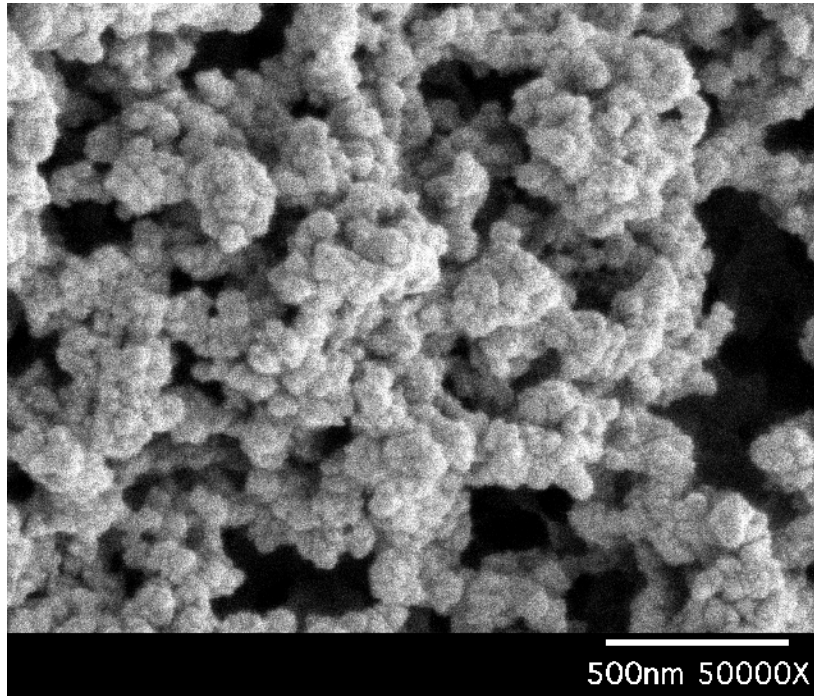
Figure 5.20.   SEM micron-scale photograph of the porous polymer matrix structure resulting from two-component polymer fabrication process of the type used in the MEKA-5 array.
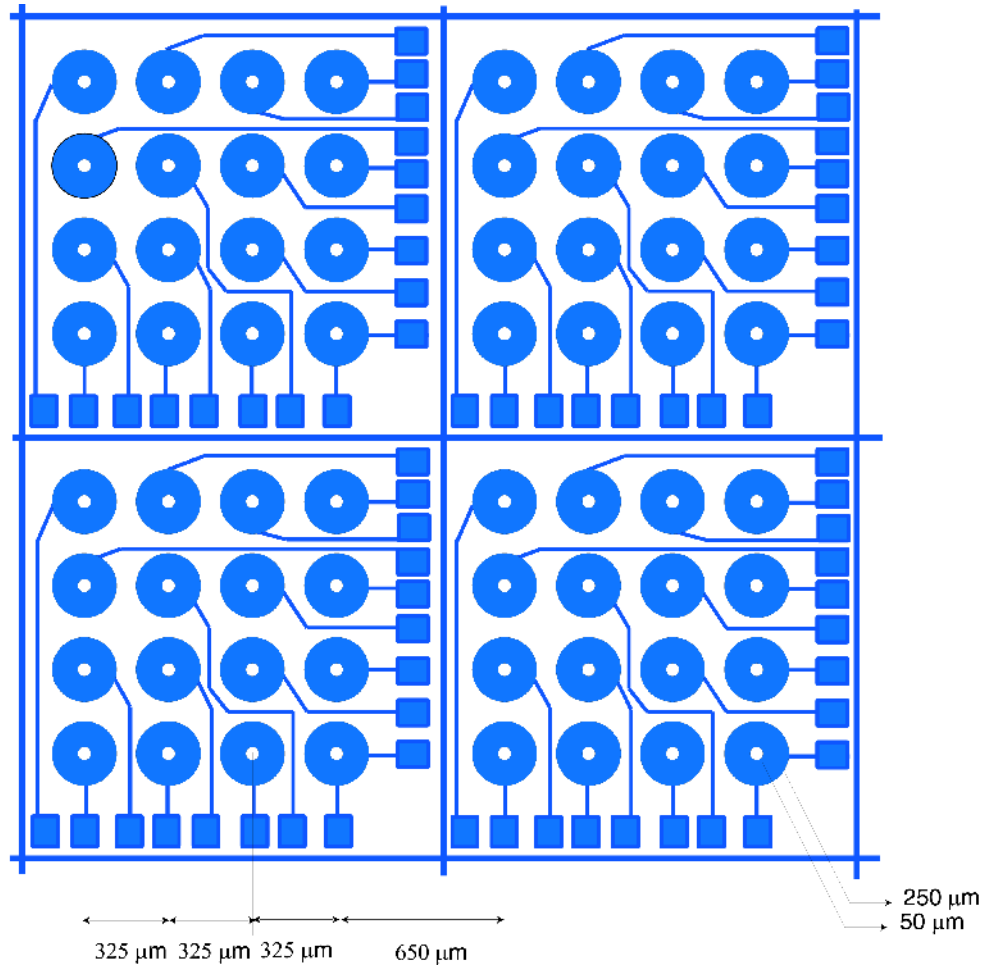
Figure 5.21.   Layout of top-surface electrodes sublayer mask for 25,600-element MEKA-5 array, showing disk electrodes with leadouts to contacts near edge of each unit cell, and common voltage bus lines running horizontally and vertically between adjacent unit cells.
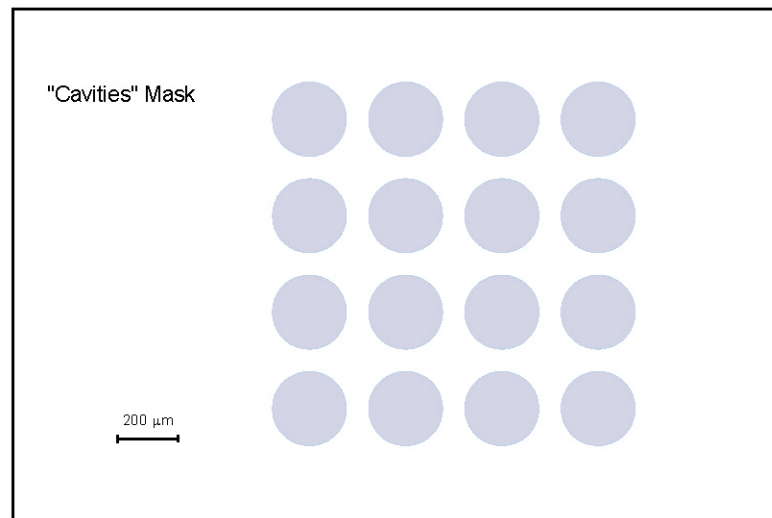
(a)

"Nozzles" Mask

200 μm

(b)

"Cavities" Mask

200 μm
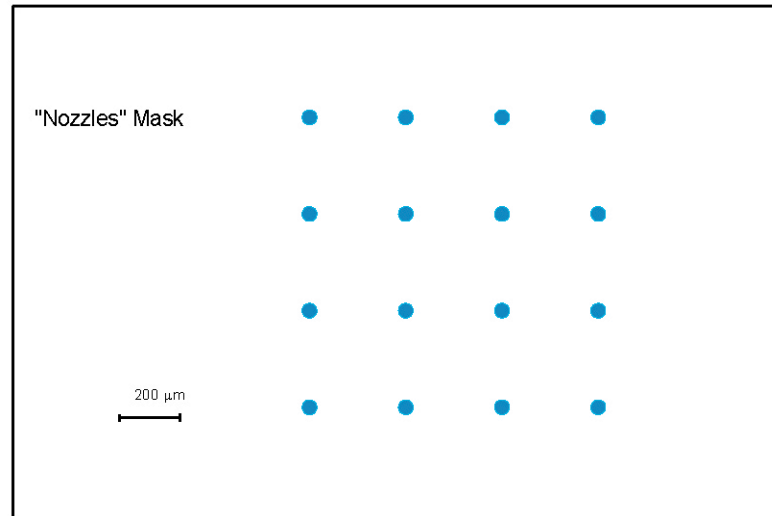
Figure 5.22.   Additional masks used in MEMS-fabrication of top layer for MEKA-5 hydronautical-scale array, showing *(a)* nozzles mask, and *(b)* cavities mask.

Process Step	Process Description
1	**Prepare starting wafers** • 0 p-type, single side polished, <100>, 1-20 [W-cm] • Rinse: DI-H_2O, 2 min; spin dry
2	**Sputter: Al release layer** • Target #3, Sputter 20000 Å Al at 5 A • 7 mT Ar with a pre-sputtet time of 2 min.
3	**Mask 1: Polyimide Nozzles Mask** • Spin: PI 2731 @ 500 rpm/8 sec, 4000 rpm/30 sec • Softbake: 75 min. @ 55° • Expose: on EV Aligner for 75 sec • Develop: to be done on spinner • Puddle DE9040 for ~70 secs • Transition to RI9180 with 250 rpm/10 sec • Rinse for ~30 sec at 3000 rpm/30 sec • Postbake: 30 min. @ 190°C • Postbake: 30 min. @ 300°C
4	**Mask 2: Metallization Mask** • Drybake: 15 min. @110°C • Spin: 1827 @ 4 Krpm • Softbake: 30 min. @ 90° • Expose: 26.5 sec on EV • Develop: 1.1minute in MF319
5	**Etch Oxide (~10 seconds in Buffered HF)**
6	**Sputter Cr/Au** • Load into chamber immediately after Step 5 • Pump down to 5×10^{-6} Torr (1.5 hr) • Target #1, Sputter 400 Å Cr at 650 W • 7 mT Ar with a pre-sputter time of 2 min, 3'15" • Target #3, Sputter 4000 Å Au at 0.5 A • 7 mT Ar with a pre-sputter time of 2 min., 14'
7	**Lift-Off of Cr/Au** • Lift-off: Soak in Acetone overnight • Sonicate in ultrasonic bath for ~10 sec • Rinse with IPA and DI for 3 minutes; spin dry and inspect for flakes
8	**Mask 3: SU-8** • Drybake: 10 min. @ 110°C • Spin: HMDS/SU-8 25 @5 sec/15 sec 500 rpm/690 rpm • Softbake: 5 min. @ 70°, 50 min. @ 90° • Expose: on EV Aligner • Bake: 1 min. @ 50°, 13 min. @ 90° • Develop: SU-8 developer in beaker for 5 min., • Change solution, 7 min., 30 sec spray • Rinse: DI-H_2O, 2 min.; spin dry
9	**Device Release**

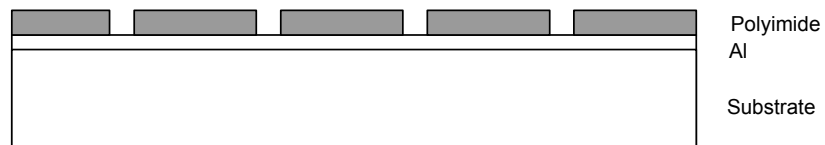Table 5.1.   MEMS process sequence for fabrication of top layer in MEKA-5 array.

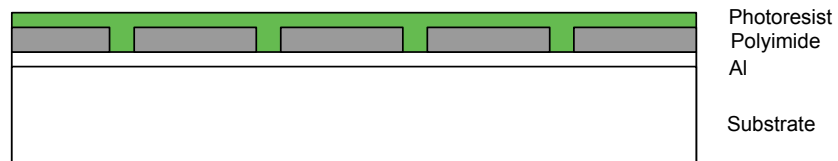*(a)*   Aluminum is deposited on a 525 μm silicon substrate (DC magnetron sputter)

Al (2 μm)

Substrate
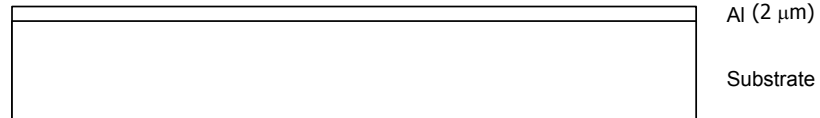
(b)   Polyimide is deposited (spin cast)

Polyimide (6 μm)
Al

Substrate

(c)   Patterned and unmasked polyimide is exposed with AZ 400K to define tthe 50 μm nozzles

Polyimide
Al

Substrate

(d)   Photoresist (Shipley 1827) coat is deposited (spin cast)

Photoresist
Polyimide
Al

Substrate

(e)   Patterned and unmasked photoresist is isotropically wet etched with MF-319

Photoresist
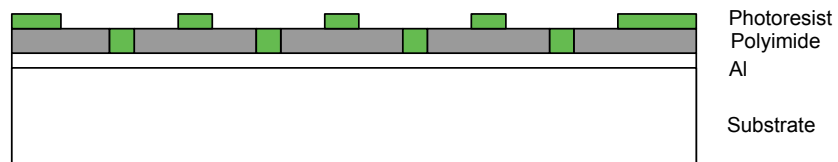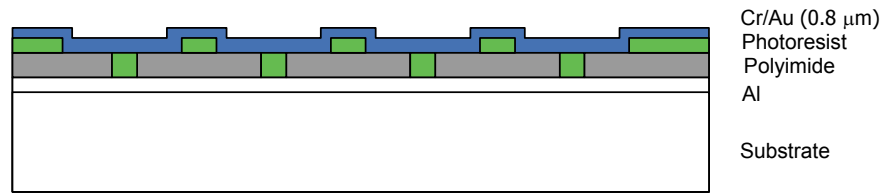Polyimide
Al

Substrate
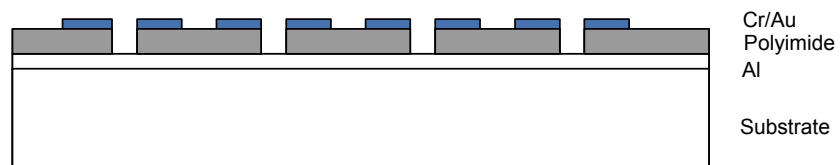
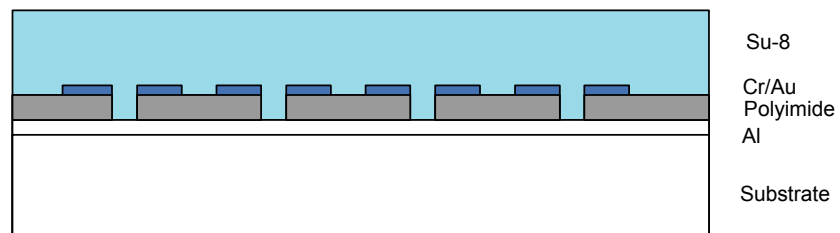Figure 5.23.   MEMS process sequence *(a-j)* developed for top layer of MEKA-5 array.
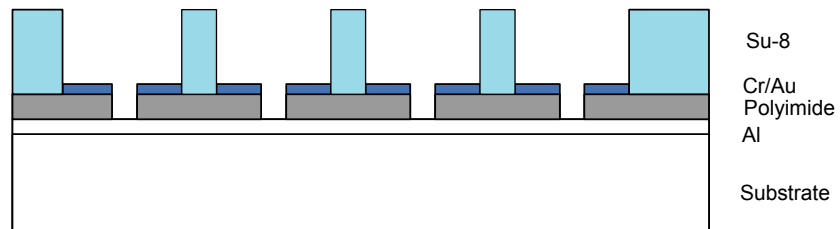
(f) Cr and Au are deposited (DC magnetron sputter)

Cr/Au (0.8 μm)
Photoresist
Polyimide
Al

Substrate

(g) Patterned and unmasked Cr/Au and photoresist is etched with acetone (lift-off)

Cr/Au
Polyimide
Al

Substrate

(h) Su-8 is deposited (spin cast)

Su-8

Cr/Au
Polyimide
Al

Substrate

(i) Patterned and unmasked Su-8 is etched with Su-8 developer

Su-8

Cr/Au
Polyimide
Al

Substrate

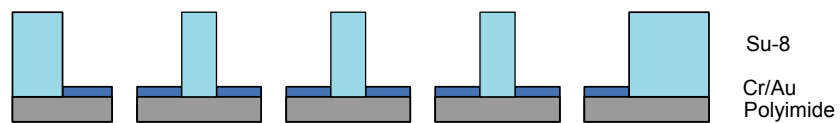*(j)* Aluminum etch with phosporic-nitric-acetic acid mixture

Su-8

Cr/Au
Polyimide
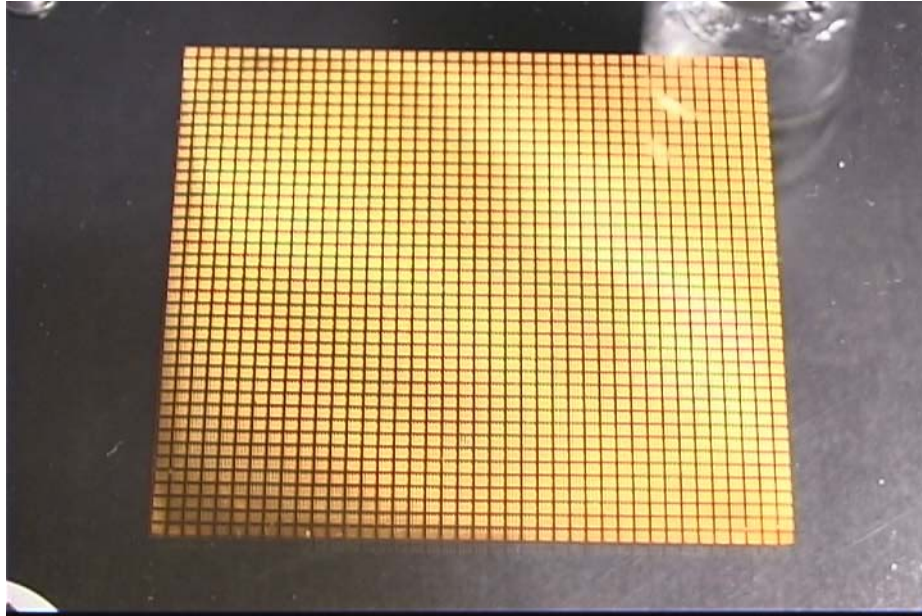
Figure 5.23.   (concluded)

Figure 5.24.   *(a)* Tile-scale view of electrodes sublayer fabricated via the process sequence in Fig. 5.23 for the 25,600-element MEKA-5 hydronautical-scale array. *(b)* Close-up view of the resulting unit-cell structure in the electrodes sublayer for the 25,600-element MEKA-5 hydronautical-scale array.

(a)

(b)
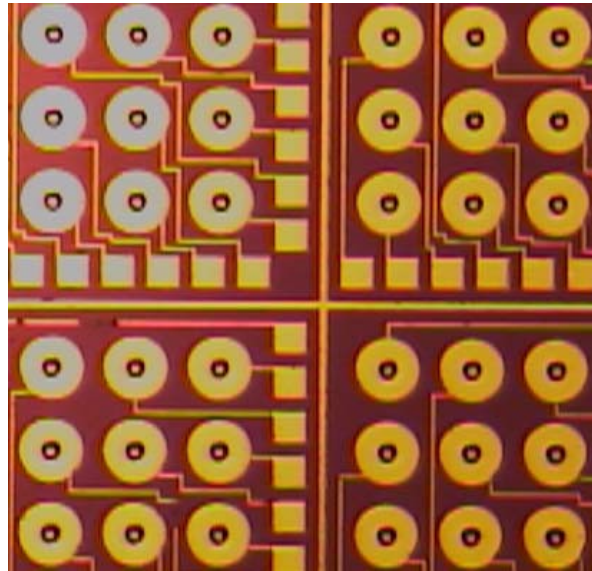
Figure 5.25.   Unit-cell-scale view of the electrodes sublayer for the 25,600-element MEKA-5 hydronautical-scale array, showing *(a)* a single unit cell, and *(b)* the bus structure separating adjacent unit cells.
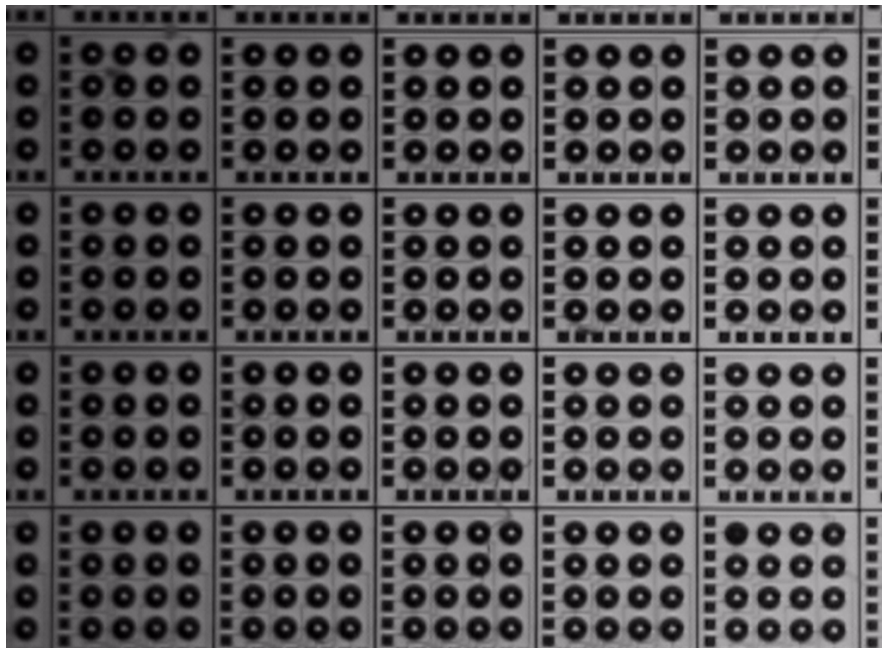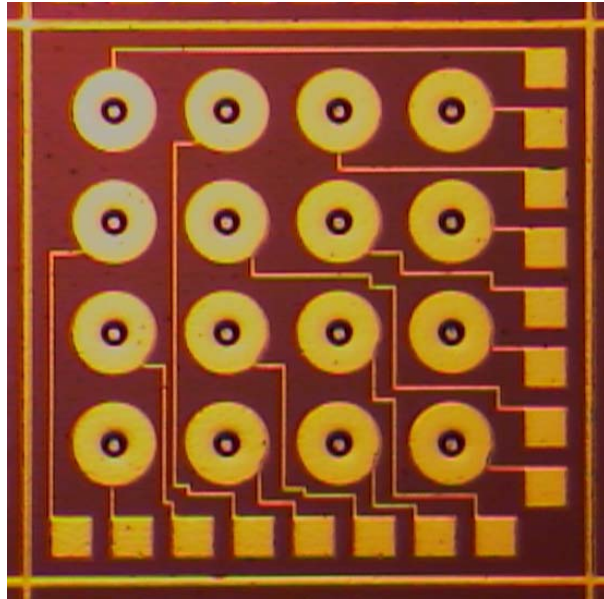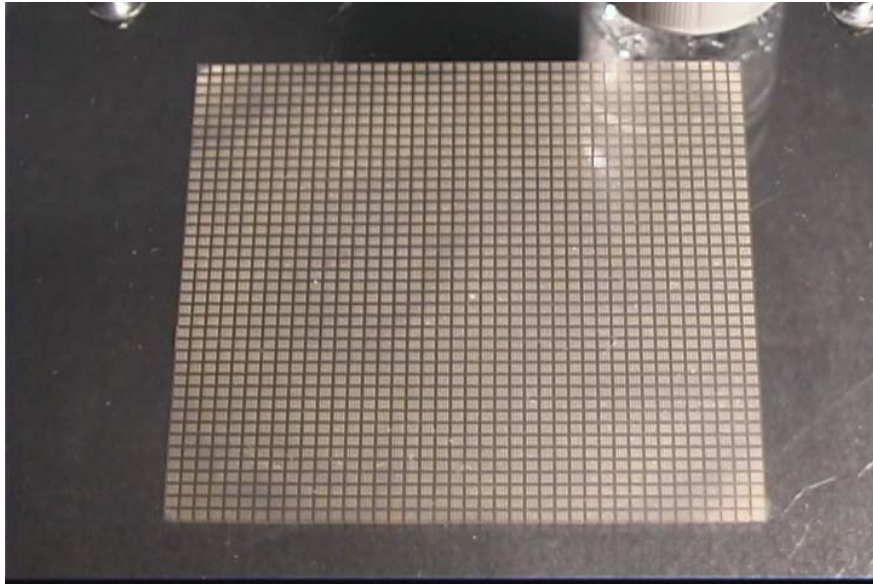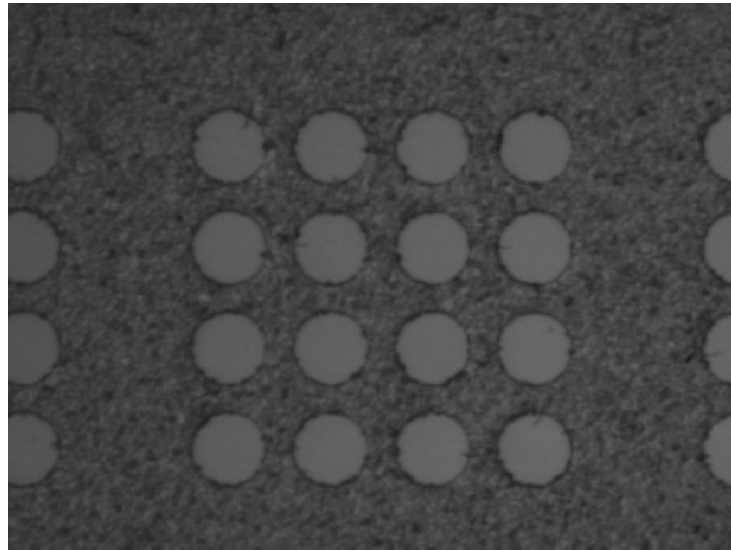
Figure 5.26.   *(a)* Tile-scale view of cavities sublayer fabricated in Su-8 via the process sequence in Fig. 5.23 for the 25,600-element MEKA-5 hydronautical-scale array. *(b)* Unit-cell-scale view of the cavities sublayer showing a single unit cell.
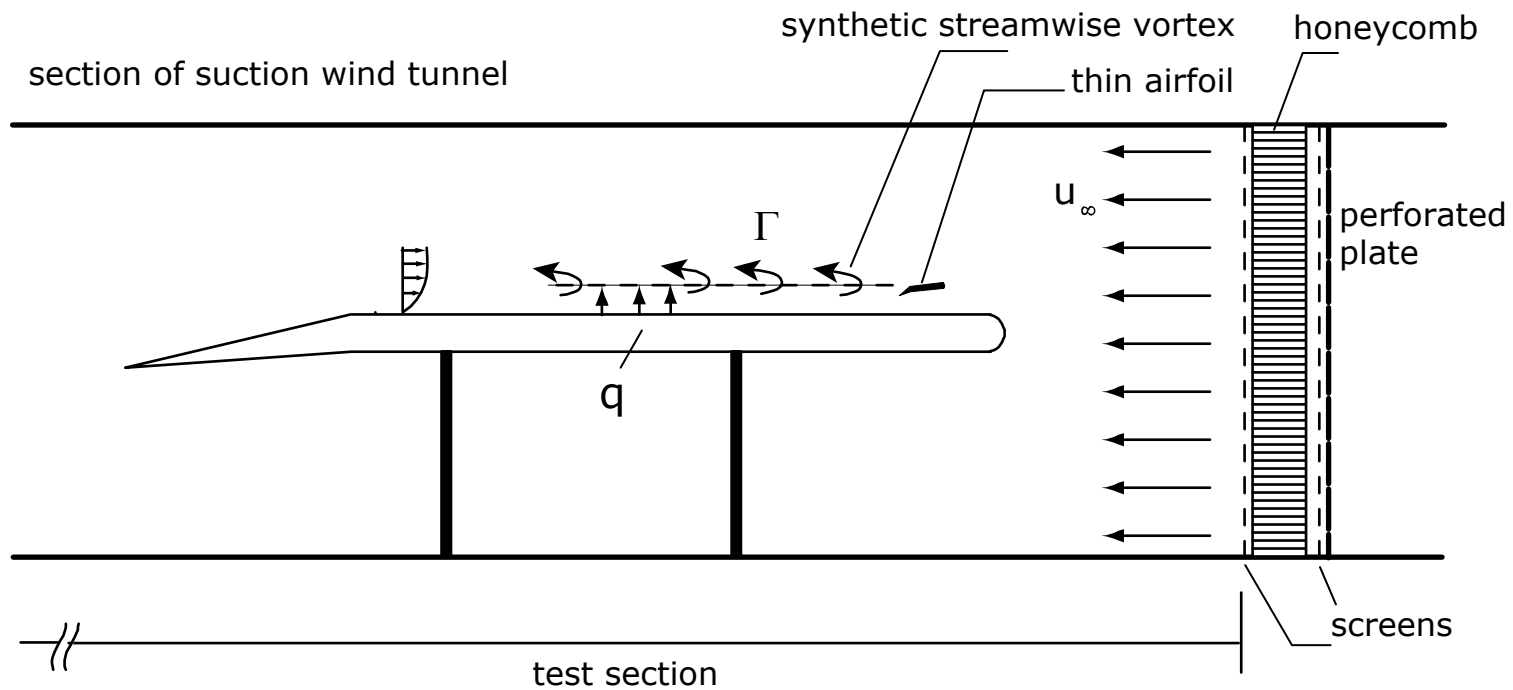
Figure 5.27.   Schematic showing basic layout of the large-scale wind tunnel experiments used to demonstrate synthetic streamwise vortex manipulation by volumetric pumping from a wall actuator, indicating wind tunnel, flat plate, and vortex generation by thin airfoil. Stereo PIV measurements were used to measure lateral displacement of the streamwise vortex by various levels of wall pumping.
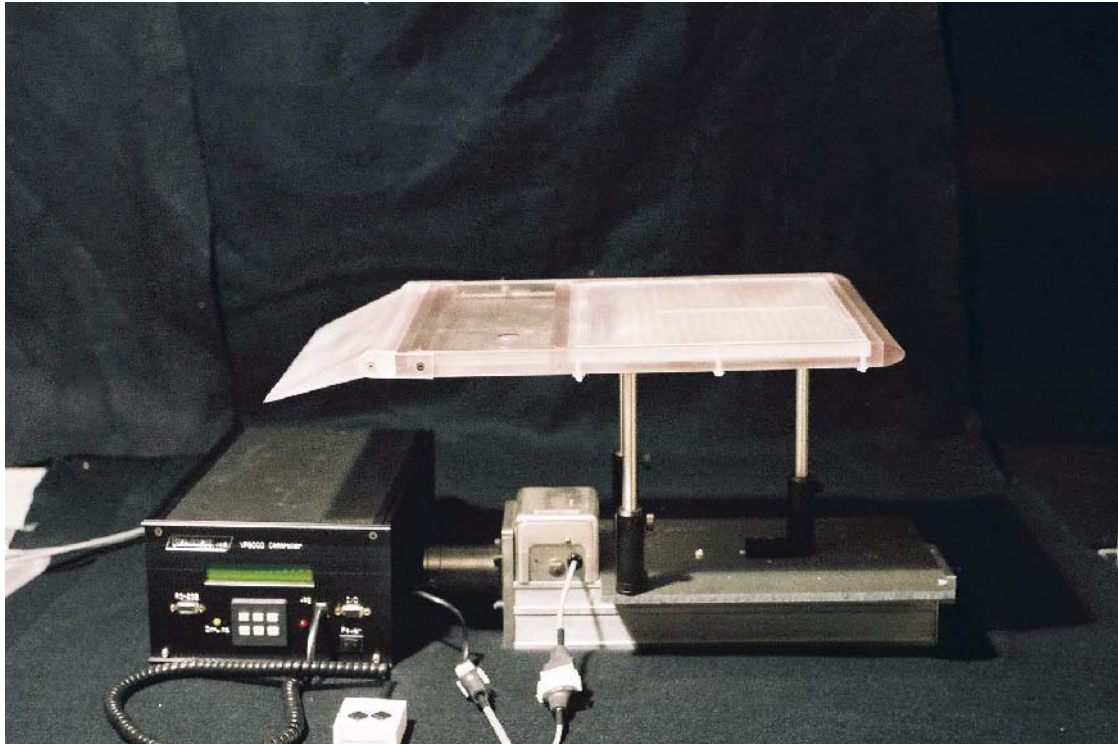
Figure 5.28.   Flat plate used for the present experiments on streamwise vortex manip-
ulation, showing rounded leading edge, trailing edge circulation flap, and digital
micropositioning stage.

(a)
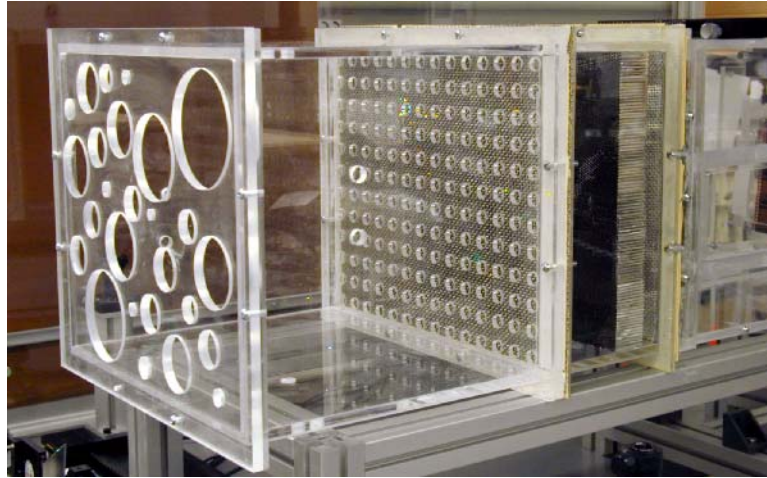
(b)
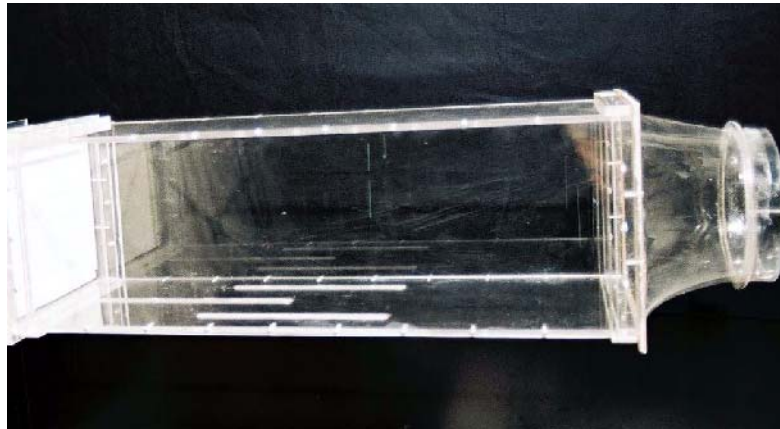
Figure 5.29.   Induced draft wind tunnel assembled for experiments on streamwise vortex manipulation, showing *(a)* the seeding section and the flow straightening section, and *(b)* the test section with slots to accomodate the positioning stage.
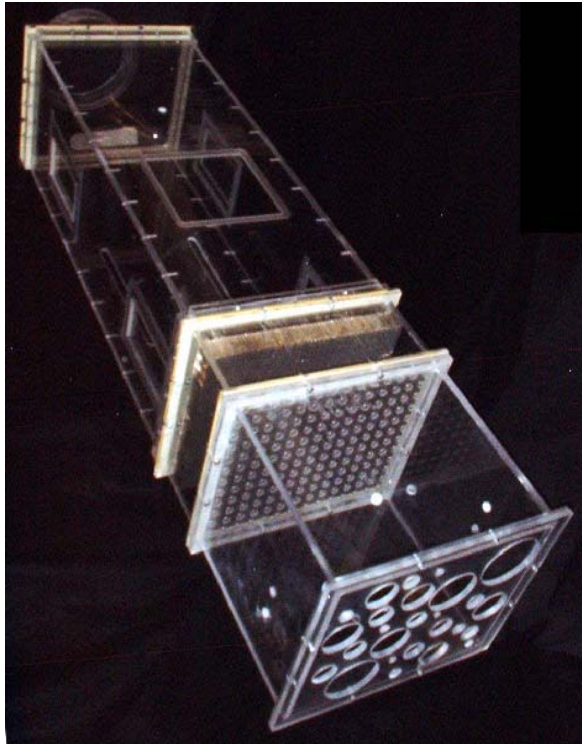
(a)   *(b)*

Figure 5.30.   Wind tunnel used for the experiments on streamwise vortex manipulation, showing stereo PIV access windows.

(a)

(b)
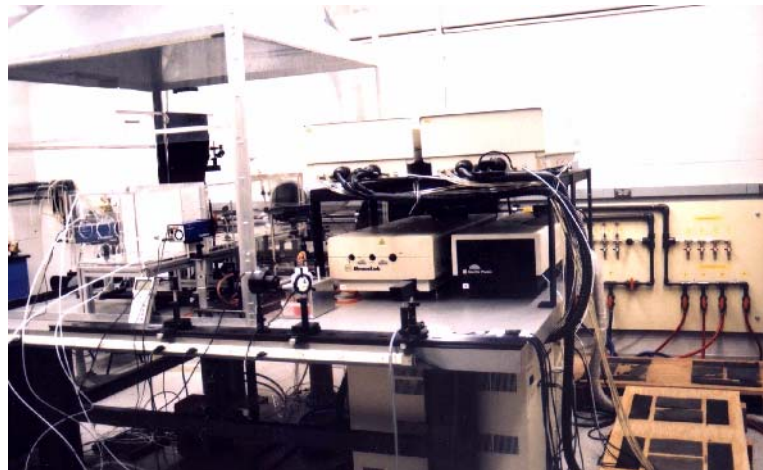
Figure 5.31.   Laboratory configuration for the stereo PIV measurements, showing *(a)* the master/slave computers for dual-plane stereo PIV capabililty, and *(b)* the four Nd:YAG lasers and the test section installed on the optical table.

(a)
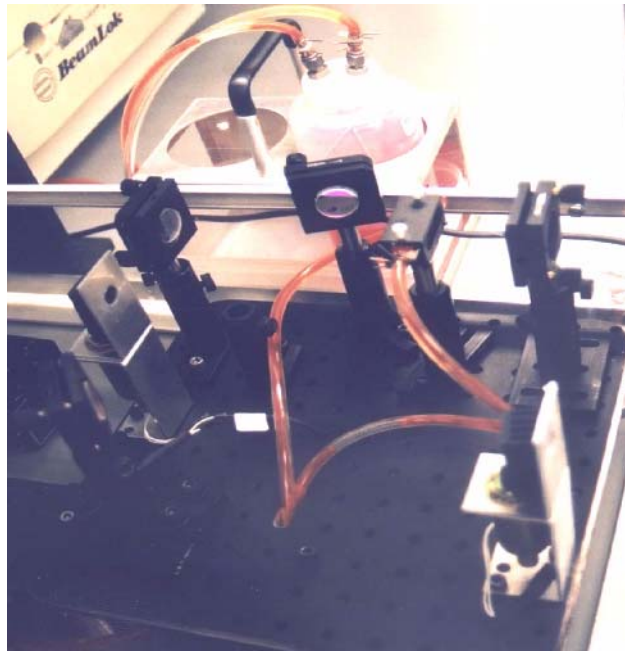
(b)
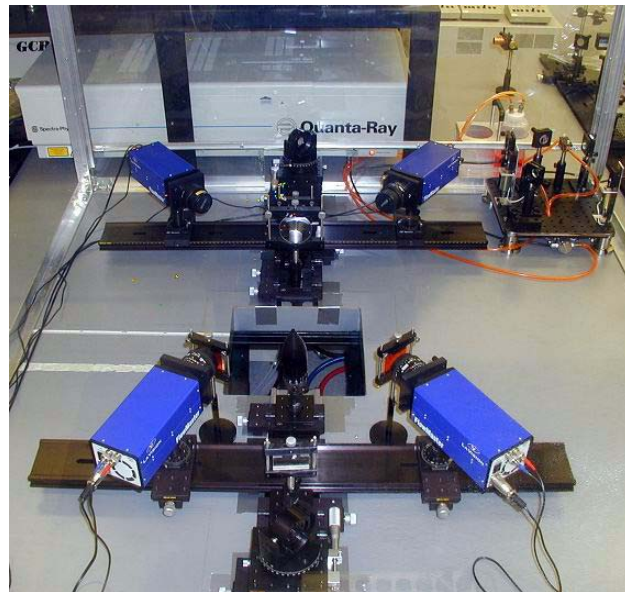
Figure 5.32.   Major components of the dual-plane stereo PIV system, showing *(a)* the dye laser, *(b)* the four PIV cameras, and *(c,d)* the wind tunnel test section with sheet-forming optics and dual-plane stereo PIV cameras.

(c)

(d)

Figure 5.32.   (concluded)

4 Nd:YAG Lasers

Dye Laser

623 nm

Master & Slave
Computer

532 nm

Wind Tunnel

4 PCO SensiCam Cameras
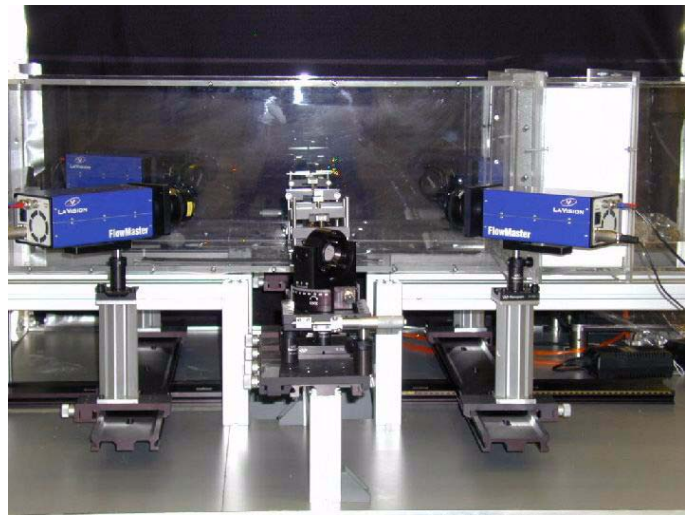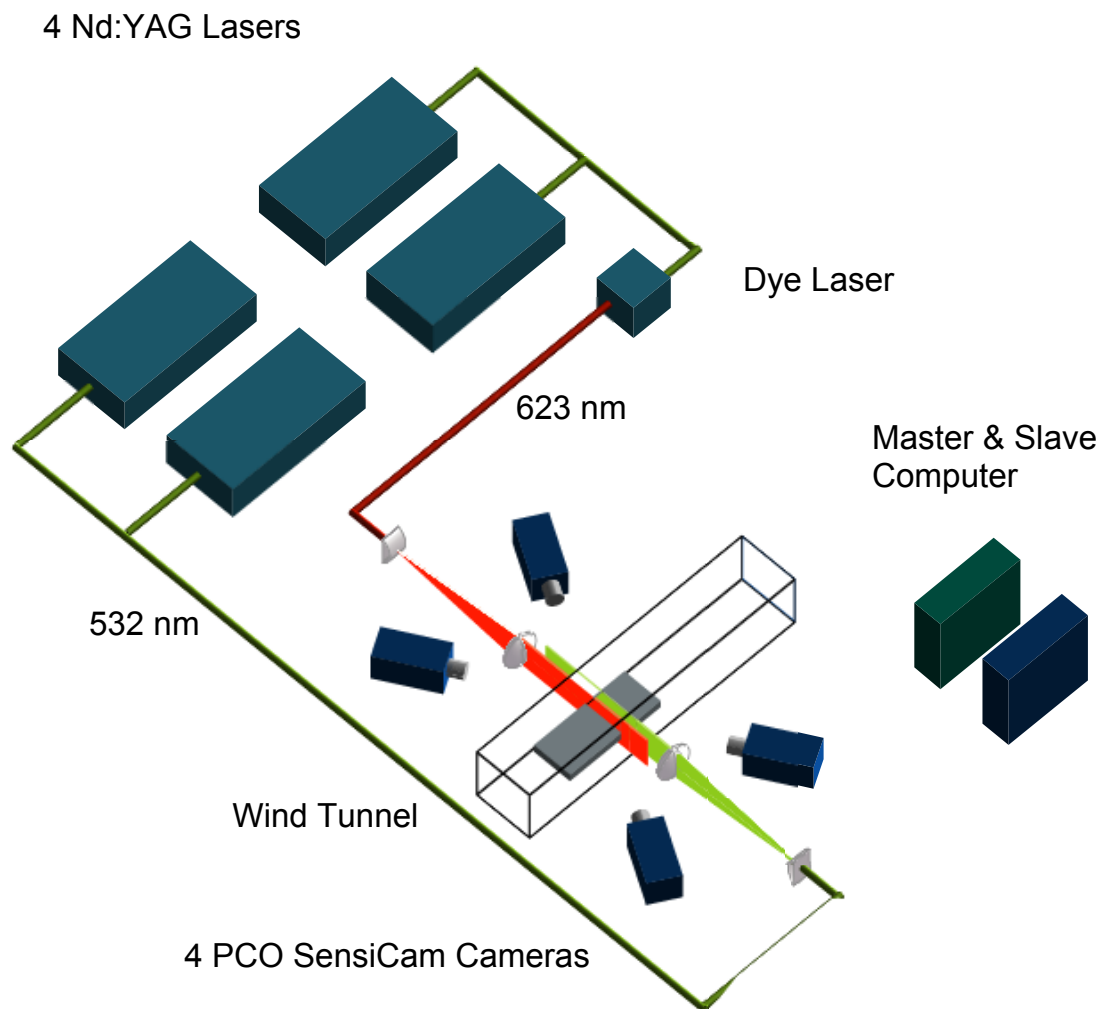
Figure 5.33.   Basic components and configuration for the two-color dual-plane stereo
PIV system.
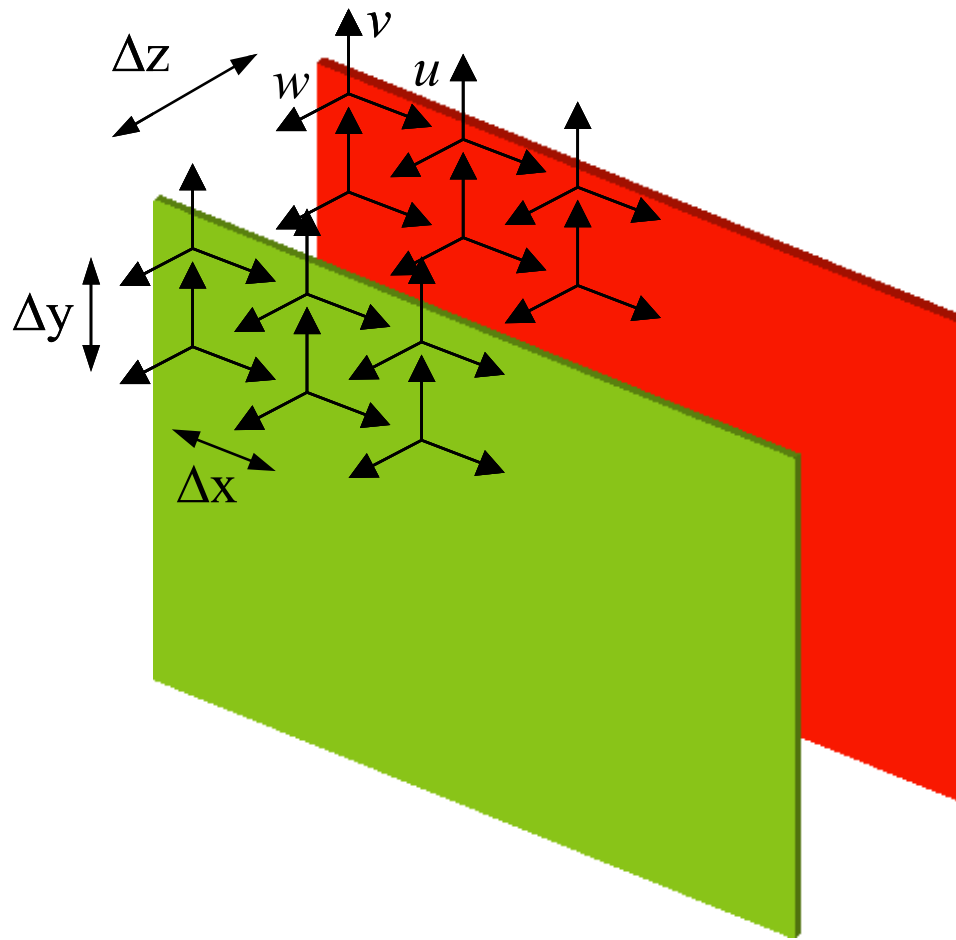
Figure 5.34. Two-color dual-plane stereo PIV concept for measurements of all nine components of the velocity gradient tensor field $\nabla \mathbf{u}(\mathbf{x},t)$, consisting of all three components of the vorticity vector field and all six components of the strain rate tensor field, via differentiation of the three-component velocity vector fields in two closely-spaced PIV measurement planes.

Laser 1 pulse — Camera 1, first frame

Laser 2 pulse — Camera 1, second frame

Laser 1 pulse — Camera 2, first frame

Laser 2 pulse — Camera 2, second frame
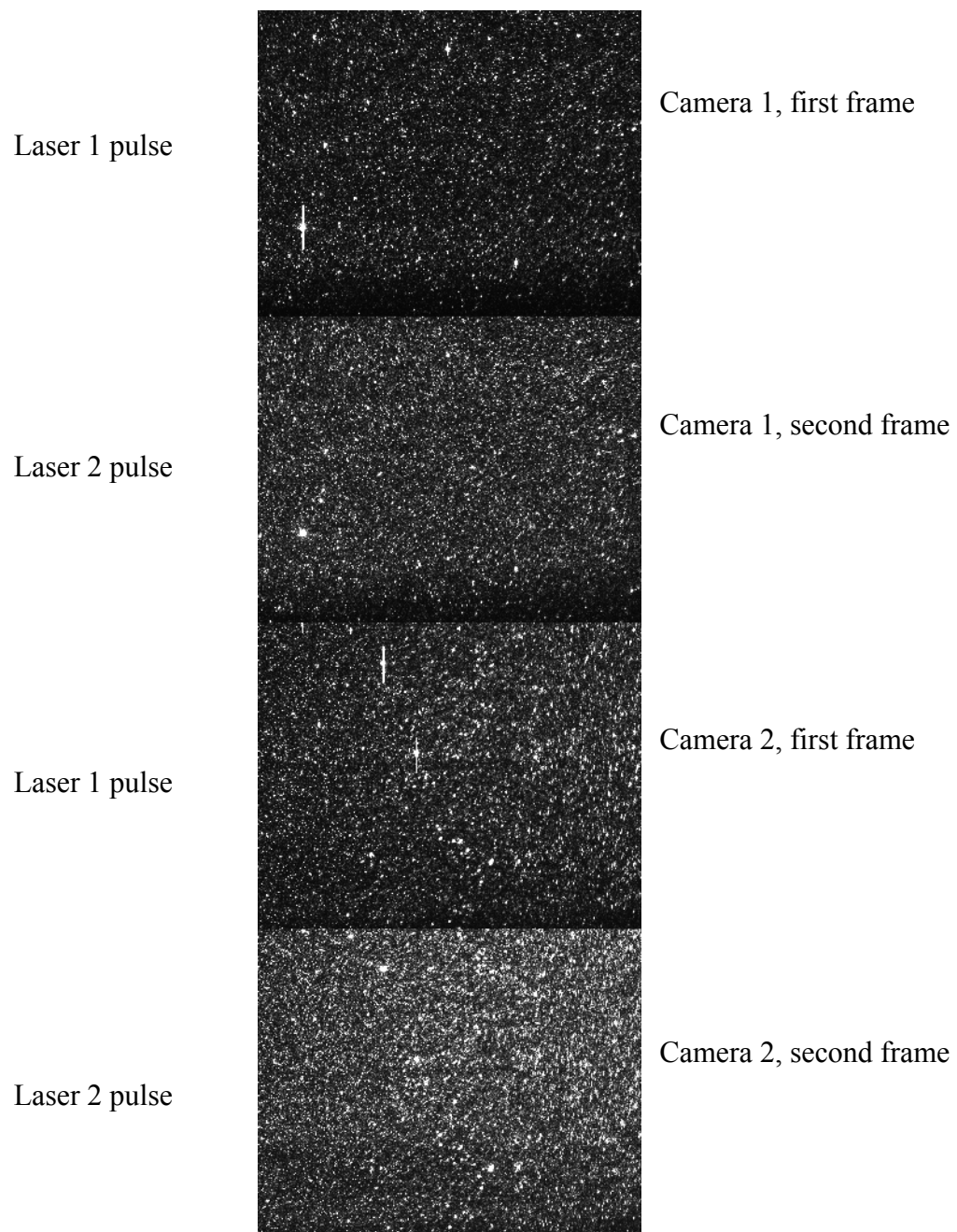
Figure 5.35.   Typical PIV images taken with stereo PIV sytem using double frame double exposure mode.

(a)
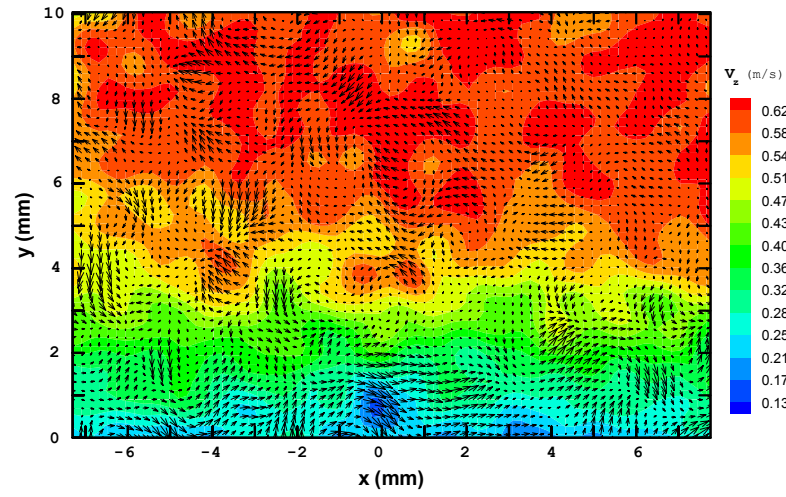
(b)

Figure 5.36.   Typical results from PIV measurements of *(a)* the instantaneous transverse velocity vector field and *(b)* the ensemble mean transverse velocity field, with color contours giving the streamwise velocity in the boundary layer.

Figure 5.37.   Measured mean streamwise velocity profiles along the wall-normal direction at several transverse locations.

(a)

(b)

Figure 5.38.   Typical results from PIV measurements of *(a)* the instantaneous transverse velocity vector field and *(b)* the ensemble mean transverse velocity field, with color contours giving the streamwise vorticity field in the boundary layer.

(a)

(b)

Figure 5.39.   Typical results from PIV measurements of *(a)* the instantaneous transverse velocity vector field and *(b)* the ensemble mean transverse velocity field, with color contours giving the shear strain field in the boundary layer.

(a)
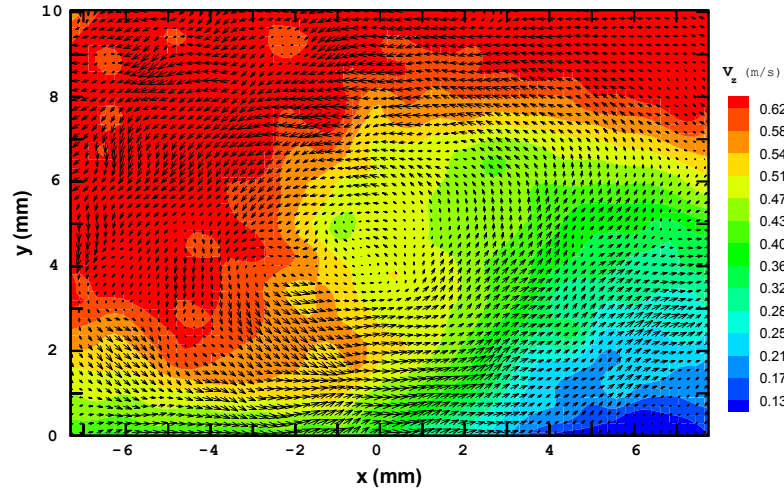
(b)
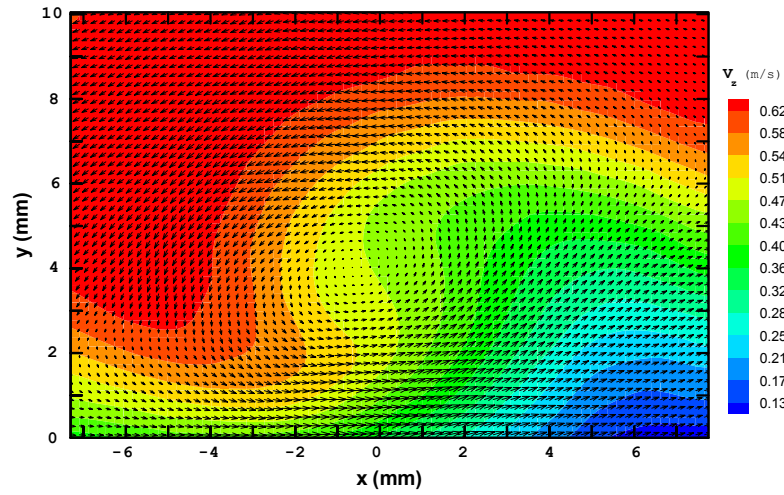
Figure 5.40.   Typical results from PIV measurements of *(a)* the instantaneous transverse velocity vector field and *(b)* the ensemble mean transverse velocity field, with color contours giving the streamwise velocity in the presence of a synthetic streamwise vortex in the boundary layer.
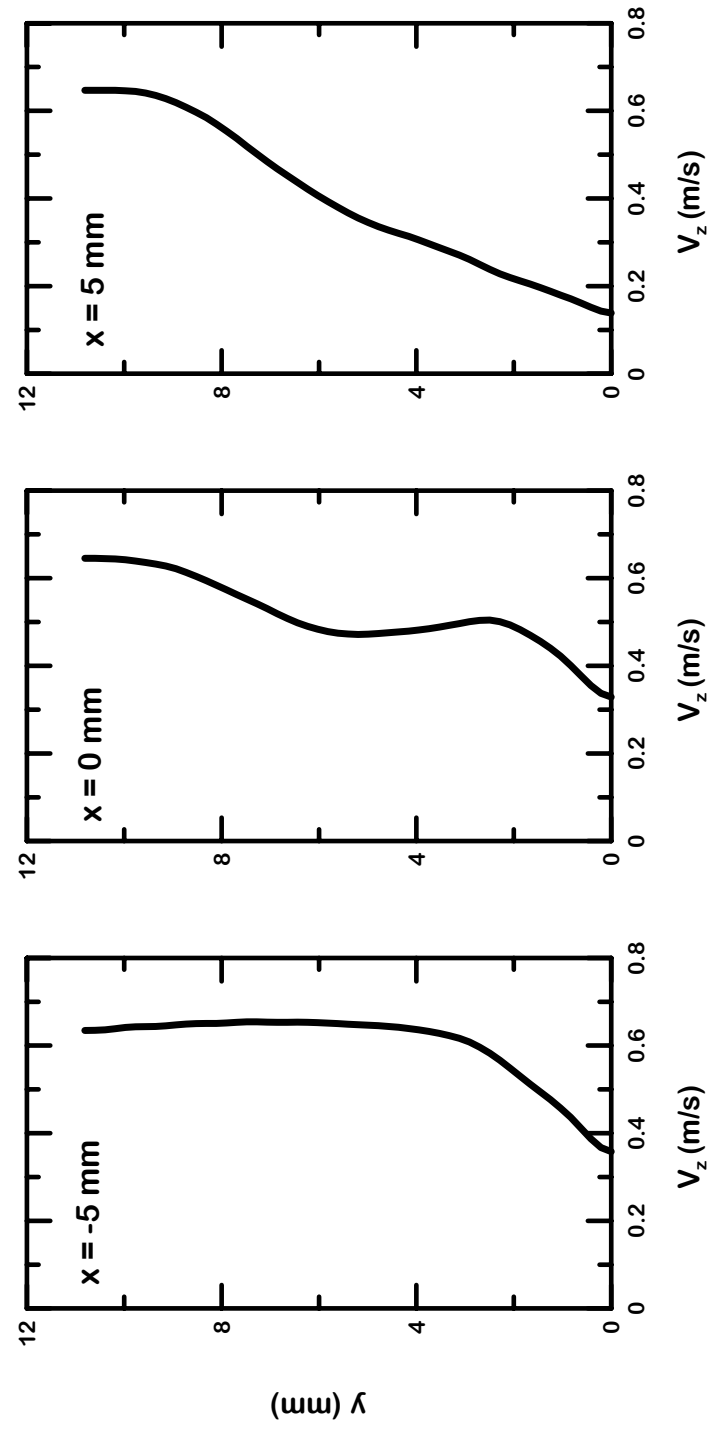
Figure 5.41. Measured mean streamwise velocity profiles along the wall-normal direction at several transverse locations for the same flow conditions as in Fig. 5.43.

(a)
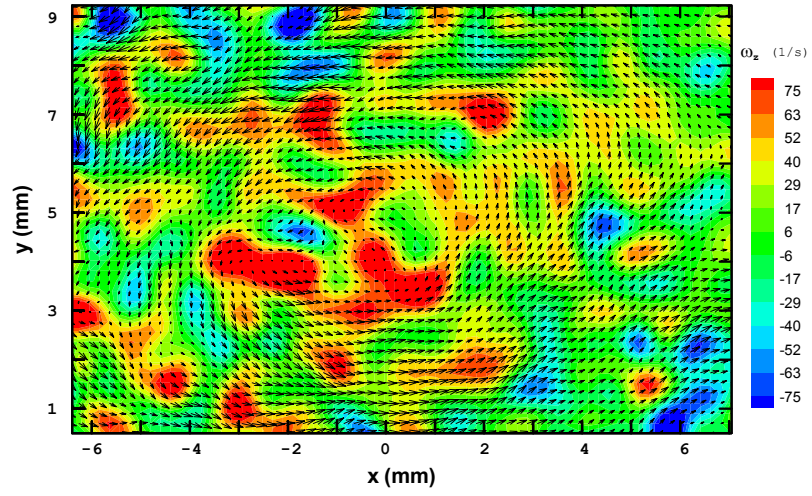
(b)
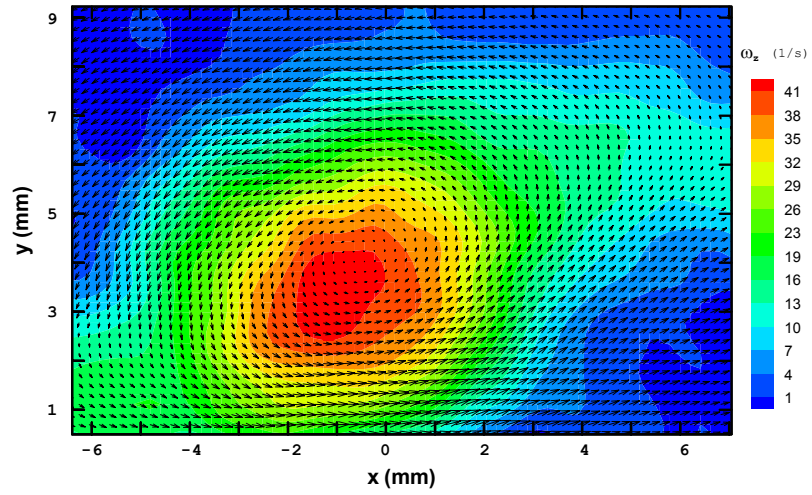
Figure 5.42.   Typical results from PIV measurements of *(a)* the instantaneous transverse velocity vector field and *(b)* the ensemble mean transverse velocity field, with color contours giving the streamwise vorticity field in the presence of a synthetic streamwise vortex in the boundary layer.

(a)
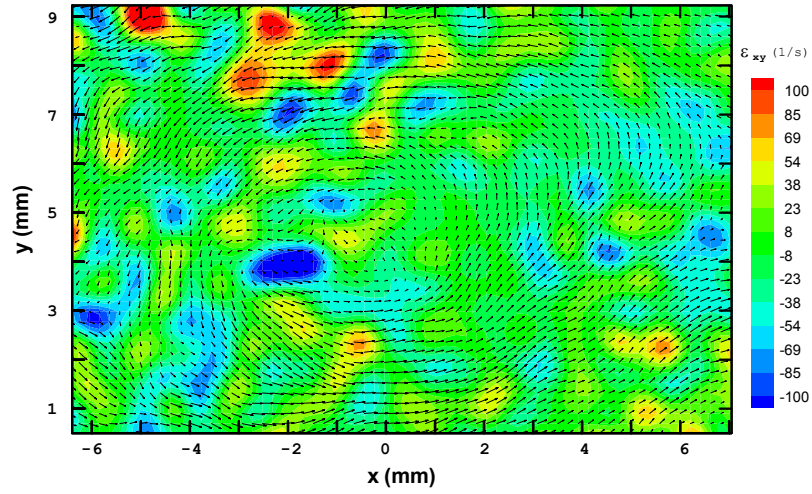
(b)
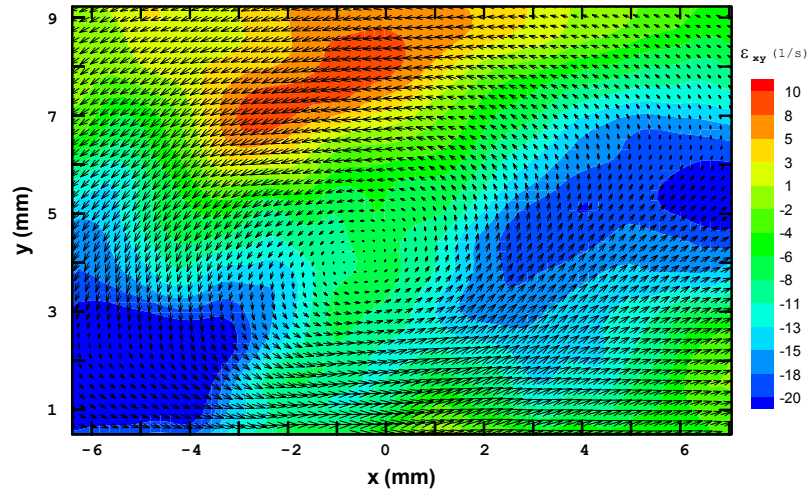
Figure 5.43.   Typical results from PIV measurements of *(a)* the instantaneous transverse velocity vector field and *(b)* the ensemble mean transverse velocity field, with color contours giving the shear strain field in the presence of a synthetic streamwise vortex in the boundary layer.
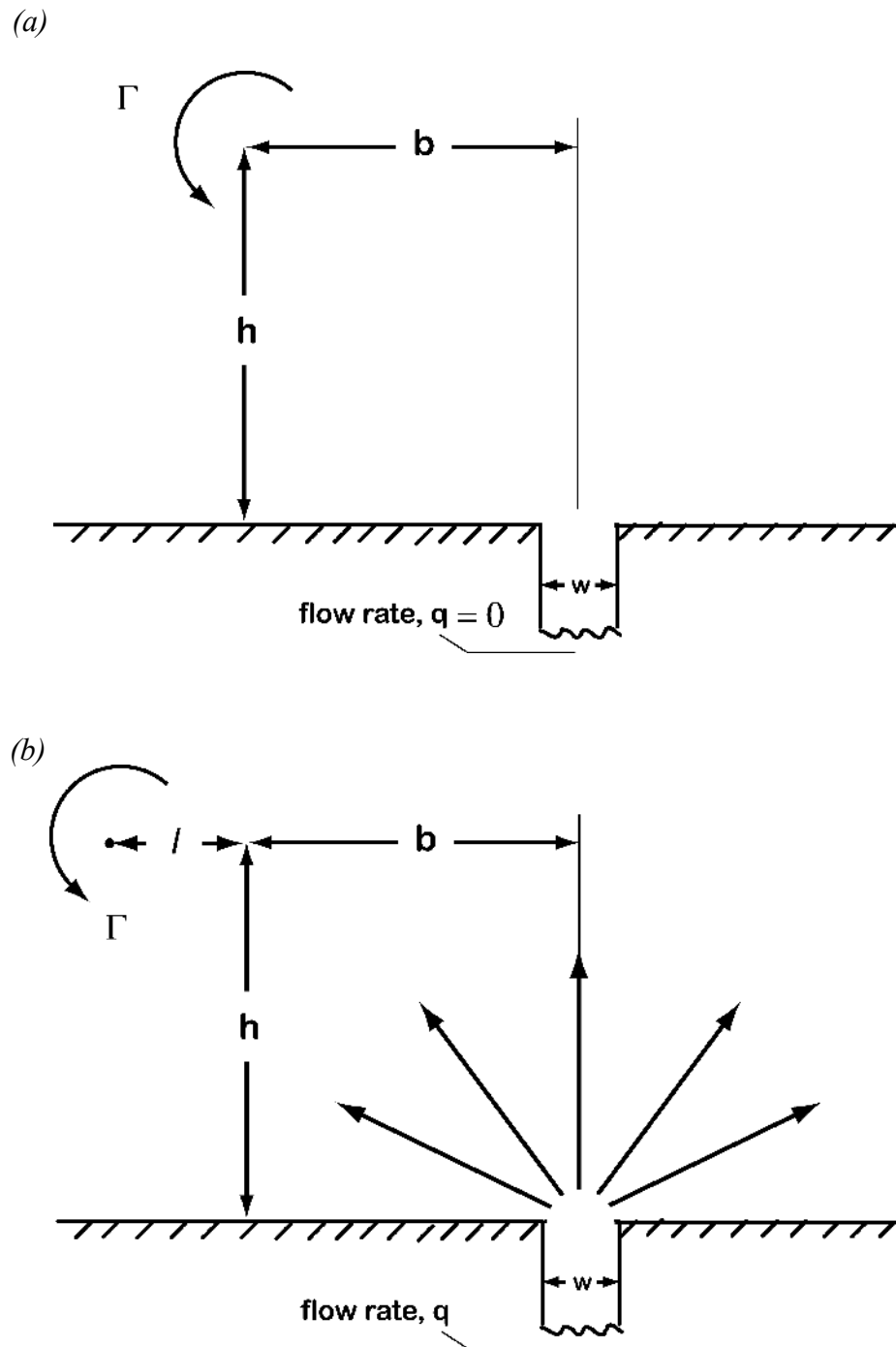
Figure 5.44.   Schematic indicating the synthetic streamwise vortex location with respect the center of the wall actuator under no wall actuation *(a)* and wall actuation *(b)*.
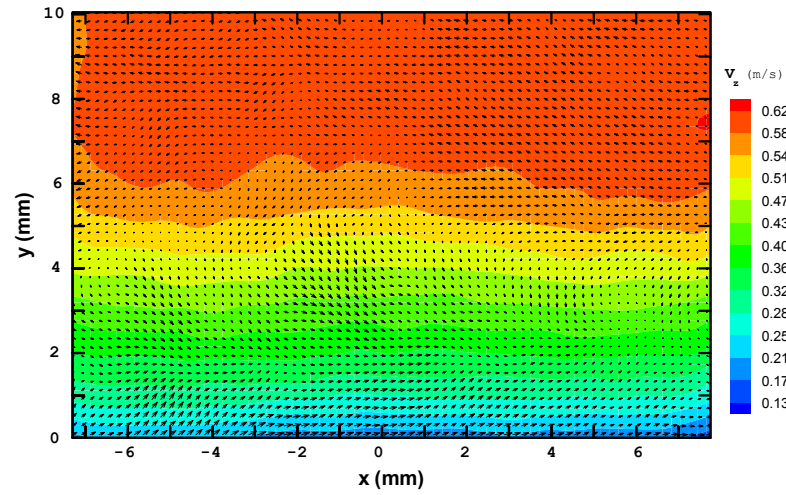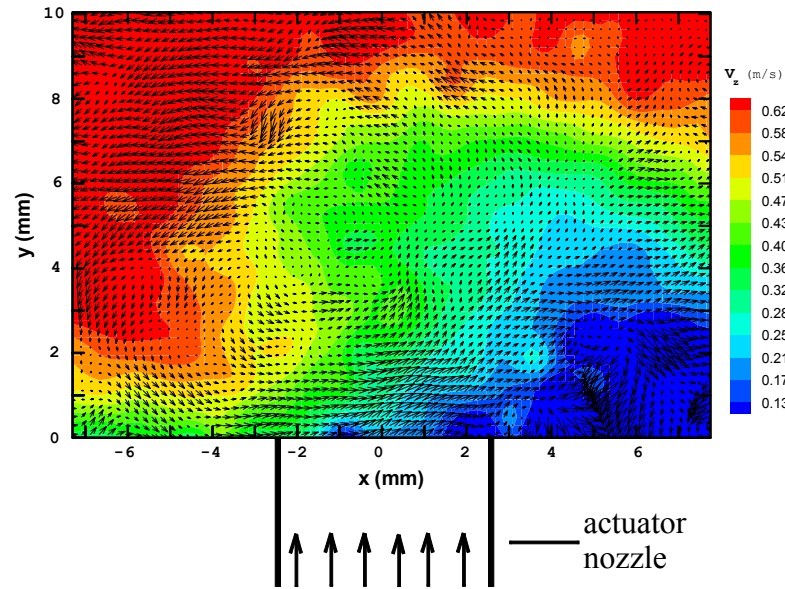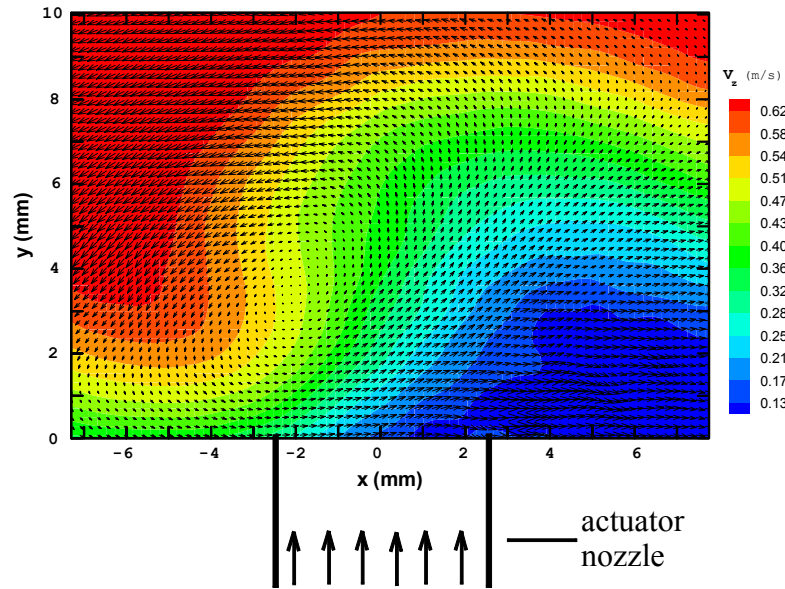
Figure 5.45. Typical results from PIV measurements of *(a)* the instantaneous transverse velocity vector field and *(b)* the ensemble mean transverse velocity field, with color contours giving the streamwise velocity in the presence of a synthetic streamwise vortex being displaced by wall actuation.
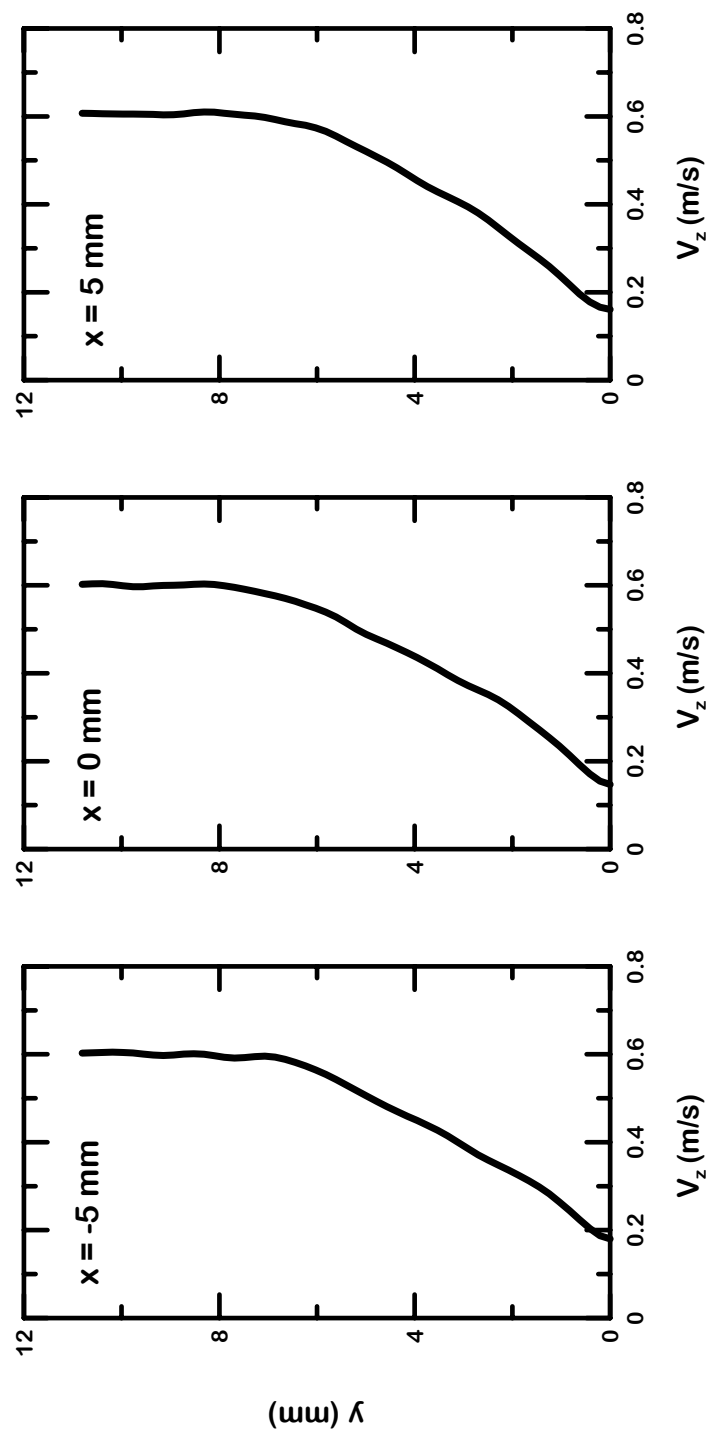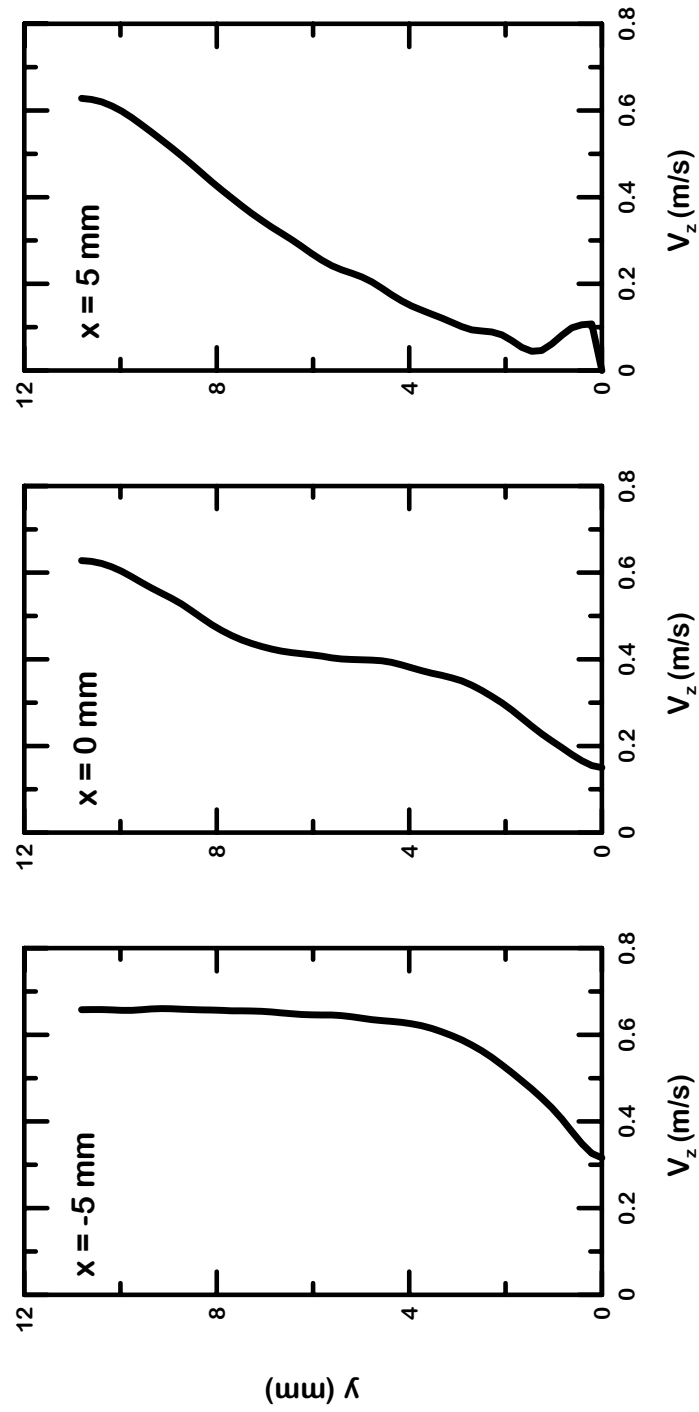
Figure 5.46. Measured mean streamwise velocity profiles along the wall-normal direction at several transverse locations for the same flow conditions as in Fig. 5.48.

(a)
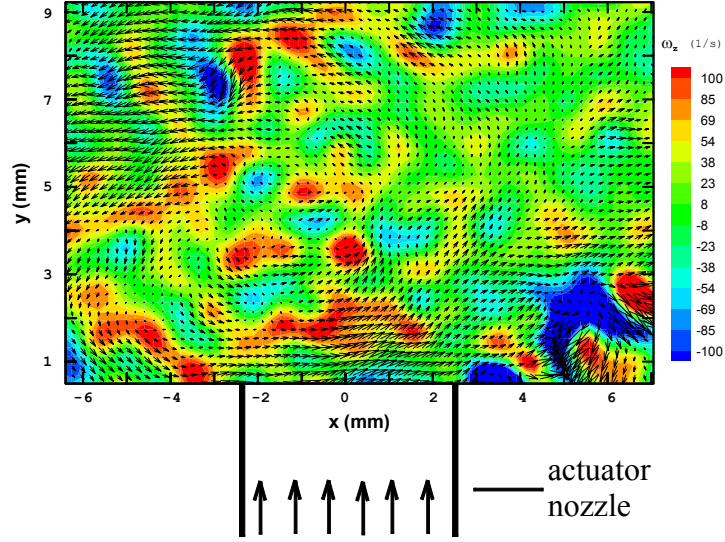
(b)
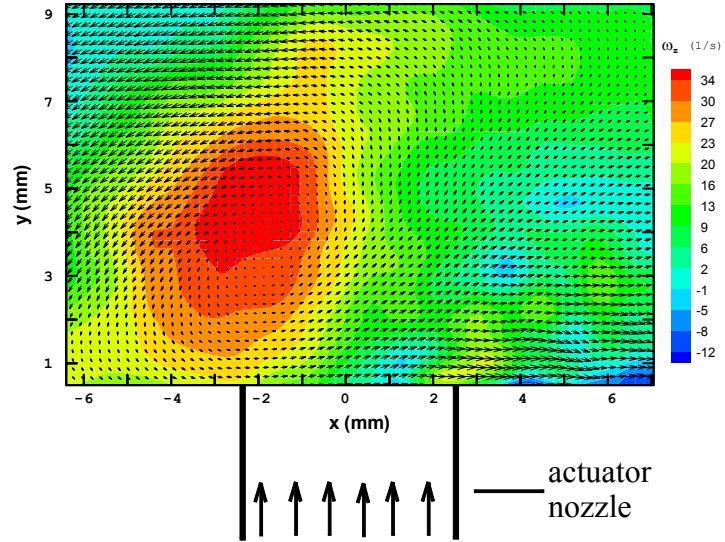
Figure 5.47.　　Typical results from PIV measurements of *(a)* the instantaneous transverse velocity vector field and *(b)* the ensemble mean transverse velocity field, with col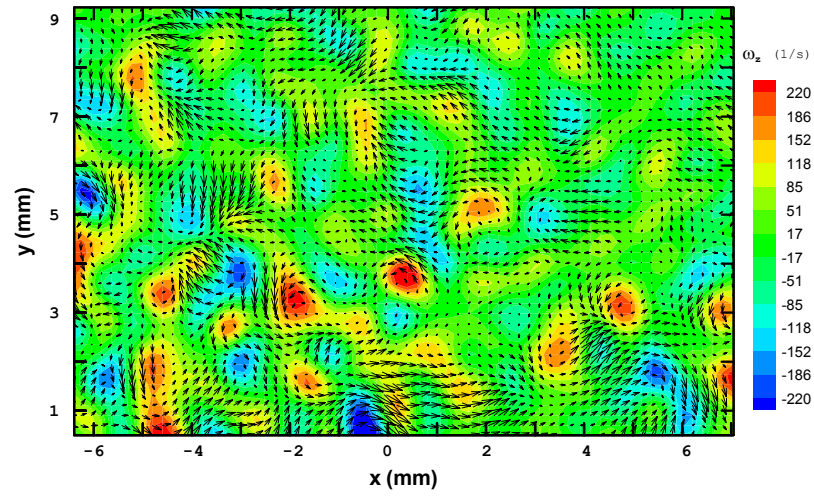or contours giving the streamwise vorticity field in the presence of a synthetic streamwise vortex being displaced by wall actuation.
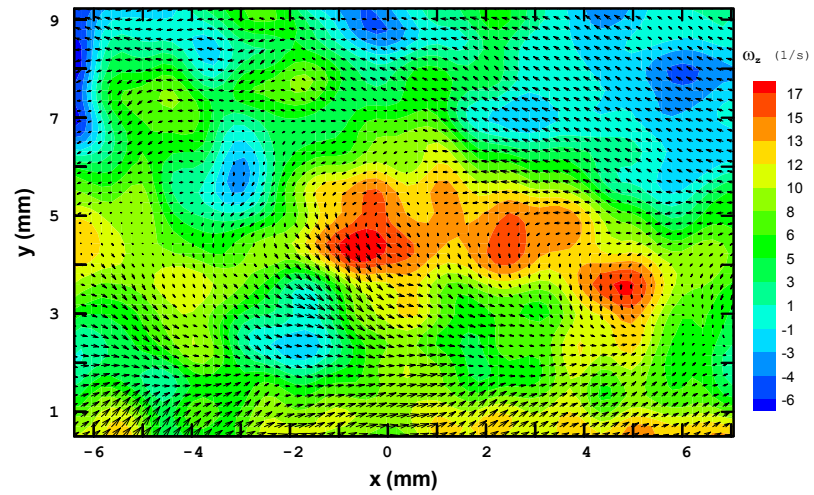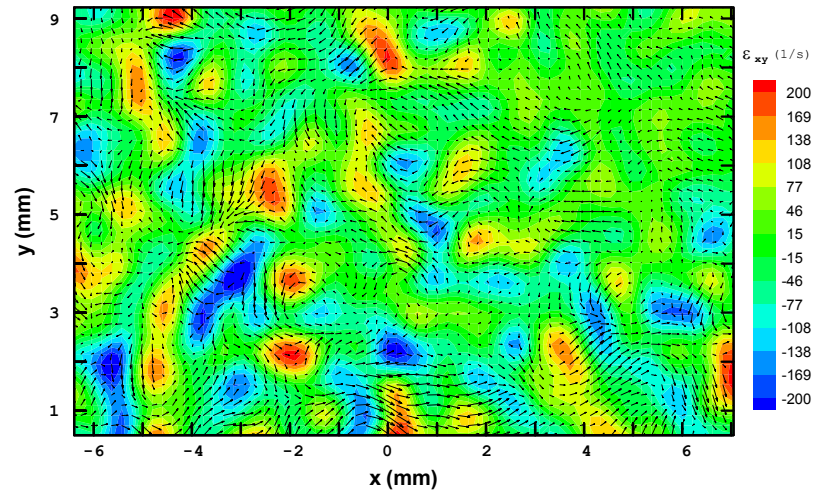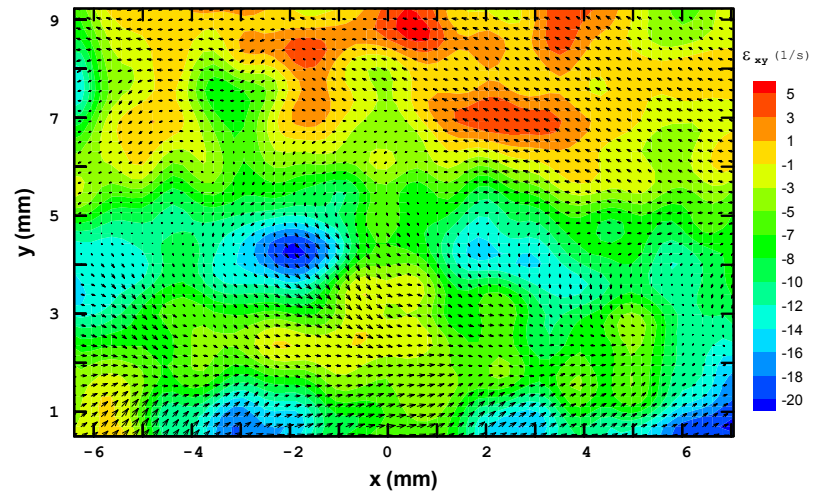
(a)
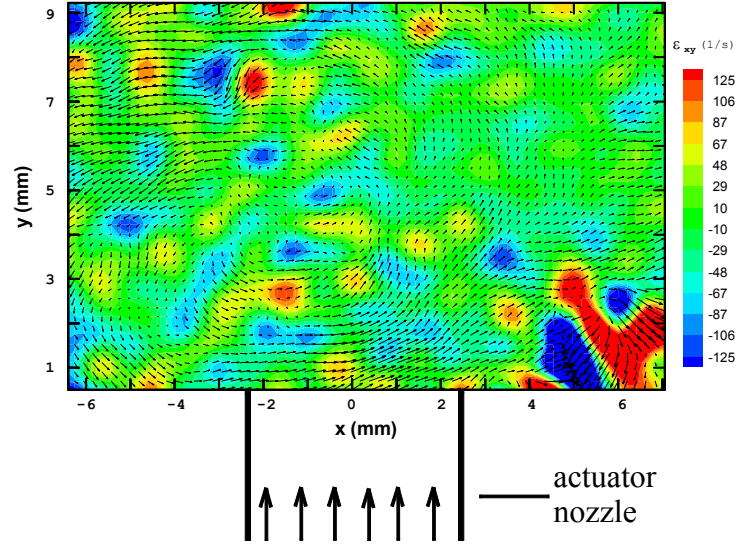
(b)
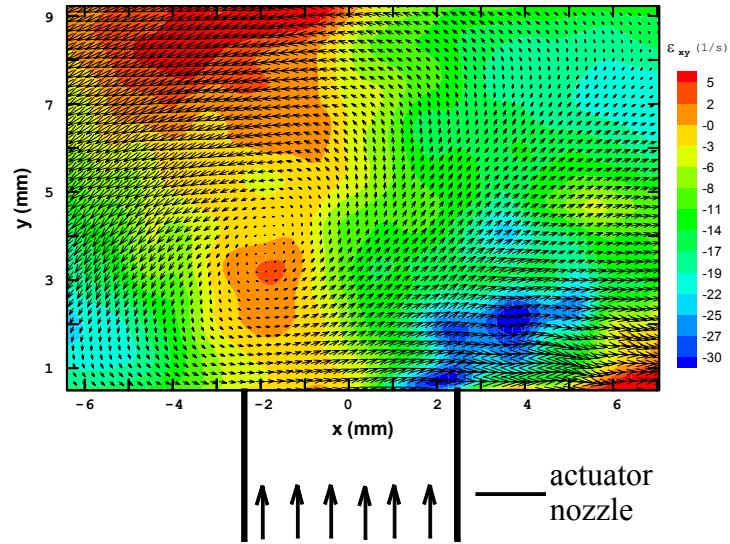
Figure 5.48.   Typical results from PIV measurements of *(a)* the instantaneous transverse velocity vector field and *(b)* the ensemble mean transverse velocity field, with color contours giving the shear strain field in the presence of a synthetic streamwise vortex being displaced by wall actuation.

138
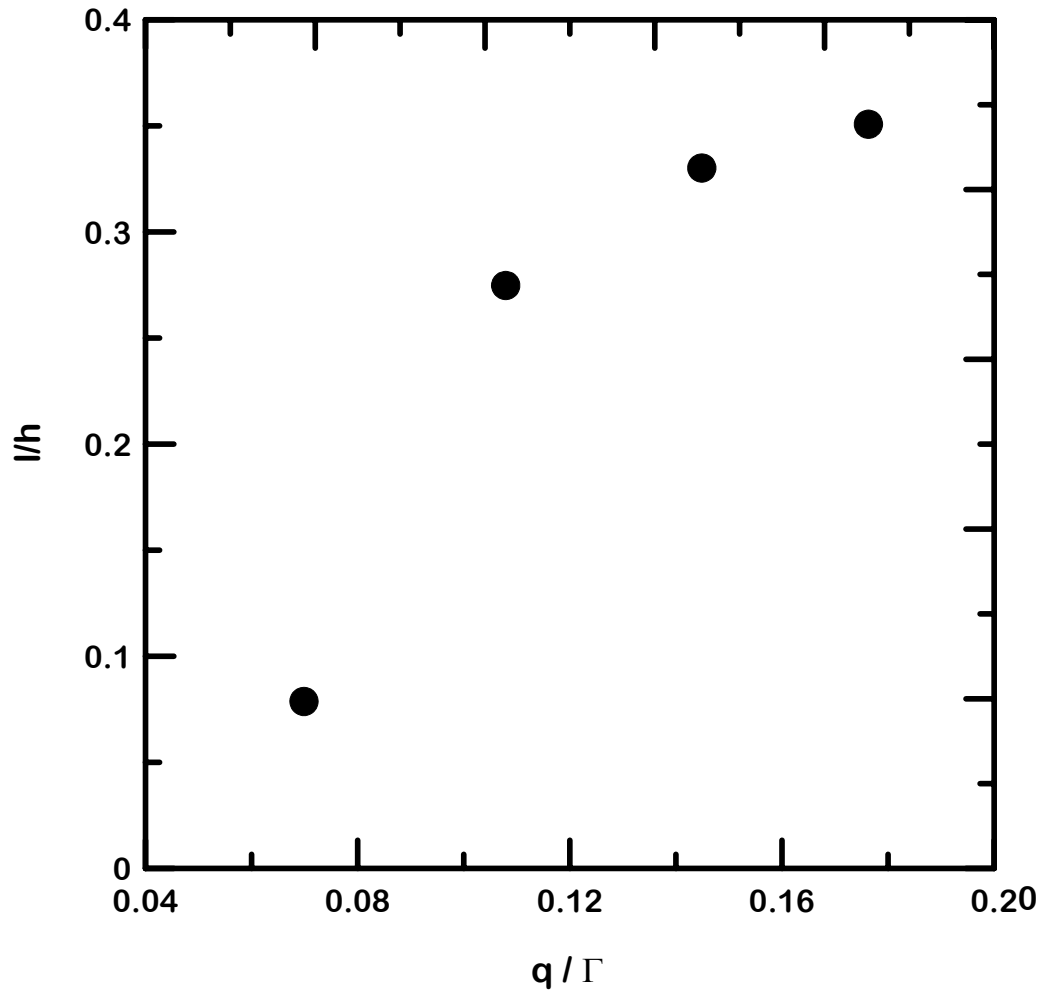
Figure 5.49. Measured relative lateral displacement *l/h* of the streamwise vortex as a function of the relative pumping strength *q*/Γ, following the notation in Fig. 5.47*b*. For sufficiently low pumping rates, these results from the PIV measurements demonstrate effective lateral displacements of streamwise vortices by wall actuation.

CHAPTER 6

WALL SHEAR STRESS SENSOR ARRAY

The system developed in this study for active sublayer control uses the signals from a set of microscale wall shear stress sensors, collocated at the unit-cell level with the microactuators described in §5, as inputs to the simple look-up table control logic described in §3. This chapter first reviews the current state-of-the-art in microscale wall shear stress sensors, and then summarizes the fundamental heat transfer considerations that are relevant to the design of such microscale sensors. It then outlines a simple sensor device based both on these fundamental considerations and on the results of previous studies reported in the literature. It also develops a MEMS process based on the current state-of-the-art from previous studies that in principle would permit fabrication of such collocated sensors in the top layer of the basic three-layer design and integration with signal processing electronics of the type noted in §3. The resulting predicted performance of this sensor array meets the requirements in Figs. 2.4-2.6 for active sublayer control on full-scale vehicles under realistic operating conditions.

6.1   Review of Micro Wall Shear Stress Sensors

Current state-of-the-art approaches for wall shear stress measurements with microscale devices are essentially all based on either "thermal sensors" or "floating element sensors". The former typically yields higher accuracies, however an equally important consideration for measurements under real vehicle operating conditions is that such thermal sensors can be built with significantly simpler structures that require no moving parts, and involve only cavities that are fully sealed and thus do not easily become contaminated or plugged.

Such thermal sensors can also be readily conformed to curved surfaces. However, thermal sensors rely on an indirect measurement that relates the shear stress to the heat transfer rate from the sensor to the fluid. As a consequence, one of the central design issues involves reducing the heat losses to the substrate, since this can seriously reduce the sensitivity of the sensor. Floating element sensors, on the other hand, allow for a direct measurement of the wall shear stress that does not rely on indirect correlations between the shear stress and some other physical process, such as heat transfer. Their main disadvantage is that the principle on which they operate fundamentally requires moving parts. As a result, such sensors are inherently more complex to fabricate than thermal sensors, and from an operational point of view they are more fragile and contain gaps and small crevices that can easily become contaminated or plugged in a realistic operating environment. Such sensors also cannot be as readily conformed to curved surfaces.

Several approaches for developing practical wall shear stress sensors based on these two approaches can be found in the literature (*e.g.,* Huang *et al* 1996, 1999; Kimura *et al* 1999; Liu *et al* 1999; Gad-el-Hak 1989, 1994, 1996; Löfdahl & Gad-el-Hak 1999; Padmanabhan *et al* 1995; Shajii *et al* 1992; Schmidt *et al* 1988; Breuer 2000). Of particular relevance for the present study, Schmidt *et al* (1988) fabricated a microscale floating element sensor with a sensing area of 500×500 μm^2 using MEMS techniques, and Huang *et al* (1996) developed a microscale thermal sensor to measure surface shear stresses, but noted that the resulting sensitivity of their sensors was less than desirable.

For wall shear stress measurements of the streamwise structures in the near-wall region of turbulent boundary layers, comparatively large arrays of such sensors would be needed to identify these structures. Arrays of thermal sensors would appear to be more appropriate for this purpose due to their inherently higher robustness, as noted above, and the fact that their inherent simplicity more readily permits fabrication in dense arrays collocated among actuators and processing electronics. Related to this, Kimura *et al* (1999) have successfully used MEMS processes to fabricate a microscale wall shear stress sensor array composed of 100 thermal sensors, and used this array under laboratory conditions to measure instantaneous spanwise distributions of surface shear stress. Their sensors were

spaced 300 μm apart, and the sensitive area – defined by the membrane where the polysilicon hot wire was located – measured 200×200 μm^2. Their array was arranged in four rows consisting of 25 sensors each, however these rows were spaced over 2.5 mm apart. The relatively large size of their sensors and the large separation between sensor rows limits their array to wall shear stress measurements at relatively low Reynolds numbers, for which the spacing between sublayer structures becomes accordingly large (as noted in §2). These authors have also reported that the frequency response of their sensors was significantly improved when an insulating vacuum cavity was used under the membrane on which the hot-film element is located, since this greatly reduces heat losses to the substrate material. However the bandwidth of their final sensor array remains unclear, since no direct evaluation of its time response was reported.

6.2 Heat Transfer Considerations

Thermal sensors take advantage the fact that the heat transfer from a sufficiently small heated surface depends only on the flow characteristics in the viscous region of the boundary layer. The heat generated electrically in the device is convectively transferred to the fluid and conductively transferred to the substrate, so that in general

$$Q = Q_f + Q_s, \tag{6.1}$$

where Q_s represents the heat transfer rate to the substrate and Q_f represents the heat transfer rate to the fluid. The latter includes both the *direct* heat transfer from the heated element to the fluid and the *indirect* heat transfer to the fluid from the heated portion of the substrate that is exposed to the fluid. The fundamental assumption relating heat transfer to shear stress is that the thermal boundary layer that develops over the device lies entirely within the linear region of the velocity profile. If, in addition, it is also assumed that the magnitude of velocity fluctuations increases linearly with distance from the wall, then it is possible to relate the fluctuating shear stress to the fluctuations in the heat transfer rate Q_f to the fluid. The resulting relation between the wall shear and the heat transfer rate, per unit width of the surface, is given by

$$Nu = 0.807(Pr(l^+)^2)^{1/3} \, , \tag{6.2}$$

where Nu is the Nusselt number, Pr is the Prandtl number and l^+ is the streamwise extent of the heated surface normalized by wall variables (Löfdahl & Gad-el-Hak 1999). The combination of Prl^+ is the Peclet number Pe based on the streamwise length of the film and the velocity at the edge of the thermal boundary layer. The Nusselt number in (6.2) is defined as

$$Nu = \frac{Q_f}{wk\Delta T}, \tag{6.3}$$

where Q_f is the total rate of heat transfer from the hot-film element to the fluid, w is the width of the film (normal to the flow direction), k is the coefficient of thermal conductivity of the fluid, and ΔT is the temperature difference between the film and the fluid.

Since part of the heat transferred from the film goes directly into the fluid, while the rest first heats the membrane and the substrate which, in turn, are subsequently cooled by the flow, there are two observations that are central to the design of such sensors. First, the heat transfer to the membrane on which the hot-film element is located participates in the process by producing an increase in the effective value of l^+. Second, as the fraction of the total heat transferred to the membrane and the substrate increases, the overall sensitivity of the resulting device to changes in the wall shear decreases.

In order to address these points, it is useful to rewrite (6.1) in a more explicit form for the case where the film is heated electrically. When the hot-film element is operated in constant-temperature mode, the temperature difference ΔT is fixed and the heat transfer rate is proportional to the square of the voltage across the film. The input power P to the sensor can then be written as

$$P = \Delta T[h(\tau_w) + k], \tag{6.4}$$

where the power dissipated by conduction to the substrate is represented by a generalized conduction coefficient k, and the power dissipated by convection to the fluid is represented by a generalized convection coefficient $h(\tau_w)$. The heat transfer rate to the fluid is related to the wall shear stress τ_w according to the relation $\tau_w \sim Q_T^3$ (Löfdahl & Gad-el-

Hak 1999). Thus $h(\tau_w)$ in (6.4) can be written as

$$h(\tau_w) = A(\tau_w)^{1/3} ,$$ (6.5)

where the factor A is given by Liu *et al* (1999) as

$$A = 0.807 A_e \left(\frac{C_p \rho k^2}{L \mu} \right)^{1/3} ,$$ (6.6)

with A_e denoting the effective area of the thermal element, C_p the heat capacity of the fluid, k the thermal conductivity of the fluid, L the streamwise length of the resistive heating element, and μ the fluid viscosity.

From (6.4)-(6.6), for any fixed input power P, as k increases relative to $A(\tau_w)^{1/3}$ the sensitivity to the wall shear stress will be reduced. Thus effective shear stress sensor design must minimize the heat loss to the substrate. For this reason, the proposed sensor design improves the frequency response and sensitivity of thermal sensors by using a vacuum cavity underneath the thermal sensor, as has been reported by Breuer (2000), Huang *et al* (1996), and Kimura *et al* (1999). Since the thin film element is then separated from the substrate by a vacuum cavity and a membrane, the heat will still be conducted from the film to the membrane and then from the membrane to the substrate. Following Huang *et al* (1999), these two conductive heat transfer terms can be written as

$$q_s = \frac{k_s A (T - T_i)}{d_s} ,$$ (6.7)

and

$$q_i = \frac{2 k_i d_i L (T_i - T_o)}{L_c} ,$$ (6.8)

where q_s and q_i represent, respectively, the conductive heat transfer rate from the sensor to the membrane and from the membrane to the substrate, while k_i and k_s are the thermal conductivities of, respectively, the membrane and the sensor element, and L_c is the half length of the cavity. The factor of 2 in (6.8) is a result of the bidirectionality of the heat transfer across the membrane. An initial estimate for k can be obtained by evaluating (6.8) and assuming an ideal membrane with no q_s-losses. For a more detailed evaluation of k, detailed heat transfer simulations such as those of Huang *et al* (1999) would be required.

The voltage V applied across the film element can then be obtained from (6.4) as

$$V^2 = \Delta T \cdot R \cdot (h(\tau_w) + k) . \tag{6.9}$$

The sensitivity of the device is obtained by differentiating (6.9) with respect to the wall shear stress τ_w, giving

$$\frac{1}{V}\frac{\partial V}{\partial \tau_w} = \frac{1}{2}\frac{\partial h}{\partial \tau_w}\frac{\Delta T}{P} . \tag{6.10}$$

As is apparent from this result, the sensitivity is increased by maximizing the overheat temperature while minimizing the dissipated power. This can be done in practice by using small thermal masses and materials with a high temperature coefficient of resistivity (TCR), namely a high temperature difference for a given resistive overheat setting.

6.3 Sensor Array Design

The thermal losses to the substrate can be minimized as demonstrated by Huang *et al* (1996) by mounting the sensor on a thin membrane over a vacuum-backed cavity. In this case, the leakage path is restricted to conduction along the surface of the membrane, as indicated by Breuer (2000). This is demonstrated by assuming a sensor with a characteristic radius R_i mounted on a membrane of radius R_o. The temperature distribution can then be modeled as a function of radial distance r across the circular membrane. The sensor element is approximated as maintaining a temperature T_i near the center of the membrane, at $r \leq R_i$, and the temperature decreases radially to the ambient value T_o at the edge of the membrane, at $r = R_o$. The resulting one-dimensional temperature distribution across the membrane is then simply

$$T(r) = T_i + (T_o - T_i)\frac{\ln(r/R_i)}{\ln(R_o/R_i)} . \tag{6.11}$$

This is shown in Fig. 6.3 for a typical membrane with $R_o = 50$ μm.

From (6.11), the total heat flux q from the periphery of the membrane, at $r = R_o$, as shown

by Breuer (2000), is

$$q \propto \frac{kt(T_o - T_i)}{\ln(R_o/R_i)},$$ (6.12)

where t is the membrane thickness. To minimize these losses for a given temperature difference and a fixed sensor size, the factor $t/\ln(R_o/R_i)$ in (6.12) needs to be made as small as possible. On the other hand, this is limited by the fact that the membrane also serves a structural function as one of the vacuum cavity walls, and thus needs sufficient strength to support the pressure difference. This pressure difference must be balanced, as indicated by Breuer (2000), by the biaxial stress s in the membrane, given by

$$s^2(s - s_o) = \frac{Mp^2R_o{}^2}{24t^2},$$ (6.13)

where M and s_o are the biaxial elastic modulus and residual membrane stress, and p is the external pressure, which in most cases would be one atmosphere. For an assumed maximum upper biaxial stress value at which the membrane will fail, the ratio of R_o/t will be constant. A calculation was carried out for the proposed silicon nitride membrane, giving $R_o/t = 1169$. Most of the values for constants involved in this calculation were obtained from the MEMS Material Database at the MEMS Clearinghouse web site, where material property data are collected from publications in the principal MEMS journals and IEEE conferences, and from the SUMMiT Material Properties from Sandia National Laboratories. In general the material properties from these two sources agreed reasonably well. Note that different processes used to deposit the membrane material yield different material properties. For the present sensors, the silicon nitride membrane was designed to be deposited using LPCVD (low pressure chemical vapor deposition) which yields lower internal stresses. Although there remains some uncertainty about some of the values used here, the fundamental sensor design and the resulting performance assessments presented below should remain valid.

In addition to effects of the membrane radius-to-thickness ratio R_o/t, a further consideration is the maximum deflection which the membrane will experience when a given pressure difference exists across the membrane due to the cavity vacuum. The pressure

difference across the membrane due to the cavity vacuum will produce a deflection of the membrane, as shown in Fig. 6.4*a*. Several studies have analyzed the load-deflection behavior of such a membrane (*e.g.,* Tabata *et al* 1989). The approach usually taken uses an energy-minimization technique that includes the contribution of intrinsic tensile stress and provides a simple closed-form solution. For the general case of an square membrane, the resulting load-deflection relationship is given by Tabata *et al* (1989) as

$$P = \frac{C_1 \sigma t h}{a^2} + \frac{C_2 E t h^3}{a^4} , \qquad (6.14)$$

where P is the pressure difference across the membrane, E is Young's modulus of the membrane material, σ is the internal film stress, t is the membrane thickness, and h the resulting membrane deflection. In (6.14), C_1 and C_2 are energy minimization constants and are functions of the membrane shape. For the present membrane, C_1 and C_2 are approximately 3.04 and 1.83, respectively. Figure 6.4*b* shows the resulting pressure P across the membrane required to produce a given deflection h for membrane thicknesses t of 1 μm, 0.5 μm and 0.2 μm. The results show that for a membrane thicknesses below $t \approx 0.5 \mu m$, the membrane will deflect at least 0.6 μm when a pressure difference of one atmosphere is applied across it. As a design constraint, a deflection below 0.6 μm is desired, since this requires the vacuum cavity height to be no larger than 2 μm, and thereby allows comparatively simple MEMS photolithographic fabrication methods to be used, of the same type as were used to fabricate the top layer of the MEKA-5 hydronautical array in §5. A schematic of the final shear stress sensor design is shown in Fig. 6.5.

From the discussion above of the temperature distribution across the membrane, the membrane stresses, and the membrane deflection, as well as the maximum sensor spacing in Fig. 6.1, a membrane thickness of 0.5 μm and radius of 50 μm has been chosen for thermal sensor array design. Sensors of this size could be readily integrated as suggested in Fig. 3.2 in the unit cells on MEKA-5 hydronautical array. To estimate the performance of these sensors, the resistance of the heating element R can be approximately related to temperature T by a linear relation $R = R_o[1 + \alpha(T - T_o)]$, as noted by Huang *et al* (1996). Here R_o and T_o are the average resistance and temperature at a reference condition (usually

ambient values) and α is the TCR (temperature coefficient of resistivity) of the hot-film material. An important parameter governing the operation of such hot-film sensor is the overheat ratio, defined as $\alpha_T = (T - T_o)/T_o$, where T is the temperature of the heated element. In operation, it is more practical to use a resistive overheat ratio, defined by $\alpha_R = (R - R_o)/R_o$, where R is the resistance of the heated element. The relationship between the two overheat ratios is simply $\alpha_R = \alpha T_o \alpha_T$. A resistive overheat ratio of α_R ≈ 0.2 is typical (*e.g.,* Huang *et al* 1995; Liu *et al* 1999). In general, as this value increases the power consumption of the sensor also increases and the frequency response is decreased. On the other hand, if α_R is too low then this will decrease the steady-state sensitivity of the device. Here a value of 0.2 will be used to permit comparisons with the results from these previous studies. Equation (6.9) can then be written as a function of α_R, α, and R_o to give

$$V^2 = (A\tau^{1/3} + B)\frac{\alpha_R}{\alpha}(\alpha_R + 1)R_o \ .$$ (6.15)

where A was defined in (6.6) and B is given by q_i in (6.8) divided by ΔT.

6.4 Sensor Performance

The considerations above suggest graphing the ratio of input power to temperature difference against $\tau_w^{1/3}$ as shown in Fig. 6.6a. The slope of this line then gives the value of A, and the intercept with the y axis gives the value of B. The resulting values of these parameters for the sensor design developed above are summarized in Table 6.1 and compared to those obtained by Liu *et al* (1999).

In general, larger values of A correspond to sensors with higher sensitivity. Note that the theoretical value for A obtained here is clearly higher than the values obtained experimentally by Liu *et al* (1999) when they operated their sensor design in constant current (CC) and constant voltage (CV) modes, but is about a factor of two lower than their result for constant temperature (CT) operation. It is important to note that the actual value of A for any particular sensor depends on a number of factors beyond the design of the sensor

itself, such as the performance characteristics of amplifiers and filters used together with the sensor in the circuit. As a result, the present calculated theoretical sensor values are only approximations for the actual performance that would be achieved experimentally. If the proposed sensor array were fabricated and tested, it is likely that it would show performance parameters A and B closer to those found experimentally by Liu *et al* (1999).

As regards the value for B, which represents the heat lost by conduction to the membrane and to the substrate, lower values of B provide greater sensitivity of the sensor. The present theoretical results for the proposed sensor design are about a factor of three smaller than the experimental values obtained by Liu *et al* for their sensor design, consistent with the fact that the losses from conduction to the membrane were not included in the present calculations. As noted above, it is furthermore likely that additional factors that impact the overall performance of the sensor in a complete circuit will also drive the actual value for B closer to that measured by Liu *et al* for their sensor design. Nevertheless, the results in Fig. 6.6*a* suggest that the proposed sensor design, which is sized to permit integration in the present MEKA-5 array, would have performance characteristics comparable to current state-of-the-art wall shear stress sensors.

Figure 6.6*b* shows the theoretical predictions for the measured voltage across the sensor element for various values of the wall shear stress τ_w. Direct comparisons of this result with values for other sensor designs reported in the literature are not possible without consideration of the characteristics of the circuit in which the sensor is operated, as noted above. Figure 6.6*c* shows the resulting theoretical sensitivity of the proposed sensor design from (6.10). The relatively low sensitivity at large values of the wall shear stress could be improved by using a differential amplifier in the associated circuit. It is likely that the overall sensitivity of this sensor, when accounting for the circuit in which it is used, will be similar to the results obtained by Huang *et al* (1999), since the present values for A and B are in the same range as the values they obtained.

6.5 Sensor Fabrication Process

The major process steps by which the proposed microscale wall shear stress sensor can be fabricated are shown in Fig. 6.7, and have been largely adapted from Huang *et al* (1999), although some changes were made to the geometry and type of electrodes used. One key modification is made in Step 3 in Fig. 6.7, where a 1.3 μm layer of thick silicon dioxide is grown using thermal oxidation at 1050 C for 4 hours, as described by Wolf & Tauber (1986). During the oxidation process, the silicon/silicon dioxide interface moves further into the substrate. At the end of this oxidation process, 44% of the 1.3 μm oxide thickness will be contributed by oxidation below the original silicon surface, as reported by Wolf and Tauber. Breuer *et al* (2000) describe a somewhat different approach for fabricating the cavity itself that provides an alternative to the high vacuum nitride deposition step shown in Fig. 6.7. Their process requires a "device" wafer that is patterned with the cavity hole, and a second "capping" wafer that is coated with the silicon nitride membrane. The two wafers are then bonded together and the capping wafer is etched until only the device wafer with the nitride film remains. The metal layers in Step 8 can be formed using e-beam deposition as indicated by Breuer (2000). A 100 Å layer of titanium can be used as an adhesion layer for a 1000 Å layer of platinum. Finally, a 5000 Å layer of gold would be deposited on top of the Pt/Ti. All three metals can be deposited sequentially. The sensors can then be defined by patterning and etching (with potassium iodide) the top layer of gold in selected areas to reveal the Pt/Ti layer below. This process would produce a sensor of the design shown in Fig. 6.5.

Mode	A	B
Current design (theory)	0.25	15
Liu *et al* CC (experimental)	0.08	42.7
Liu *et al* CV (experimental)	0.10	42.7
Liu *et al* CT (experimental)	0.56	42.6

Table 6.1. Tabulated values for *A*, *B* (defined in §6.4) and calculated from Fig. 6.6*a* for the current design and compared to those obtained by Liu *et al* (1999). (CC = constant current, CV = constant voltage, CT = constant temperature).
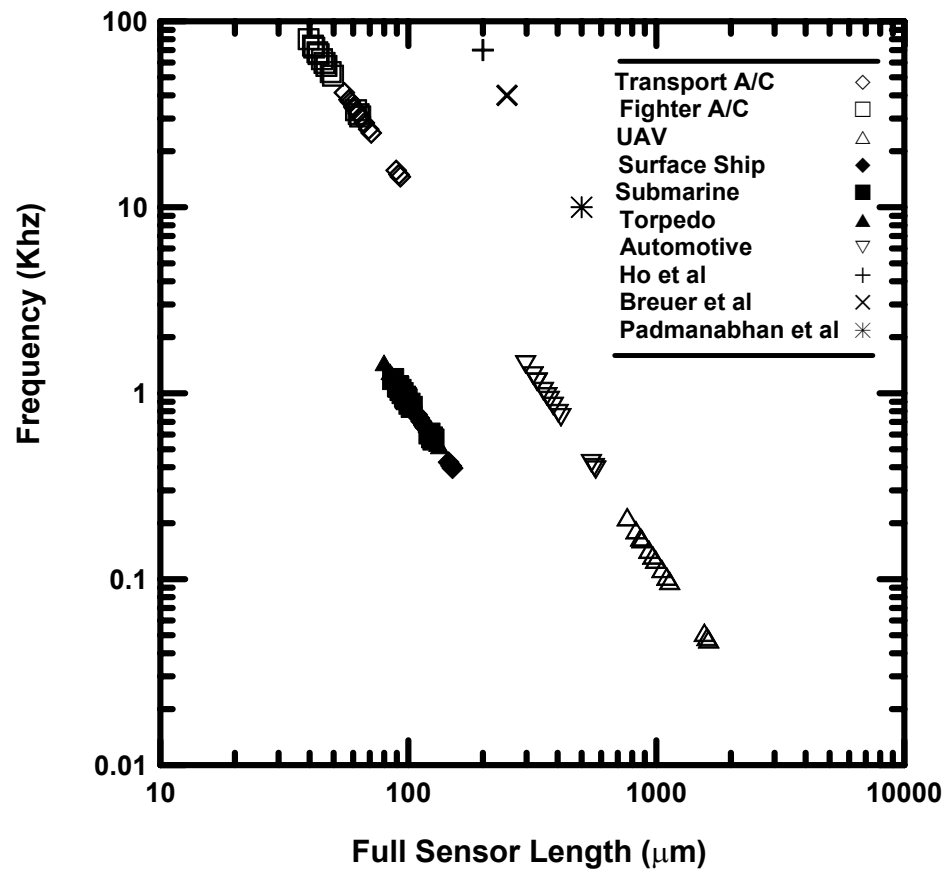
Figure 6.1. Microsensor length and frequency requirements for vehicle types in table 2.1. These sensor requirements will allow the detection of the incipient bursting of the streamwise vortical structures that naturally occur in a turbulent boundary layer as described in §2. The design allows for collocation with the MEKA actuators shown in §5.
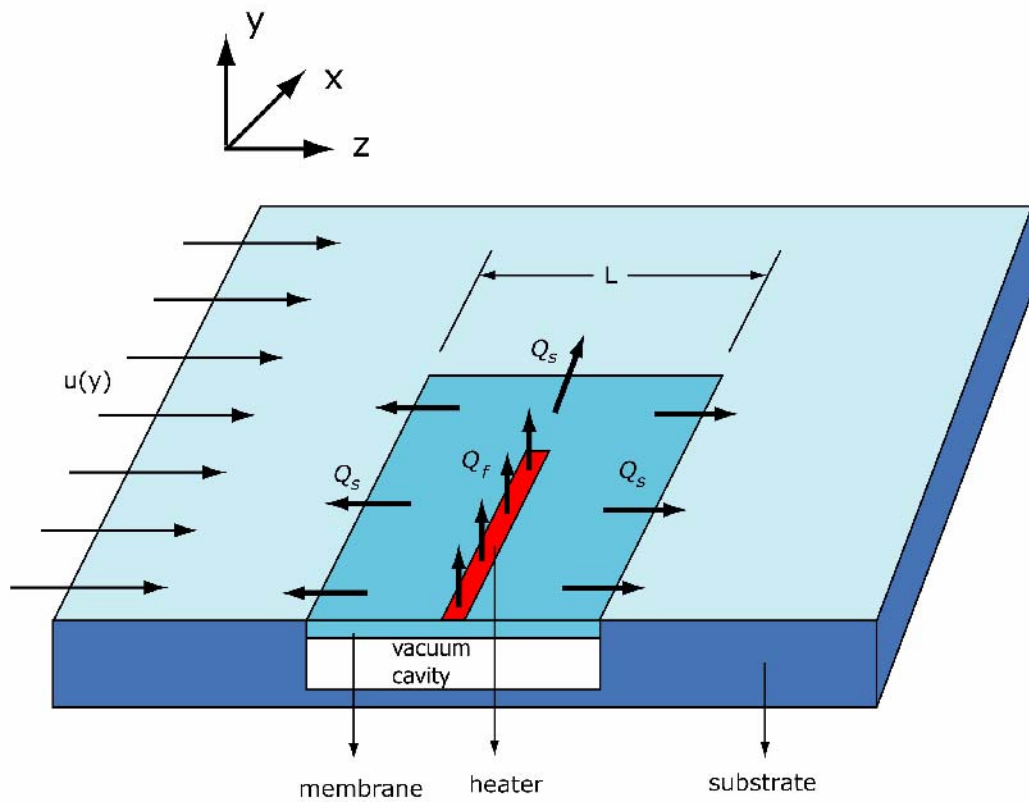
Figure 6.2. Schematic of a wall shear stress thermal sensor of length L embedded on a wall and capable of detecting the incipient bursting signature of the coherent structures in a turbulent boundary layer. The heat transfer losses from the sensor to the substrate Q_s are shown. The heat transfer to the fluid is shown by Q_f.
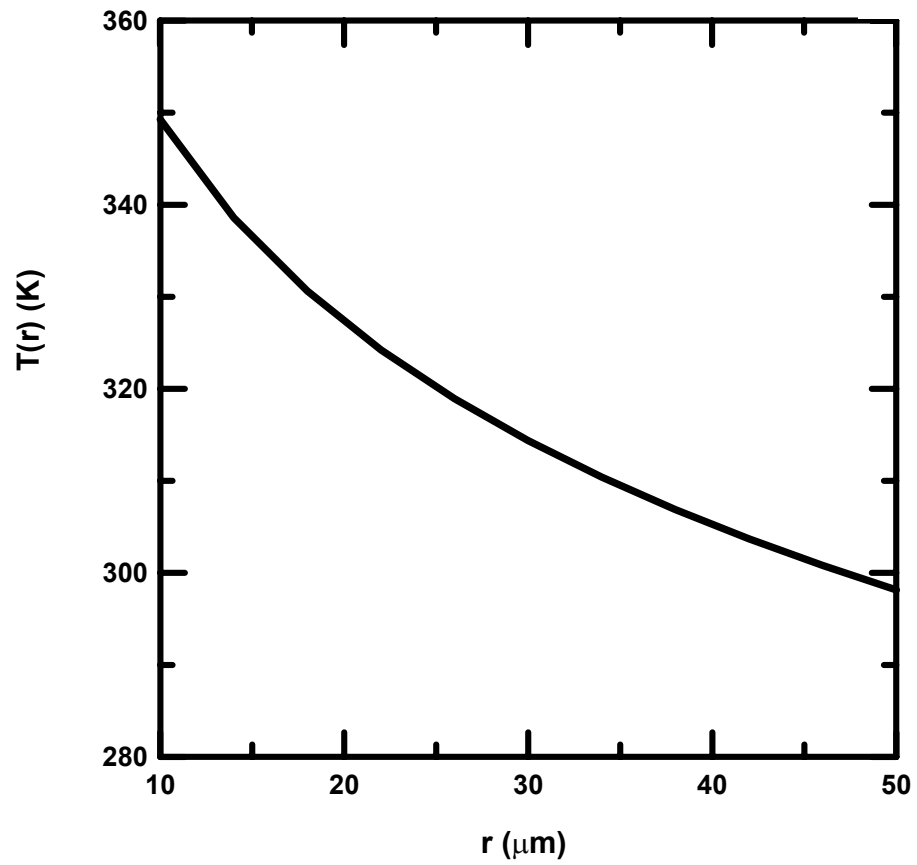
Figure 6.3.   Radial temperature distribution are shown for a thermal sensor composed of a heated thin film, at a temperature $T_i = 350$ K, located in the center of a 50 μm circular silicon nitride membrane.

(a)
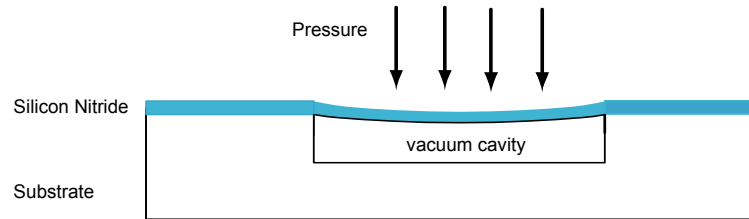
(b)
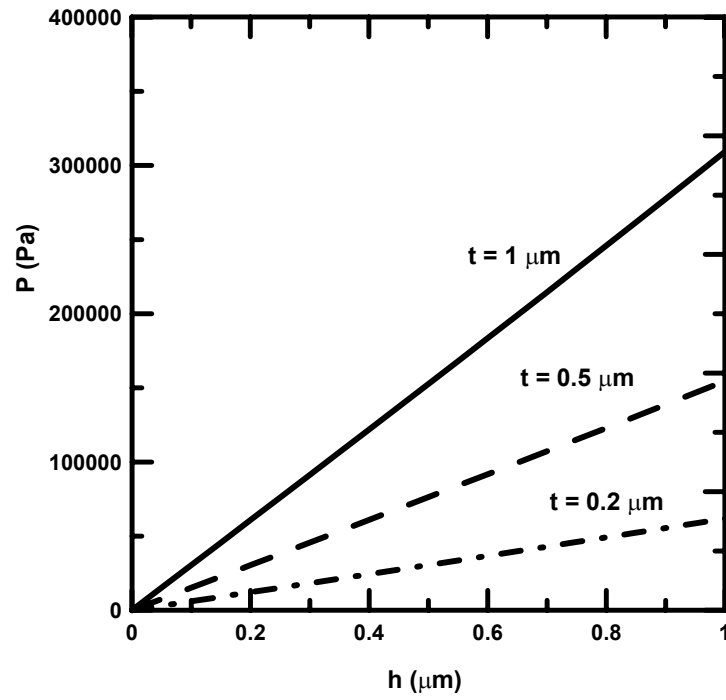
Figure 6.4.   *(a)* Cross sectional view of a thermal sensor showing a silicon nitride membrane of thickness *t*, with a sealed vacuum cavity underneath, being deflected by a pressure load, and *(b)* maximum membrane deflection at its center point for different pressure loads.
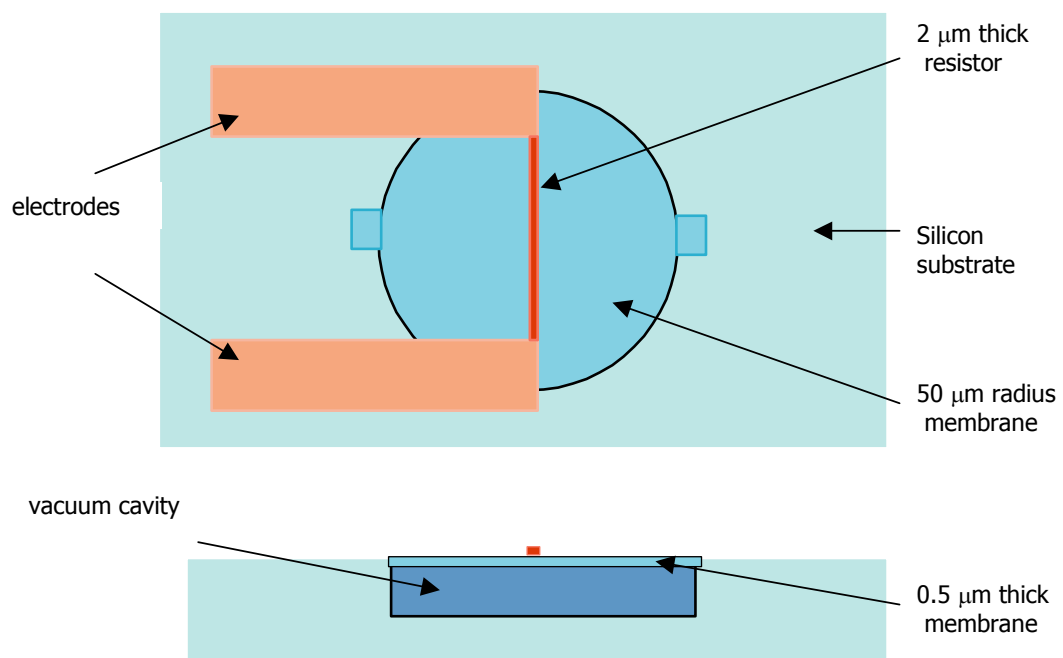
Figure 6.5.   Schematic showing a thermal sensor. *(a)* Top view shows the gold electrodes and platinum resistor located on top of a circular membrane, and *(b)* the cross sectional view of the sensor shows also the silicone membrane with a vacuum cavity underneath used to increase the sensitivity of the sensor by reducing the heat transfer losses.

(a)

$y = 0.2479x + 15.0$

P/ΔT (m-W/K)

$\tau_w^{1/3}$ (Pa$^{1/3}$)

(b)

Voltage (mV)

τ_w (Pa)
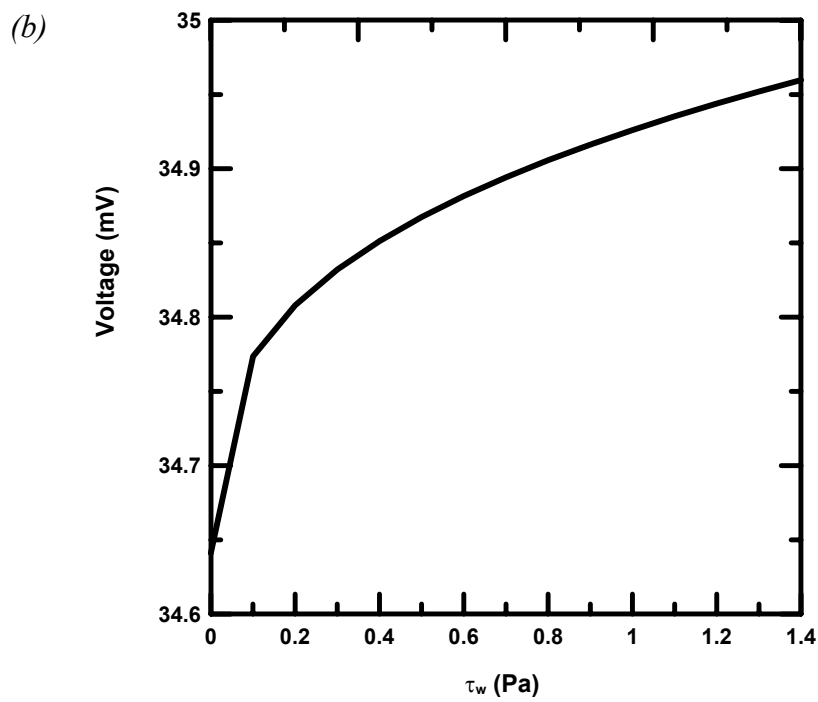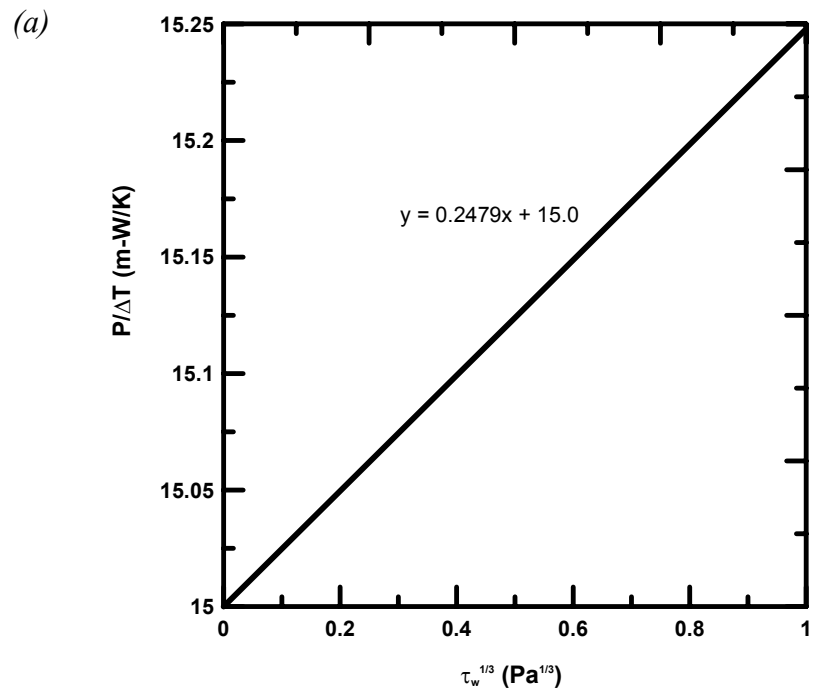
Figure 6.6   (Caption on next page)

157
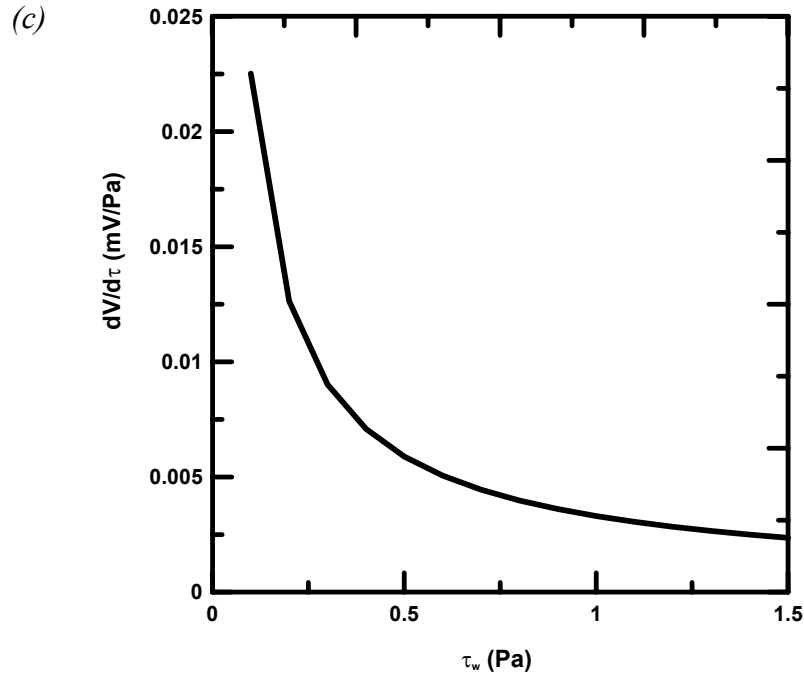
Figure 6.6.   The performance of the designed thermal sensor is characterized by *(a)* the ratio of input power to temperature difference against $\tau_w^{1/3}$, *(b)* the theoretical predictions for the measured voltage across the sensor element for various values of the wall shear stress τ_w and *(c)* the resulting theoretical sensitivity of the proposed sensor design from (6.10).

(a)   Silicon nitride is deposited by LPCVD
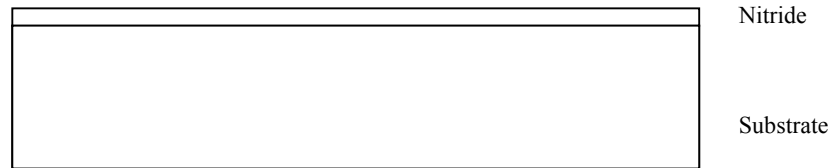
(b)   Photolithographically patterned to define cavities (100 μm x 100 μm)

(c)   Silicon dioxide is grown using thermal oxidation (1.3 μm)
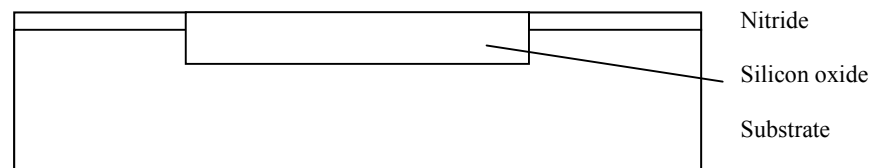
(d)   500-nm LPCVD sacrificial phosphosilicate glass (PSG)
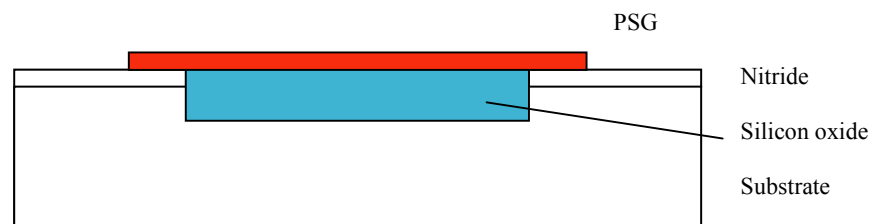
Figure 6.7.   Major fabrication steps required for the production of the designed wall shear stress sensor. These steps are based on those used by Huang *et al* (1999) with some modifications outlined in §6.5.

(e) Patterned and unmasked PSG is etched with hydrofluoric acid

PSG

Nitride

Silicon oxide

Substrate

(f) Silicon nitride is deposited (1.2 µm)

Nitride

Nitride

Silicon oxide

Substrate
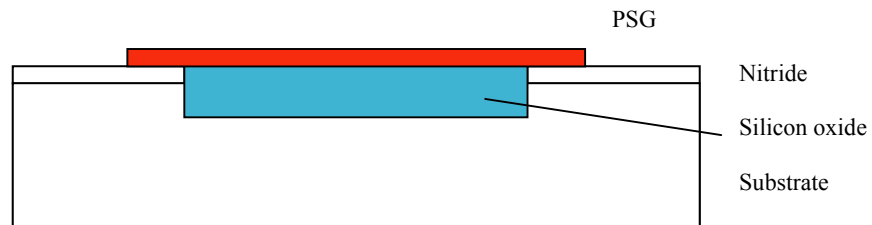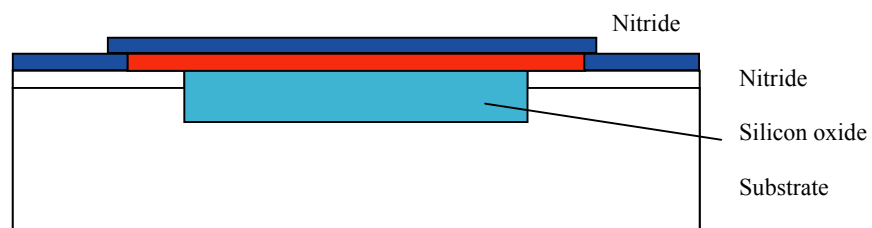
(g) Etch hole with SF6 plasma. Etch PSG and nitride with HF

etch hole

Nitride

Substrate
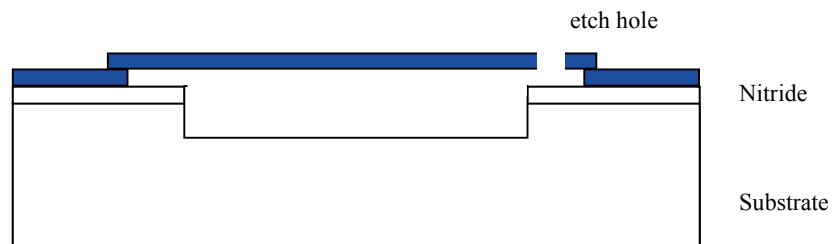
(h) Seal hole and deposite electrodes
Gold leads (1000 A), Platinum resistor (1000 A)

Nitride

Substrate
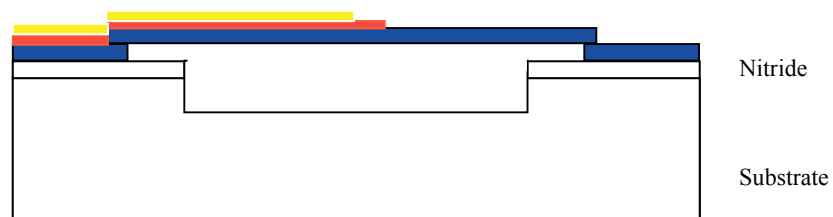
Figure 6.7.   (Caption on previous page).

CHAPTER 7

CONCLUSIONS

Major results and conclusions from the present study of electrokinetic microactuator arrays for active sublayer control in turbulent boundary layers can be summarized as follows:

1. The present study has been the first to examine the electrokinetic principle as the basis for a new class of microscale actuator arrays for active sublayer control on full scale aeronautical and hydronautical vehicles under realistic operating conditions; the Helmholtz-Smoluchowski scalings that govern such electrokinetic actuator arrays show significant performance advantages from their miniaturization to the microscale.

2. Specific performance requirements for microactuator spacing, flow rate, and frequency response for active sublayer control have been determined from fundamental scaling laws for the streamwise vortical structures in the sublayer of turbulent boundary layers.

3. In view of the inherently local nature of the sublayer dynamics, a general system architecture for microactuator arrays appropriate for active sublayer control has been developed based on the concept of relatively small and independent "unit cells", each with their own sensing, processing, and actuation capability, that greatly simplifies the sensing and processing requirements needed to achieve practical sublayer control.

4. A key innovation in this system architecture is the possibility of replacing previously elaborate control processing requirements with a simple look-up table approach implemented at the unit-cell level, in which a sensor state vector provides the input to a simple programmable logic array (PLA) that determines the corresponding actuator state vector; such an approach is made possible by the comparatively small number of sensors and actuators within each unit cell.

5. A microscale wall shear stress sensor has been proposed that meets the performance requirements for sublayer control on full-scale vehicles; individual sensor states are determined from the sensor output by an averaging and thresholding procedure that essentially eliminates the usual concerns regarding drift in the sensor calibrations, and effects caused by changes in the vehicle speed and attitude.

6. A fundamental three-layer design has been developed for such electrokinetic microactuator arrays, in which electrokinetic flow is induced by an impulsively applied electric field across a center layer, with a bottom layer containing an electrolyte reservoir and a common electrode, and a top layer that contains individual electrodes and lead-outs for each microactuator in the unit cell.

7. A recently-developed porous polymer fabrication technology has been adapted to permit formation of fine-pore matrix structures suitable for electrokinetic pumping in large, dense arrays of microchannels located in the center layer; porous polymer matrix structures with 1 μm average pore sizes can be readily created within the electrokinetic pumping channels.

8. Measured volume flow rates produced by such porous polymer-filled electrokinetic microchannels under the effect of steady applied electric fields have been shown to meet the requirements for active sublayer control on full-scale vehicles; the thin layers into which these electrokinetic microactuators can be fabricated permits the required field strengths to be achieved with potential differences of the order of 15-20 V.

9. Simple hydrodynamic models have been developed for the frequency response of such electrokinetic microactuators under the effect of sinusoidally or impulsively applied fields; these show that electrokinetically-induced flow in 1 μm-scale porous polymer matrix structures achieve essentially quasi-steady performance at frequencies up to 1 MHz.

10. Measurements of the actual frequency response achieved in such electrokinetic actuators have verified essentially loss-less AC performance at frequencies as high as 10 kHz; the observed roll-off at higher frequencies may be due to inhomogeneities in the porous polymer structure that lead to inertial damping at these frequencies.

11. Microfabrication techniques have been developed that permit mass production of large numbers of individual electrokinetic microactuators in unit cells on comparatively large-area tiles; CO_2 laser drilling of individual actuator channels can be accomplished in thin flexible plastic substrates that are compatible with the solvents used in the porous polymer constituents.

12. Several generations of such electrokinetic microactuator arrays have been built leading to the MEKA-5 full-scale hydronautical array, composed of 25,600 individual electrokinetic microactuators with 350 μm center-to-center spacings, arranged in a 40×40 pattern of unit cells, each composed of a 4×4 matrix of actuators; this array was successfully fabricated in a 7×7 cm² tile in 250 μm thick mylar substrate material.

13. MEMS design and fabrication processes were used to produce a top layer for the MEKA-5 hydronautical-scale array, composed of an electrode sublayer patterned in Cr/Au, a nozzles sublayer etched in polyimide, and a cavities sublayer fabricated in Su-8; the functionality incorporated in this top layer fabrication demonstrates the complete elements needed for microscale electrokinetic actuator arrays for sublayer control.

14. Stereo-PIV measurements successfully demonstrated lateral displacement of synthetically-generated streamwise vortical structures by volumetric pumping from a wall actuator in a set of large-scale wind tunnel tests; results characterized the relative lateral displacement achieved as a function of the dimensionless pumping strength q/Γ. Despite differences between the large-scale actuator used in these measurements and the microscale electrokinetic actuators that are the subject of this study, the results obtained suggest that manipulation of naturally-occurring sublayer vortices in turbulent boundary layers by volumetric pumping with wall actuators is possible at comparable dimensionless pumping strengths q/Γ.

APPENDICES

APPENDIX A

SLOT-TYPE MICROACTUATOR ARRAYS

For open-loop control based on the oscillating wall approach, volume displacement is through slots nominally aligned with the near-wall flow. Such slot microactuators, shown in Figure A.1 are between adjacent slot pairs. Adjacent slots pairs produce alternatively positive or negative volume displacements, in a time-oscillating fashion, to displace fluid above the wall along the cross-stream direction. The volume displacements are again created by electrokinetic pumping within the much larger microactuator channels in a center layer. In this case the slot spacing is less critical, and key performance requirements are the frequency and flowrate needed to achieve effective spanwise oscillation of the fluid above the wall.

For the open-loop control approach based on slot microactuators it is apparent that the spacing of such actuators is dependent on the number, N, of sublayer vortices typically located between adjacent slot pairs. For the present case lets choose $N = 1$ so we can compare the flow rate requirements for the slot actuators and single point actuators.

The following assumptions are made while calculating the flow rate for a slot actuator:

1.- We expect to move the midpoint between slots a distance of 10 y^+ back and forth between cycles.

2.- The Reynolds number should be chosen small to prevent inertia effects.

3.- A square wave voltage will be used from now on as the driver of the electrokinetic actuator.

4.- The slots will be treated as a potential source/sink for the purpose of calculating the flow rate and exit velocity.

The flow velocity at a distance r from a potential source is given by

$$u_r = 2 \frac{Q}{2\pi} \frac{1}{r} \tag{A.1.1}$$

where 2Q, the source strength, is the flow rate per unit length and r is the radial distance from the source. Notice that we use 2Q to denote the total flow rate per unit length issuing from the source. Figure A.2 shows an ideal view of the slots actuating.

Thus, the mid point velocity is given by

$$u_{midpoint} = \frac{Q}{\pi} \frac{1}{\Delta/2} - \frac{-Q}{\pi} \frac{1}{\Delta/2}, \tag{A.1.2}$$

where Δ is the distance between slots.

Simplifying (A.1.2) we obtain,

$$u_{midpoint} = \frac{4Q}{\pi\Delta} \tag{A.1.3}$$

This $u_{midpoint}$ is constant during the oscillation period T/2.

During time T/2 we need to move the midpoint a distance 10 l_τ, wall units.

$$10 l_\tau = u_{midpoint} \frac{T}{2}, \tag{A.1.4}$$

substituting for $u_{midpoint}$

$$10 l_\tau = \frac{4}{\pi} \frac{Q}{\Delta} \frac{T}{2} \tag{A.1.5}$$

and solving for Q we obtain,

$$Q = 5\pi l_\tau \frac{\Delta}{T}. \tag{A.1.6}$$

We have chosen T = 100[+], although further checks should be done to see if this is the appropriate value.

$$T = 100 \frac{\nu}{\tau_w/\rho} = 100 \frac{l_\tau^2}{\nu}, \tag{A.1.7}$$

where l_τ is given by

$$l_\tau = \frac{\nu}{\sqrt{(\tau_w/\rho)}}. \tag{A.1.8}$$

167

Substituting (A.1.7) into (A.1.6) we obtain

$$Q = 5\pi\nu N,$$ (A.1.9)

where N is the number of vortices between slots and is defined as

$$N = \frac{\Delta}{100l_\tau}.$$ (A.1.10)

Using w, the width of the slot, as the characteristic length we obtain the Reynolds number as follows

$$Re = \frac{Uw}{\nu} = \frac{Q}{\nu}.$$ (A.1.11)

Substituting (A.1.10) into (A.1.11) we obtain a Reynolds number that is only dependent on the number of vortices allocated between slots.

$$Re = 5\pi N.$$ (A.1.12)

Let us assume that the gap between the electrokinetic beds is negligible for both point and slot actuator. Then, a sketch of points and slot actuators is shown in Figure A.3. The dimensions have been chosen to simplify the results.

Next, we will show that the flow rate that two point actuators need to deliver in order to successfully cancel or modify the sublayers streaks is a factor of exactly 75 times smaller than the flow rate a slot actuator will need to oscillate the wall at the correct frequency.

The volume displaced by a point actuator is given by

$$V_{point} = \frac{2}{3}\pi R_{point}^3,$$ (A.1.13)

where $R_{point} = 10\, l_\tau$ is the radius of this virtual hemisphere. Also, the flow rate per stroke is given by

$$Q_{point} = V_{point}\frac{1}{f},$$ (A.1.14)

where f is the frequency at which this virtual hemispheres will need to be created. On the other hand, the flow rate per stroke displaced by a slot actuator is given by a virtual half cylinder as

$$Q_{slot} = \pi\frac{R_{slot}^2}{2}L\frac{1}{f}$$ (A.1.15)

where $R_{slot} = 3.162\, R_{point}$.

Figure A.3 shows a sketch where there are two point actuators for every slot actuator. Thus, in order to compare the flow rates between slots and point actuators we will need to look at the ratio of

$$\frac{Q_{slot}}{2Q_{point}} = \frac{3L}{8} \frac{R^2_{slot}}{R^3_{point}}, \tag{A.1.16}$$

where (A.1.13) and (A.1.14) have already been substituted in (A.1.16). By substituting L $= 2\Delta = 200\,l_\tau$ and $R_{point} = 10\,l_\tau$ into (A.1.16) the following ratio is obtained

$$\frac{Q_{slot}}{2Q_{point}} = 75 \tag{A.1.17}$$

This large difference in flow rates between the point actuator and the slot actuator is plotted in Figure A.4.

We still need to prove for the slot actuator that we need to displace per stroke an amount of flow equivalent to the volume of half a cylinder of radius $31.62\,l_\tau$ and length fix by the length of the slot. Recall that the flow rate per unit length is given by (A.1.9). The assumption is made that the volume displaced per stroke per unit length is given by

$$Q = \frac{\pi R^2_{slot}}{2} \frac{1}{\Delta T}, \tag{A.1.18}$$

where R_{slot} is the radius of the virtual volume of a half a cylinder displaced by the slot actuator per stroke. The oscillation time T was given by (A.1.7) as

$$T = 100 \frac{\nu}{\tau_w/\rho} = 100 \frac{l_\tau^2}{\nu}. \tag{A.1.19}$$

Substituting (A.1.7) into (A.1.17), equating the result with (A.1.9) and substituting for R_{slot} we get

$$R_{slot} = 31.62 l_\tau. \tag{A.1.20}$$

Top Layer

Actuator
Nozzles &
Electrodes

Center Layer

Electrokinetic
Channels
& Matrix

Bottom Layer

Electrolyte
Reservoir
& Common
Electrode
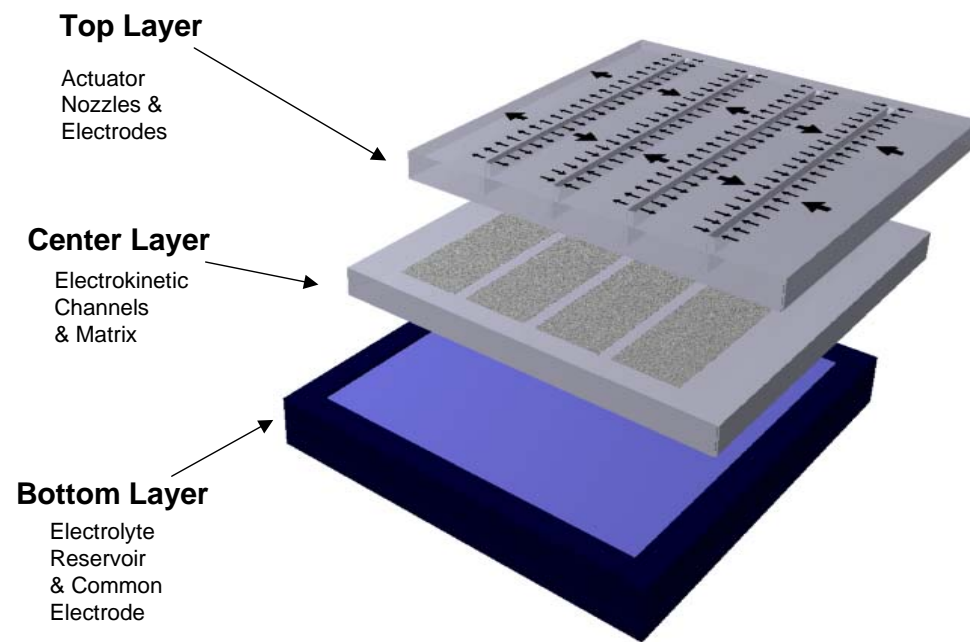
Figure A.1 Basic Three-layer design of slot-type microactuator arrays for "oscillating wall" control approach.
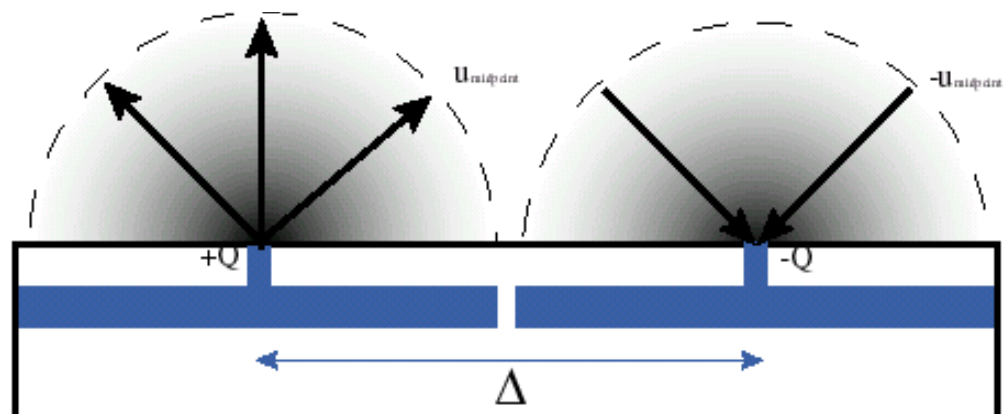
Figure A.2 Slot actuator. The left actuator is issuing fluid while the right actuator is pumping fluid in.
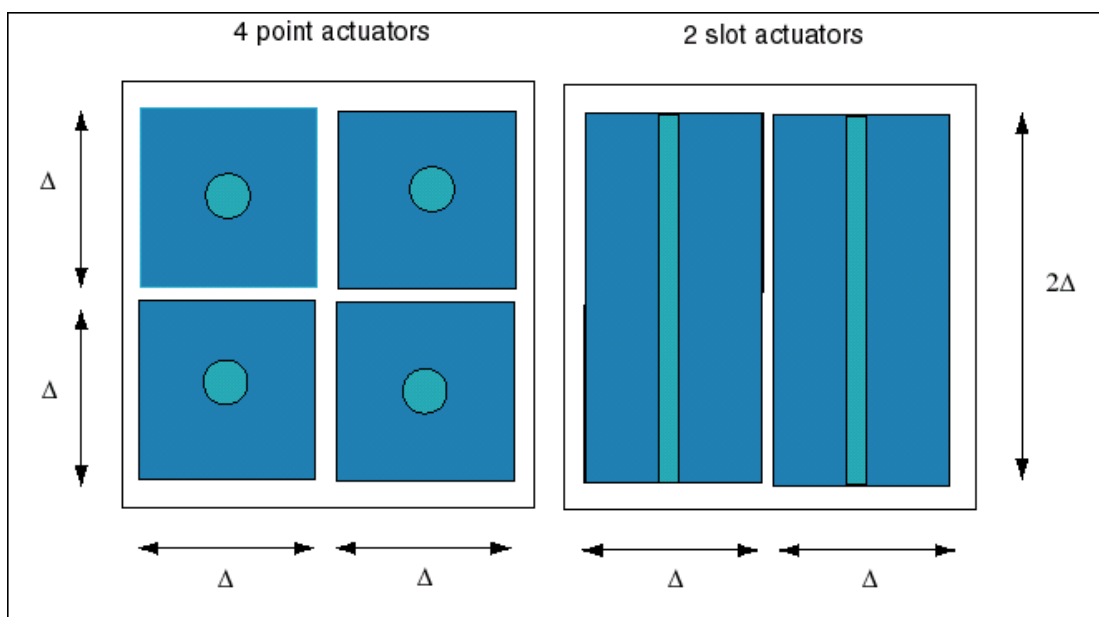
Figure A.3 Drawing of a slot actuator whose electrokinetic bed is twice the size of a point actuator, N = 1.
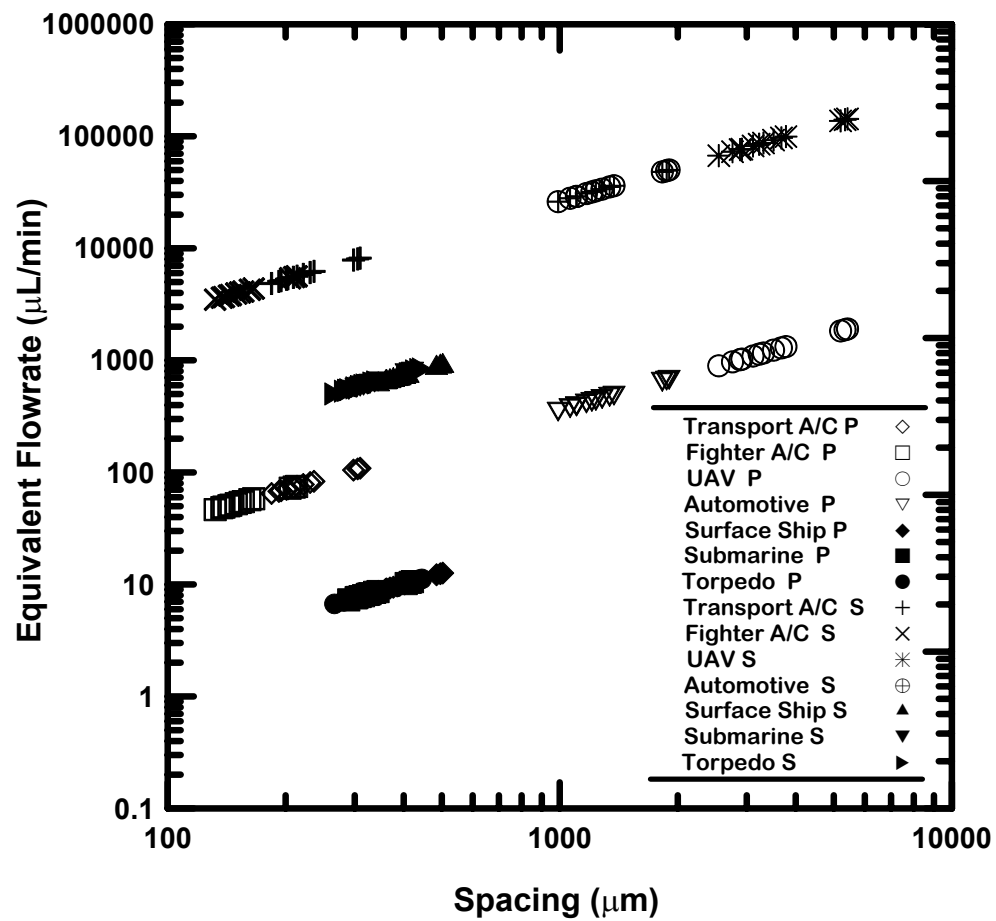
 Figure A.4 Comparison of flow rate requirements for slot actuators and point actuators.
(S = slots actuators and P = point actuators)

BIBLIOGRAPHY

BIBLIOGRAPHY

Akhavan, R., Jung, W.J. & Mangiavacchi, N. (1993) Turbulence control in wall bounded flows by spanwise oscillations. *Appl. Sci. Res.* **51**, 299-303.

Alshamani, K.M.M., Livesey, J.L, & Edwards, F.J. (1982) Excitation of wall region by sound in fully developed channel flow. *AIAA J.* **20**, 334-339.

Bewley, T.R. (2001) Flow control: new challenges for a new Renaissance. *Prog. Aerospace Sci.* **37**, 21-58.

Berger, T.W., Kim, J., Lee, C. & Lim, J. (1999) Turbulent boundary layer control utilizing the Lorentz force. *Phys. Fluids* **12**, 631-649.

Blackwelder, R.F. & Eckelmann, H. (1979) Streamwise vortices associated with the bursting phenomenon. *J. Fluid Mech.* **94**, 577-594.

Bockris, J.O'M. & Khan, S.U.M. (1993) <u>Surface</u> <u>Chemistry</u>: <u>A</u> <u>Molecular</u> <u>Level</u> <u>Approach</u>, Plenum, New York.

Breuer, K.S. (2000) MEMS sensors for aerodynamic measurements- the good, the bad (and the ugly). *AIAA Paper 2000-0251*, AIAA, Washington, D.C.

Breuer, K.S., Haritonidis, J.H. & Landahl, M. (1989) The control of transient disturbances in a flat plate boundary layer through active wall motion. *Phys. Fluids A* **1**, 574-582.

Burgreen, D. & Nakache, F.R. (1964) Electrokinetic flow in ultrafine capillary slits. *J. Phys. Chem.* **68**, 1084-1091.

Bushnell, D. & McGinley, C. (1989) Turbulent control in wall flows. *Annu. Rev. Fluid Mech.* **21**, 1-20.

Cantwell, B.J. (1981) Organized motion in turbulent flow. *Annu. Rev. Fluid Mech.* **13**, 457-515.

Carlson, H.A. & Lumley, J.L. (1996*a*) Active control in the turbulent wall layer of a mini-

mal flow unit. *J. Fluid Mech.* **329**, 341-371.

Carlson, H.A. & Lumley, J.L. (1996*b*) Flow over an obstacle emerging from the wall of a channel. *AIAA J.* **34**, 924-931.

Chara, Z., Zakin, J.L. & Myska, S.J. (1993) Turbulence measurements of drag reducing surfactant systems. *Expts. Fluids* **16**, 36-41.

Choi, H., Moin, P. & Kim, J. (1993) Direct numerical simulation of turbulent flow over riblets. *J. Fluid Mech.* **255**, 503-539.

Choi, H., Moin, P. & Kim, J. (1994) Active turbulence control for drag reduction in wall-bounded flows. *J. Fluid Mech.* **262**, 75-110.

Choi, H., Temam, R., Moin, P. & Kim, J. (1993) Feedback control for unsteady flow and its application to the stochastic Burgers equation. *J. Fluid Mech.* **253**, 509-543.

Choi, K.-S. (1989) Near-wall structure of a turbulent boundary layer with riblets. *J. Fluid Mech.* **208**, 417-458.

Choi, K.-S. (1993) Turbulent structure revisited; results and implications from riblets research. In Near Wall Turbulent Flows, Elsevier, New York, 699-707.

Coles, D. (1956) The law of the wake in the turbulent boundary layer. *J. Fluid Mech.* **1**, 191.

Corino, E.R. & Brodkey, R.S. (1969) A visual investigation of the wall region in turbulent flow. *J. Fluid Mech.* **37**, 1-30.

Crawford, C.H. & Karniadakis, G.E. (1997) Reynolds stress analysis of EMHD-controlled wall turbulence. Part 1. Streamwise forcing. *Phys. Fluids* **9**, 788-806.

Crow, D.R. (1988) Principles and Applications of Electrochemistry, Chapman and Hall, New York.

Dahm, W.J.A. & Diez-Garias, F.J. (2001) Electrokinetic microactuator arrays for sublayer control in turbulent boundary layers. *Proc. 2nd Int'l. Symp. on Smart Control of Turbulence*, 107-116, University of Tokyo, Tokyo.

Dahm, W.J.A., Paul, P.H., Rakestraw, D.J. & Scherer, J.J. (1997) Fluid microactuators based on the electrokinetic principle. *Bull. Am. Phys. Soc.* **42**, 2247.

Das, DK (1987) A numerical study of turbulent separated flows. *Amer. Soc. Mech. Eng. Forum on Turbulent Flows, FED* **51**, 85-90.

Diez-Garias, F.J., Dahm, W.J.A. & Paul, P.H. (2000) Microactuator arrays for sublayer control in turbulent boundary layers using the electrokinetic principle. *AIAA Paper 2000-0548*, AIAA, Washington, D.C.

Endo, T., Kasagi, N. & Suzuki, Y. (1999) Feedback control of wall turbulence with wall deformation. *1st Int'l. Symp. Turbulence & Shear Flow Phenomena*, Santa Barbara, Ca., 405-410.

Fiedler, H.E. & Fernholz, H.H. (1990) On management and control of turbulent shear flows. *Prog. Aerospace Sci.* **27**, 305-387.

Gad-el-Hak, M. (1989) Flow control. *Appl. Mech. Rev.* **42**, 261-293.

Gad-el-Hak, M. (1994) Interactive control of turbulent boundary layers: A futuristic overview. *AIAA J.* **32**, 1753-1765.

Gad-el-Hak, M. (1996) Modern developments in flow control. *Appl. Mech. Rev.* **49**, 365-379.

Gad-el-Hak, M. (2001) Flow control: the future. *J. Aircraft* **38**, 402-418.

Gad-el-Hak, M. & Blackwelder, R.F. (1987) A drag reduction method for turbulent boundary layers. *AIAA Paper 87-0358*, AIAA, Washington, D.C.

Gad-el-Hak, M. & Blackwelder, R.F. (1989) Selective suction for controlling bursting events in a boundary layer. *AIAA J.* **27**, 308-314.

Gottero, M. & Onorato, M. (2000) Low-speed streak and internal shear layer motions in a turbulent boundary layer. *Eur. J. Mech. B - Fluids* **19**, 23-36.

Hamilton, J.M., Kim, J. & Waleffe, F. (1995) Regeneration mechanisms of near-wall turbulence structures. *J. Fluid Mech.* **287**, 317-348.

Hammond, E.P., Bewley, T.R. & Moin P. (1998) Observed mechanisms for turbulence attenuation and enhancement in opposition-controlled wall-bounded flows. *Phys. Fluid* **10**, 2421-2423.

Henoch, C. & Stace, J. (1995) Experimental investigation of a salt water turbulent boundary layer modified by an applied streamwise magnetohydrodynamic body force. *Phys. Fluid* **7**, 1371-1383.

Ho, C.-M. & Tai, Y.-C. (1996) Review: MEMS and its application to flow control. *J. Flu-

ids Engng. **118**, 437-447.

Ho, C.-M. & Tai, Y.-C. (1998) Micro-electro-mechanical-systems (MEMS) and fluid flows. *Annu. Rev. Fluid Mech*. **30**, 579-612.

Hoyt, J.W. (1990) Viscous drag reduction in boundary layers. *Prog. Astronautics & Aeronautics* **123**, 413-432, AIAA, Washington, D.C.

Huang, J-B., Tung, S., Ho, C.-H., Liu, C. & Tai, Y-C. (1996) Improved micro thermal shear-stress sensor. *IEEE Transact. Instr. Meas.* **45**, 570-574.

Huang, J.B., Jiang, F.K., Tai, Y.C. & Ho, C.M. (1999) A micro-electro-mechanical-system-based thermal shear-stress sensor with self-frequency compensation. *Meas. Sci. Technol.* **10**, 687-696.

Hunter, R.J. (1981) Zeta Potential in Colloid Science. Principles and Application, Academic, London.

Jacobson, S.A. & Reynolds, W.C. (1993) Active boundary layer control using flush mounted surface actuators. *Bull. Am. Phys. Soc.* **38**, 2197.

Jacobson, S.A. & Reynolds, W.C. (1998) Active control of streamwise vortices and streaks in boundary layers. *J. Fluid Mech.* **360**, 179-211.

Jeong, J., Hussain, F., Schoppa, W. & Kim, J. (1997) Coherent structures near the wall in a turbulent channel flow. *J. Fluid Mech.* **332**, 185-214.

Jiménez, J. & Pinelli, A. (1999) The autonomous cycle of near-wall turbulence. *J. Fluid Mech.* **389**, 335-359.

Johansen, J.B. & Smith, C.R. (1986) The effects of cylindrical surface modifications on turbulent boundary layers. *AIAA J.* **24**, 1081-1087.

Jung, W.J., Mangiavacchi, N. & Akhavan, R. (1992) Suppression of turbulence in wall-bounded flows by high-frequency spanwise oscillations. *Phys. Fluids A* **4**, 1605-1607.

Kang, S. & Choi, H. (2000) Active wall motions for skin-friction drag reduction. *Phys. Fluids* **12**, 3301-3304.

Kim, H.T., Kline, S.J. & Reynolds, W.C. (1971) The production of turbulence near a smooth wall in a turbulent boundary layer. *J. Fluid Mech.* **50**, 133-168.

Kimura, M., Tung, S., Lew, J., Ho, C.-M., Jiang, F. & Tai, Y.-C. (1999) Measurements of

wall shear stress of a turbulent boundary layer using a micro-shear-stress imaging chip. *Fluid Dyn. Res*. **24**, 329-342.

Kline, S.J., Reynolds, W.C., Schraub, F.A. & Runstadler, P.W. (1967) The structure of turbulent boundary layers. *J. Fluid Mech.* **30**, 741-773.

Laadhari, F., Skandaji, L. & Morel, R. (1994) Turbulence reduction in a boundary layer by a local spanwise oscillating surface. *Phys. Fluids* **6**, 3218-3220.

Lazos, B.S. & Wilkinson S.P. (1988) Turbulent viscous drag reduction with thin-element riblets. *AIAA J.* **26**, 496-498.

Levine, S., Marriott, J.R., Neale, G. & Epstein, N. (1975) Theory of electrokinetic flow in fine cylindrical capillaries at high zeta-potentials. *J. Colloid Interface Sci.* **52**, 136-149.

Lim, J., Choi, H & Kim, J. (1998) Control of streamwise vortices with uniform magnetic fluxes. *Phys. Fluids* **10**, 1997-2005.

Liu, C., Huang, J.-B., Zhu, Z., Jiang, F., Tung, S., Tai, Y.-C. & Ho, C.-M. (1999) A micro-machined flow shear-stress sensor based on thermal transfer principles. *J. Micro-electromechanical Sys.* **8**, 90-99.

Löfdahl, L. & Gad-el-Hak, M. (1999) MEMS applications in turbulence and flow control. *Prog. Aerospace Sci.* **35**, 101- 203.

Lumley, J.L. (1996) Control of turbulence. *AIAA Paper 96-0001,* AIAA, Washington, D.C.

Lumley, J.L. & Blossey, P. (1998) Control of turbulence. *Annu. Rev. Fluid Mech*. **30**, 311-327.

Lumley, J.L. & Kubo, I. (1985) Turbulent drag reduction by polymer additives. The Influence of Polymer Additives on Velocity and Temperature Fields, Springer, New York, 3-21.

McMichael, J.M. (1996) Progress and prospects for active flow control using microfabricated electromechanical systems (MEMS). *AIAA Paper 96-0306*, AIAA, Washington, D.C.

Myska, J., Zakin, J.L. & Chara, Z. (1995) Viscoelasticity of a surfactant and it's drag reducing ability. *Appl. Sci. Res.* **55**, 297-310.

Mito, Y. & Kasagi, N. (1998) DNS study of turbulence modification with streamwise-uni-

form sinusoidal wall-oscillation. *Int'l. J. Heat Fluid Flow* **19**, 470.

Moin, P. & Bewley, T. (1994) Feedback control of turbulence. *Appl. Mech. Rev.* **47**, S3-S13.

Myose, R.Y. & Blackwelder R.F. (1995) Control of streamwise vortices using selective suction. *AIAA J.* **33**, 1076-1080.

Nosenchuck, D.M. & Brown, G.L. (1993) Discrete spatial control of a wall shear stress in a turbulent boundary layer. *Proc. Int'l. Conf. on Near Wall Turbulent Flows*, Elsevier, New York.

Nosenchuck, D.M. & Lynch, M.K. (1985) Active control of low-speed streak bursting in turbulent spots. *AIAA Paper 85-0535*, AIAA, Washington, D.C.

Nosenchuck, D.M., Lynch, M.K. & Stratton J.P. (1987) Active control of sublayer disturbances using an array of heating-elements. *Proc. ASME/JSME Thermal Eng. Joint Conf.* **2**, 619-627.

Orlandi, P. & Jimenez, J. (1994) On the generation of turbulent wall friction. *Phys. Fluids* **6**, 634-641.

van Oss, C.J. (1994) Interfacial Forces in Aqueous Media, Marcel Dekker, New York, 51.

Overbeek, J.Th.G. & Wiersema, P.H. (1967) Electrophoresis, **2**, Academic, New York.

Padmanabhan, A., Goldberg, H.D., Breuer, K.S. & Schmidt, M.A. (1995) A silicon micro-machined floating-element shear-stress sensor with optical position sensing by photodiodes. *The 8th Int'l. Conf. Solid-State Sensors and Actuators*, Stockholm, Sweden, 436-439.

Peters E.C., Petro, M., Svec, F. & Fréchet J.M.J. (1998*a*) Molded rigid polymer monoliths as separation media for capillary electrochromatography. 1. Fine control of porous properties and surface chemistry. *Anal. Chem.* **70**, 2288-2295.

Peters E.C., Petro, M., Svec, F. & Fréchet J.M.J. (1998*b*) Molded rigid polymer monoliths as separation media for capillary electrochromatography. 2. Effect of chromatographic conditions on the separation. *Anal. Chem.* **70**, 2296-2302.

Pollard, A. (1997) Passive and active control of near-wall turbulence. *Prog. Aerospace Sci.* **33**, 689-708.

Potter, E.C. (1961) Electrochemistry, Principles and Applications, Cleaver-Hume, London.

Rathnasingham, R. & Breuer K.S. (1997) System identification and control of a turbulent boundary layer. *Phys. Fluids* **9**, 1867-1869.

Rebbeck, H. & Choi K.-S. (2001) Opposition control of near-wall turbulence with a piston-type actuator. *Phys. Fluids* **13**, 2142-2145.

Reuss, F. F. (1809) Sur un nouvel effet de l'éctricité galvanique. *Memoires de la Societé Imperiale de Naturalistes de Moscou* **2**, 327-337.

Rice, C.L. & Whitehead, R. (1965) Electrokinetic flow in a narrow cylindrical capillary. *J. Phys. Chem.* **69**, 4017-4023.

Robinson, S.K. (1991) Coherent motion in the turbulent boundary layer. *Annu. Rev. Fluid Mech.* **23**, 601-639.

Schoppa, W. & Hussain, F. (2000*a*) Coherent structure dynamics in near-wall turbulence. *Fluid Dyn. Res.* **26**, 119-139.

Schoppa, W. & Hussain, F. (2000*b*) Generation of near-wall coherent structures in a turbulent boundary layer. *Current Science*, **79**, 849-858.

Schmidt, M.A., Howe, R.T., Senturia, S.D. & Haritonidis, J.H. (1988) Design and calibration of a microfabricated floating-element shear-stress sensor. *IEEE Transactions Electron Devices* **35**, 750-757.

Sexl, T. (1930) Über den von E.G. Richardson entdeckten 'Annulareffekt'. *Z. Phys.* **61**, 349-362.

Shajii, J., Ng, K.Y. & Schmidt, M.A. (1992) A microfabricated floating-element shear stress sensor using wafer-bonding technology. *J. Microelectromechanical Sys.* **1**, 89-94.

Sherman, F., Tung, S., Kim, C.-J., Jo, C.-M. & Woo, J. (1999) Flow control by using high-aspect-ratio, in-plane microactuators. *Sensors and Actuators A* **73**, 169-175.

Soloff, S.M., Adrian R.J., Liu, Z.-C. (1997) Distortion compensation for generalized stereoscopic particle image velocimetry. *Meas. Sci. Technol.* **8**, 1441-1454.

Tabata, O., Kawahata, K., Sugiyama, S. & Igarashi, I. (1989) Mechanical property measurements of thin films using load-deflection of composite rectangular membranes. *Sensors and Actuators* **20**, 135-141.

Toms, B.A. (1949) Detection of a wall effect in laminar flow of solutions of a linear polymer. *J. Coll. Sci.* **4**, 511-521.

Tsao, T., Liu, C., Tai, Y.-C. & Ho, C.-M. (1994) Micromachined magnetic actuator for active fluid control. *ASME Int'l. Mech. Eng. Congress and Expo.*, Chicago, Il., 31-38.

Walsh, M.J. (1983) Riblets as a viscous drag reduction technique. *AIAA J.* **21**, 485-486.

Walsh, M.J. & Weinstein L.M. (1979) Drag and heat-transfer characteristics of small longitudinally ribbed surfaces. *AIAA J.* **17**, 770-771.

Warholic, M.D., Schmidt, G.M. & Hanratty T.J. (1999) The influence of a drag reducing surfactant on a turbulent velocity field. *J. Fluid Mech.* **388**, 1-20.

Wilkinson, S.P. (1990) Interactive wall turbulence control. In "Viscous Drag Reduction in Boundary Layers" (Bushnell, D.M. & Hefner, J.N., Eds.) *Prog. Astronautics & Aeronautics* **123**, 479-509, AIAA, Washington, D.C.

Wilkinson, S.P. & Balasubramanian, R. (1985) Turbulent burst control through phase-locked surface depressions. *AIAA Paper 85-0536*, AIAA, Washington, D.C.

Wolf, S. & Tauber, R.N. (1986) <u>Silicon</u> <u>Processing</u> <u>for</u> <u>the</u> <u>VLSI</u> <u>Era</u>, Lattice Press, Sunset Beach, Ca.

Zakin, J.L. & Qi, Y. (2001) Some recent developments in surfactant drag reduction. *Proc. 2nd Symp. on Smart Control of Turbulence*, 43-58, University of Tokyo, Tokyo.